

**UNIVERSIDADE FEDERAL DE SANTA CATARINA
PROGRAMA DE PÓS-GRADUAÇÃO EM ENGENHARIA
MECÂNICA**

André Ricardo Popinhak

**INVESTIGAÇÃO EXPERIMENTAL DA CONVECÇÃO
NATURAL TURBULENTA EM UMA CAVIDADE COM
PAREDES VERTICAIS A DIFERENTES TEMPERATURAS E
RAZÃO DE ASPECTO 4**

Dissertação submetida ao Programa de Pós Graduação em Engenharia Mecânica da Universidade Federal de Santa Catarina para a obtenção do Grau de Mestre em Engenharia Mecânica.

Orientador:

Prof. César J. Deschamps, Ph.D.

Florianópolis
2013

Ficha de identificação da obra elaborada pelo autor,
através do Programa de Geração Automática da Biblioteca Universitária da UFSC.

Popinhak, André Ricardo

Investigação experimental da convecção natural turbulenta em uma cavidade com paredes verticais a diferentes temperaturas e razão de aspecto 4 [dissertação] / André Ricardo Popinhak ; orientador, César José Deschamps - Florianópolis, SC, 2013.

137 p.

Dissertação (mestrado) - Universidade Federal de Santa Catarina, Centro Tecnológico. Programa de Pós-Graduação em Engenharia Mecânica.

Inclui referências

1. Engenharia Mecânica. 2. Convecção natural. 3. Turbulência. 4. Cavidade paralelepípeda. I. Deschamps, César José. II. Universidade Federal de Santa Catarina. Programa de Pós-Graduação em Engenharia Mecânica. III. Título.

André Ricardo Popinhak

**INVESTIGAÇÃO EXPERIMENTAL DA CONVECÇÃO
NATURAL TURBULENTA EM UMA CAVIDADE COM
PAREDES VERTICAIS A DIFERENTES TEMPERATURAS E
RAZÃO DE ASPECTO 4**

Esta Dissertação foi julgada adequada para a obtenção do Título de “Mestre”, e aprovada em sua forma final pelo Programa de Pós Graduação em Engenharia Mecânica.

Florianópolis, 21 de fevereiro de 2013.

Prof. Júlio César Passos, Dr.

Coordenador do Programa de Pós-Graduação em Engenharia Mecânica

Banca Examinadora:

Prof. César J. Deschamps, Ph.D.

Orientador

Prof.^a Juliana Rodrigues Loureiro, D.Sc. (UFRJ)

Prof. Juan Pablo de Lima Costa Salazar, Ph.D.

Prof. Saulo Güths, Dr.

Em homenagem a minha amada esposa Marie, que faleceu durante a realização deste trabalho. Seu amor incondicional, companheirismo e incentivos foram de fundamental importância para que eu defendesse essa dissertação e tivesse forças pra continuar essa jornada.

AGRADECIMENTOS

Ao Prof. César J. Deschamps pela confiança, paciência e orientação neste trabalho, além do exemplo de profissionalismo e caráter.

Aos técnicos: Fabiano Van Bommel, Eduardo Ludgero e Tiago Fernandes pelo auxílio durante as instrumentações de minha bancada experimental.

Ao projetista e amigo Ricardo Hellmann pelo empenho e dedicação no projeto de todo o aparato experimental.

Aos engenheiros Driek Rouwenhorst e Jan Christiaan Willemsen da Universidade de Twente na Holanda pela dedicação e comprometimento durante seus estágios realizados no laboratório, além dos bons momentos vividos dentro e fora da Universidade.

Aos demais colegas do Laboratório de Pesquisas em Refrigeração e Termofísica - POLO, pelo apoio e cooperação. Entre eles: Dalton Bertoldi, Daniel Hense, Marco Macarini e Pedro Magalhães.

Aos meus pais e avós pelo suporte durante toda minha formação acadêmica.

A Marie pelo amor, companheirismo e incentivo nos momentos difíceis.

A CAPES e a Embraco pelo indispensável apoio financeiro.

Mais cedo ou mais tarde, a teoria sempre
acaba assassinada pela experiência.

(Albert Einstein)

RESUMO

A convecção natural em cavidades fechadas tem sido extensivamente investigada em função de sua importância em diversas aplicações tecnológicas, tais como resfriamento de componentes eletrônicos, isolamento de reatores nucleares, conforto térmico em edificações e compartimentos de refrigeradores domésticos. O presente trabalho consiste na investigação experimental da convecção natural turbulenta em uma cavidade paralelepípeda. A cavidade em estudo possui uma razão de aspecto altura/largura igual a quatro e base quadrada, com as paredes verticais mantidas em diferentes temperaturas, resultando em um número de Rayleigh igual a $1,14 \times 10^{10}$. Medições de perfis de velocidade e tensões de Reynolds são realizadas via velocimetria laser Doppler (LDV) em diferentes seções da cavidade. O escoamento demonstrou ser restrito às regiões próximas das paredes verticais, com velocidades mais elevadas junto à parede quente. Um resultado inesperado foi obtido na região da parede fria, onde logo depois de uma fina camada de fluido que escoava para baixo, o escoamento se dá no sentido ascendente. Através de perfis da componente vertical de velocidade e da visualização via velocimetria por imagens de partículas (PIV), observou-se que isto é provavelmente causado por uma camada de fluido intrusiva que se move para cima. Campos instantâneos de velocidade obtidos pelas medições PIV também indicam a presença de vórtices que se movem ao longo de ambas as paredes verticais.

Palavras-chave: Convecção natural, cavidade paralelepípeda, turbulência.

ABSTRACT

Turbulent natural convection in cavities has been extensively studied due to its importance in various technological applications, such as cooling of electronic components, insulation of nuclear reactors, thermal comfort in buildings and compartments of refrigerators. This master's thesis reports an experimental investigation of turbulent natural convection in a parallelepiped cavity. The cavity has an aspect ratio height/width equal to four and a square base, with the vertical walls maintained at different temperatures, resulting in a Rayleigh number equal to 1.14×10^{10} . Measurements of velocity and Reynolds stresses were carried out via laser Doppler velocimetry (LDV) in different sections of the cavity. The flow was found to be restricted within a very narrow region next to vertical walls, with higher levels of velocity next to the hot wall. Unexpectedly, fluid flow was seen to be upwards after a very thin layer of descending flow along the cold wall. With reference to profiles of vertical velocity component and flow images acquired through PIV, it was observed that this phenomenon is probably associated with a fluid intrusion traveling upwards. PIV measurements also indicate the presence of vortices moving along both vertical walls.

Keywords: Natural convection, parallelepiped cavity, turbulence.

FIGURES

Figure 1.1- Geometry of a cavity with internal heat generation. (Oztop and Bilgen, 2006)	29
Figure 1.2- Contours for velocity components: (a) Horizontal; (b) Vertical, $Ra_H = 10^6$, $Pr = 0.71$, $h/H = 0.25$. (Alamiri <i>et al.</i> , 2009)	30
Figure 1.3- Formation of Bénard cells. (Pavel Urban, 2012).....	30
Figure 1.4- Streamlines (top), isotherms (bottom), $Ra_H = 3 \times 10^4$, $Pr = 0.7$. (Treck, 2012)	31
Figure 1.5- Schematic of a differentially heated rectangular cavity with the dimensions $D \times W \times H$ (depth \times width \times height).	31
Figure 2.1- Schematic diagram of Ampofo's (2004) test cavity.	36
Figure 2.2- Averaged profiles at cavity mid-height, $Y = 0.5$ and $Z = 0.5$, of horizontal velocity (u_2), vertical velocity (u_3), and temperature (T). Source: Soria <i>et al.</i> , (2004).	40
Figure 3.1- Schematic diagram of the LDV experimental apparatus.	43
Figure 3.2- 1) Cavity; 2) Support; 3) Vibration Isolator; 4) LDV probe; 5) Displacement Device; 6) Thermal baths; 7) Radiation Shield; 8) Room thermocouples.....	44
Figure 3.3- Formation of interference fringes.....	45
Figure 3.4- Flow measurement technique using an optically fixed measurement volume. (Cunha and Silva, 2000)	46
Figure 3.5- Beam separator with three output pairs of beams: green, blue and violet. (TSI, 2008).....	48
Figure 3.6- Schematic of a typical PIV measurement system (Blonski <i>et al.</i> , 2008).....	50
Figure 3.7- Schematic diagram of the PIV experimental apparatus.....	51
Figure 3.8- Dynamic response of spherical Polyamide seeding particles with different nominal diameters.	53
Figure 3.9- Light scattering of a hollow glass sphere in air for three different diameters according to Mie's theory ($\lambda = 0.488 \mu\text{m}$). The polar scale is logarithmic (Tarozzi, 2007).	55
Figure 3.10- Rayleigh number \times Characteristic length (H), $T_H = 28 \text{ }^\circ\text{C}$, $T_C = 18 \text{ }^\circ\text{C}$, $\Delta T = 10 \text{ }^\circ\text{C}$, $P = 1 \text{ atm}$	57
Figure 3.11- Rayleigh number \times Pressure, $T_H = 28 \text{ }^\circ\text{C}$, $T_C = 18 \text{ }^\circ\text{C}$, $\Delta T = 10 \text{ }^\circ\text{C}$, $H = 400 \text{ mm}$	57
Figure 3.12- Cavity used in this work.....	58
Figure 3.13- Closed circuit flow between bath and isothermal wall.	60
Figure 3.14- Illustration of the serpentine-like channels of the cavity to allow the hot and cold water to maintain, as far as possible, isothermal conditions of the walls.....	60
Figure 3.15- Detailed view of the thermocouple's channels.	61
Figure 3.16- 1) Cavity; 2) Support; 3) Vibration Isolator.	63
Figure 4.1- Incident laser beams from a probe tilted for measurement in the near-wall region.	67

Figure 4.2- Refraction of two laser beams in two mediums.	68
Figure 4.3- Refraction through the interfaces air-acrylic-water.....	69
Figure 4.4- Behavior of the beam crossing the cavity wall.....	70
Figure 4.5- Schematic diagram of the thermocouple calibration apparatus.....	72
Figure 4.6- Experimental thermocouple calibration apparatus.....	72
Figure 4.7- Thermocouple calibration curve.	73
Figure 4.8- Results of the calibration procedures for all the thermocouples.	74
Figure 5.1- Mean velocity distribution at different heights: (a) vertical velocity; (b) horizontal velocity.	81
Figure 5.2- Mean velocity distribution at $Y = 0.1$: (a) vertical velocity; (b) horizontal velocity.	82
Figure 5.3- Mean velocity distribution at $Y = 0.2$: (a) vertical velocity; (b) horizontal velocity.	83
Figure 5.4- Mean velocity distribution at $Y = 0.3$: (a) vertical velocity; (b) horizontal velocity.	84
Figure 5.5- Mean velocity distribution at $Y = 0.4$: (a) vertical velocity; (b) horizontal velocity.	85
Figure 5.6- Mean velocity distribution at $Y = 0.5$: (a) vertical velocity; (b) horizontal velocity.	86
Figure 5.7- Mean velocity distribution at $Y = 0.6$: (a) vertical velocity; (b) horizontal velocity.	87
Figure 5.8- Mean velocity distribution at $Y = 0.7$: (a) vertical velocity; (b) horizontal velocity.	88
Figure 5.9- Mean velocity distribution at $Y = 0.8$: (a) vertical velocity; (b) horizontal velocity.	89
Figure 5.10- Mean velocity distribution at $Y = 0.9$: (a) vertical velocity; (b) horizontal velocity.	90
Figure 5.11- Velocity vectors: (a) entire cavity; (b) mid-height region on the cold wall side.....	91
Figure 5.12- Validation of the employed experimental techniques (PIV and LDV). Vertical velocity component in the cold wall side at $Z = 0.5$: (a) $Y = 0.1$; (b) $Y = 0.2$	93
Figure 5.13- (a) Mean velocity and (b) Instantaneous fields for PIV on the cold wall side. x is the distance from the cold wall; y is the distance from the bottom.	94
Figure 5.14- (a) Mean velocity and (b) Instantaneous fields for PIV on the hot wall side. x is the distance from the hot wall; y is the distance from the bottom.	95
Figure 5.15- Instantaneous velocity field for different time frames on the cold wall side: (a) $t = 0$ s, (b) $t = 1.4$ s, (c) $t = 2.8$ s.....	96
Figure 5.16- Instantaneous velocity field for different time frames on the hot wall side: (a) $t = 0$ s, (b) $t = 1$ s, (c) $t = 2$ s.....	97
Figure 5.17- Comparison of the vertical velocity at cavity mid-height $Y = 0.5$ and $Z = 0.5$ and 0.95	98

Figure 5.18- Velocity signals near the cavity walls at $Y = 0.5$: (a) hot wall; (b) cold wall.	99
Figure 5.19- Vertical velocity fluctuation at different heights.	100
Figure 5.20- Horizontal velocity fluctuation at different heights.	101
Figure 5.21- Relation between fluctuation quantities near the walls at $Y = 0.5$; (a) hot wall side; (b) cold wall side.	102
Figure 5.22- Distribution of Reynolds-stress at different heights.	104
Figure 5.23- Turbulent kinetic energy along the walls: (a) hot wall; (b) cold wall.	106
Figure 5.24- Contours of turbulent kinetic energy.	107
Figure 5.25- Comparison between the arithmetic mean and the sample and hold processor (S/H) in the reconstruction of the vertical velocity signal at $Y = 0.5$ on the cold wall side.	111
Figure B.0.1- Cause and effect diagram for a velocity component.	129
Figure B.0.2- Schematic diagram showing the experimental arrangement for direct measurement of the intersection angle of the laser beams (Bean and Hall, 1999).	130

LIST OF TABLES

Table 3.1- Specifications of the Fiber optic Probe model TLN06-363. (TSI, 2007).....	48
Table 3.2- Specifications of thermoelectric bath. (Quimis, 2010).....	58
Table 3.3- Corresponding thermocouple to the place of measurement.....	62
Table 3.4- Specifications of Traverse System. (TSI, 2006).....	63
Table 4.1- Polynomial coefficients for a linear curve fitting.	73
Table 4.2- Combined standard uncertainty for temperature.	74
Table 4.3- Standard uncertainties of the experimental quantities.	76
Table A.0.1- Level of confidence x coverage factor.....	125

LIST OF ABBREVIATIONS

<i>CFD</i>	Computational Fluid Dynamics
<i>CW</i>	Continuous Wave
<i>DNS</i>	Direct Numerical Simulation
<i>KEM</i>	k- ϵ model
<i>LDV</i>	Laser Doppler velocimetry
<i>LES</i>	Large Eddy Simulation
<i>SMC</i>	Second moment closure

LIST OF SYMBOLS

$a-$	lower limit of a rectangular probability distribution
$a+$	upper limit of a rectangular probability distribution
a_0, a_1, a_3	polynomial coefficients
AR_h	horizontal aspect ratio, $AR_h = D/W$
AR_v	vertical aspect ratio, $AR_v = H/W$
B_p	buoyancy force acting on the seeding particle
F_D	drag force
c	distance of the internal heat source from the cavity wall
c_{fD}	sensitivity coefficient of the Doppler frequency
c_i	sensitivity coefficients
c_θ	sensitivity coefficient of angle between the crossing laser beams
c_λ	sensitivity coefficient of the wavelength
C_μ	turbulent-viscosity constant in the k- ϵ model
d_p	diameter of the seeding particle
f_D	Doppler frequency
D	depth
g	gravitational acceleration
g_i	estimator of the weight factor
g_{ui}, g_{vi}	estimator of the weight factor of the u and v velocity components
h	height of the internal heat source
H	height
I	turbulent intensity, $I \equiv \sqrt{2k/3}/V_0$
k	turbulence kinetic energy per unity mass
k_p	coverage factor
l	turbulent length scale
L	distance between the heated walls of the cavity
m_i	i -th measured velocity
\bar{m}	mean velocity components (\bar{u}, \bar{v})
m_p	mass of the seeding particle

m'_{rms}	root-mean-square of the fluctuation quantities (u'_{rms}, v'_{rms})
n	number of independent observations obtained under the same conditions of measurement
N	Number of measured particles, number of points employed in the curve fitting
n_1	refractive index of medium 1
n_2	refractive index of medium 2
n_a	refractive index of air
n_f	refractive index of water
n_f	refractive index of fluid
n_p	refractive index of particle
n_w	refractive index of acrylic
p	level of confidence
P	pressure
PD	polynomial degree
Pr	Prandtl number, $Pr = \nu/\alpha$
R	correlation coefficient
$r(x_i, x_j)$	correlation coefficient of the uncertainties
Ra_H	Rayleigh number based on cavity height, $Ra_H = \frac{g\beta\Delta TH^3}{\nu\alpha}$
Re_p	Reynolds number based on the seeding particle diameter
$s(x_i)$	standard deviation of a sample
t	time measured from the light scattered by the particle, thickness of the window
T	temperature, time scale of the largest eddy
$TC1, TC2, TC3...$	thermocouple channels
t_i	arrival time of the i-th particle in the measurement volume
T_h	hot wall temperature
T_c	cold wall temperature
T_o	working temperature
T_{ref}	reference temperature, measured through the bulb thermometer
$U(T)$	expanded uncertainty

$u(xi)$	standard uncertainty
u, v, w	velocity components in x, y, z directions
u', v', w'	fluctuation velocity components in x,y,z directions respectively
u_b	standard uncertainty of the thermal expansion coefficient
$u_c(T)$	combined standard uncertainty
u_{DT}	standard uncertainty of the temperature difference
u_g	standard uncertainty of the gravitational acceleration
u_H	standard uncertainty of the height
u_m, v_m, w_m	actual Measured velocity components according to the tilt angle of the probe
u_{T_h}, u_{T_c}	standard uncertainty of the hot and cold wall temperature measurements, respectively
u'_{rms}, v'_{rms}	root-mean-square of the fluctuation velocities
u_{Ra}	Rayleigh number combined uncertainty
u_α	standard uncertainty of the thermal expansion coefficient
u_ν	standard uncertainty of the kinematic viscosity
$\overline{u'v'}$	Reynolds stress
U_p	particle velocity
U_{max}	maximum measured velocity
V	tension in voltage obtained from the thermocouples
V_k	k -th value of the measured temperature
$V_{LS,k}$	value obtained by the polynomial curve fitting from calibration
$V_{measured}$	measured velocity by the LDV system
V_o	the buoyancy velocity, $V_o = \sqrt{g\beta W(T_h - T_c)}$
w	width of the internal heat source
W	width
W_p	weight of the seeding particle
x, y, z	Cartesian coordinates
X, Y, Z	dimensionless coordinates, ($X=x/W, Y=y/H, Z=z/D$)
\bar{x}_i	sample mean of n independent observations
X_i	list of the uncertainty sources
y	average of a measurement Y

Y	represents the measurand
y_a	undisturbed position of the measured volume
y_f	disturbed position of the measured volume

GREEK LETTERS

α	thermal diffusivity
β	coefficient of thermal expansion, refractive angle
γ	ratio between the densities of the particle and the fluid respectively (ρ_p/ρ_f)
δ_f	fringe spacing
δH	assembly tolerance
ΔT	temperature difference
ε	dissipation rate of turbulent kinetic energy
η	Kolmogorov length scale
θ	angle between incidence laser beams, incidence angle of a laser beam passing from one medium to another one
θ_{tilt}	tilt angle of the probe
λ	wavelength
μ	dynamic viscosity
μ_f	dynamic viscosity of the fluid
ν	kinematic viscosity
ν_{eff}	effective degrees of freedom
ρ	density
ρ_p	density of the seeding particle
τ	Kolmogorov time scale
τ_p	characteristic time of the seeding particle
v	Kolmogorov velocity scale

SUMMARY

1. INTRODUCTION	27
1.1 NATURAL CONVECTION FLOWS	27
1.2 NATURAL CONVECTION IN ENCLOSED CAVITIES.....	27
1.2.1 CAVITIES WITH INTERNAL HEAT GENERATION.....	29
1.2.2 CAVITIES HEATED ON THE BOTTOM.....	30
1.2.3 CAVITIES WITH VERTICAL WALLS MAINTAINED AT DIFFERENT TEMPERATURES.....	31
1.3 MAIN OBJECTIVES.....	32
1.4 THESIS STRUCTURE.....	32
2. LITERATURE REVIEW.....	33
2.1 EXPERIMENTAL INVESTIGATIONS	34
2.2 NUMERICAL ANALYSES	37
2.3 CONCLUDING REMARKS.....	42
3. EXPERIMENTAL SETUP	43
3.1 OVERVIEW OF THE EXPERIMENTAL APPARATUS.....	43
3.2 LASER DOPPLER VELOCIMETRY	44
3.2.1 LASER SOURCE	47
3.2.2 OPTICAL SYSTEM.....	47
3.2.3 ACQUISITION AND SIGNAL PROCESSING SYSTEMS.....	49
3.3 PARTICLE IMAGE VELOCIMETRY	49
3.4 SEEDING PARTICLES	51
3.5 CAVITY	55
3.5.1 TEMPERATURE CONTROL SYSTEM	58
3.5.2 TEMPERATURE MEASUREMENT.....	61
3.6 AUXILIARY COMPONENTS	62
3.6.1 VIBRATION ISOLATOR AND SUPPORT	62
3.6.2 DISPLACEMENT DEVICE	63
3.6.3 RADIATION SHIELD	63
4. EXPERIMENTAL PROCEDURE.....	65
4.1 MEASUREMENT PROCEDURE.....	65
4.1.1 MEASURING WITH A TILTED PROBE	66

4.1.2	MEASURING CONFINED FLUIDS.....	67
4.2	<i>UNCERTAINTY ANALYSIS</i>	70
4.2.1	TEMPERATURE	71
4.2.2	EXPANDED UNCERTAINTY	75
4.2.3	EXPERIMENTAL REPEATABILITY	77
5.	RESULTS.....	79
5.1	<i>VELOCITY DISTRIBUTION</i>	79
5.2	<i>INFLUENCE OF THE WALLS</i>	98
5.3	<i>TURBULENCE ANALYSIS</i>	98
5.4	<i>DISCUSSION OF RESULTS</i>	108
5.4.1	ASYMMETRY OF THE FLOW	109
5.4.2	UPWARD VELOCITY NEAR THE COLD WALL	109
6.	CONCLUSIONS.....	113
6.1	<i>PRELIMINARY CONSIDERATIONS</i>	113
6.2	<i>MAIN FINDINGS</i>	113
6.3	<i>SUGGESTIONS FOR FUTURE WORK</i>	114
	REFERENCES.....	115
	APPENDIX A - UNCERTANTY EVALUATION.....	123
A.1	<i>TYPE A EVALUATION OF UNCERTAINTY</i>	124
A.2	<i>TYPE B EVALUATION OF UNCERTAINTY</i>	124
A.2.1	RECTANGULAR PROBABILITY DISTRIBUTION.....	125
A.2.2	NORMAL PROBABILITY DISTRIBUTION	125
A.2.3	POLYNOMIAL UNCERTAINTY	127
	APPENDIX B - ANALYSIS OF VELOCITY UNCERTAINTY	129
	ATTACHMENT A- PART 1: CALIBRATION REPORT OF THE BULB	
	THERMOMETER	131
	ATTACHMENT A- PART 2: CALIBRATION REPORT OF THE BULB	
	THERMOMETER	133
	ATTACHMENT B - REPEATABILITY OF EXPERIMENT	135

1. INTRODUCTION

Although some engineering problems are easily represented by simplified mathematical models, many flows encountered in everyday life are usually complex. Complex flows can be momentum-driven by an applied force (e.g., by a fan or a pump), or can occur naturally; based on the physical and thermodynamic properties of matter. Natural flow situations arise when a body force field such as gravity acts on a fluid. For example, if a density gradient exists within a fluid, a buoyancy force induces natural fluid motion. In general, a density gradient is due to a temperature gradient.

1.1 NATURAL CONVECTION FLOWS

Most flows that take place in our surroundings are induced by buoyancy. Natural convection flows, also known as buoyancy-driven flows, can be seen as air circulation around our bodies, in the atmosphere, oceanic circulation, etc.

Kakaç *et al.* (1985) observed that natural convection has remained one of the less well-understood heat transfer processes. The authors listed a number of complexities that are responsible for this, including: transition to turbulence, turbulence buoyant generation, unbounded domains as in plumes, stratified fluids caused by combined temperature and concentration variations, and variable fluid property effects.

Natural convection flows can be subdivided into two major categories: (i) buoyant flows imposed by temperature differences or heat transfer over a surface, known as external natural convection flows; (ii) buoyant flows that occur inside cavities bounded by surfaces, which are called internal natural convection flows. The next section will be limited to discussing the latter, which is the main objective of the present work.

1.2 NATURAL CONVECTION IN ENCLOSED CAVITIES

The phenomenon of natural convection inside a closed cavity exhibits complex interactions between fluid elements that are in thermal contact with the cavity walls. Such interactions create a coupling between the temperature and velocity fields, and generate difficulties in both the numerical and experimental analyses. Additionally, this phenomenon is influenced by the geometry and orientation of the cavity itself.

Due to its inherent complexity, enclosed natural convection has not been studied as extensively as other natural flows, such as non-enclosed natural convection. In earlier works, researchers focused primarily on laminar and low-level turbulence flows. These more simplified situations have been fully characterized and researchers have been able to model the flow. Currently, the community is devoted to more complex, turbulent flows. Despite improvements in experimental measurement techniques and advances in numerical models and computing capability, these problems are still very challenging and there is still no reliable tool for correctly predicting turbulent phenomena. These difficulties have been documented by Tian and Karayiannis (2000) as well as Dol and Hanjalic (2000).

Natural convection in enclosed cavities is encountered in many practical applications, such as electronic cooling systems, solar collectors, nuclear reactor containment and radioactive waste containers. These real-world applications can be divided into three major types: (1) cavities in which the flow is due to internal heat generation, (2) cavities heated at the bottom (Rayleigh-Bénard configuration), and (3) cavities with vertical walls maintained at different temperatures. The focus of this work is type 3, but it is worth considering some basic information about all three types of flow. However, prior to that, it is convenient to present the dimensionless parameters necessary to characterize the flows in enclosed cavities.

The fluid motion within the cavity is buoyancy driven, and is a function of the cavity geometry, fluid properties, and temperature difference within the fluid ($\Delta T = T_h - T_c$). The flow can be completely characterized by three dimensionless parameters: the geometric aspect ratio (vertical $AR_v = \text{height}/\text{width}$, and horizontal $AR_h = \text{depth}/\text{width}$); the Prandtl number (Pr); and the Rayleigh number (Ra_H), which characterizes the flow regime, representing the ratio between the buoyancy and viscous forces:

$$Ra_H = \frac{g\beta\Delta TH^3}{\nu\alpha} \quad (1.1)$$

In Equation (1.1), g is the intensity of the gravitational field [m/s^2], β is the thermal expansion coefficient of the confined fluid [$1/\text{K}$], ΔT is the temperature difference between the isothermal walls [K], H is the geometric characteristic length [m], taken as the cavity

height, and ν and α are the kinematic viscosity [m^2/s] and the thermal diffusivity [m^2/s] of the fluid, respectively.

As mentioned before, turbulence is one of the main sources of complexity in natural convection problems. For natural convection in cavities the turbulent regime occurs at high Rayleigh numbers, and as reported by Kuyper *et al.* (1993), the laminar regime prevails for values of $Ra_H \leq 10^8$ for differentially heated cavities, i.e., flow type 3.

1.2.1 Cavities with Internal Heat Generation

In recent years, the study of natural convection in cavities with volumetric heat generation has become a subject of intense interest mainly due to nuclear safety issues (Horvat *et al.*, 2001; Liu *et al.*, 2006; Lee *et al.*, 2007).

If a nuclear reactor is operating, and if the cooling process is interrupted, a core-melt can result within a very short time. In the case of the destruction of a reactor building due to an inadequate or failed cooling system, a core-melt accident of the most hazardous category results; rapid melting with open containment, and the radioactive releases will be particularly high, as pointed out by Frogatt (2005). Figure 1.1 shows a typical geometry of a cavity with internal heat generation, and Figure 1.2 shows magnitude contours for horizontal and vertical velocity components, respectively, of the associated flow field.

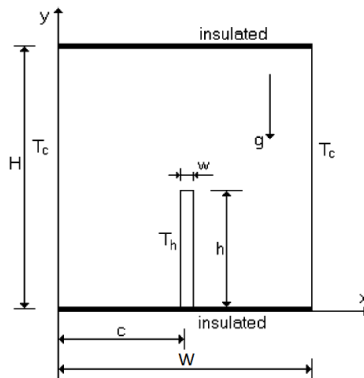


Figure 1.1- Geometry of a cavity with internal heat generation. (Oztop and Bilgen, 2006)

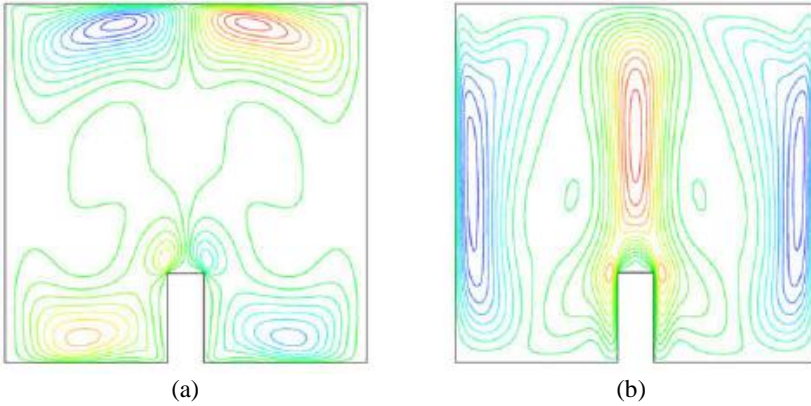


Figure 1.2- Contours for velocity components: (a) Horizontal; (b) Vertical, $Ra_H = 10^6$, $Pr = 0.71$, $h/H = 0.25$. (Alamiri *et al.*, 2009)

1.2.2 Cavities Heated on the Bottom

In situations where the cavities are heated from the bottom, the imposed temperature difference must exceed a critical value before the fluid starts moving and convective heat transfer takes place. These flows are known as Rayleigh-Bénard convection. Immediately above $Ra_H = 1708$ (Bejan, 2004), the flow consists of rotating two-dimensional rolls, also known as Bénard cells (see Figure 1.3). Figure 1.4 shows the corresponding streamlines and isotherms.

Rayleigh-Bénard convection is a peculiar type of natural convection generated by density stratification in the direction of gravity. Due to its importance in several engineering applications, this phenomenon has been extensively investigated with particular attention dedicated to rectangular and square geometries. Most works consider free convection and analyze the heat transfer dependency in relation to a number of parameters, such as: the Rayleigh number, the Prandtl number, the boundary conditions, and aspect ratio of the cavity.

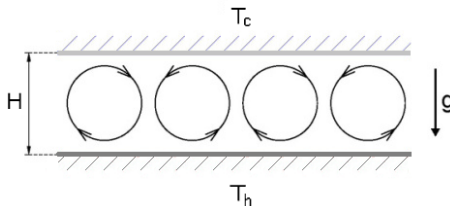


Figure 1.3- Formation of Bénard cells. (Pavel Urban, 2012)

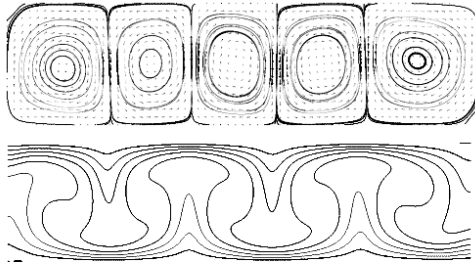


Figure 1.4- Streamlines (top), isotherms (bottom), $Ra_H = 3 \times 10^4$, $Pr = 0.7$. (Treack, 2012)

1.2.3 Cavities with Vertical Walls Maintained at Different Temperatures

This problem is the focus of this work. It corresponds to a cavity with two opposing vertical walls maintained at different temperatures and the remaining walls assumed to be adiabatic (see Figure 1.5). This is a typical heat transfer problem for many important applications, such as: industrial cooling systems, crystal growth procedures, building insulation, and buoyancy-induced horizontal mass transfer in geophysical flows (Schöpf and Patterson, 1996).

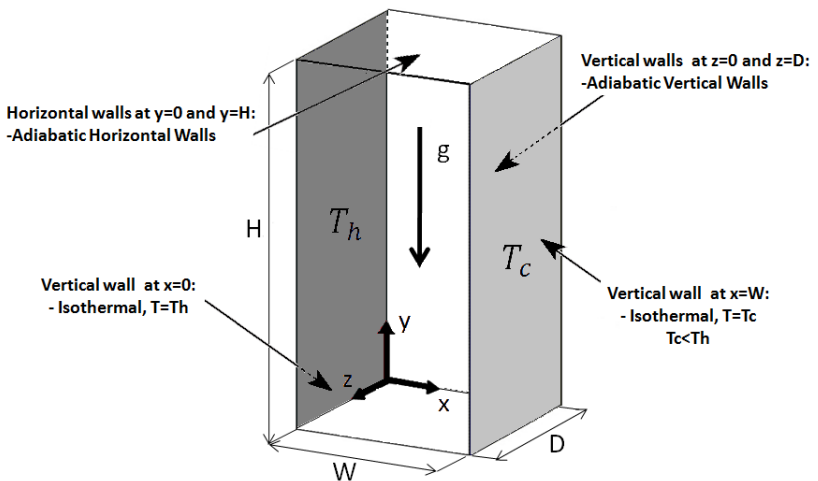


Figure 1.5- Schematic of a differentially heated rectangular cavity with the dimensions $D \times W \times H$ (depth \times width \times height).

1.3 MAIN OBJECTIVES

The goal of this work is to investigate experimentally the turbulent natural convection inside an enclosed cavity with vertical aspect ratio $AR_v = 4$. Within the cavity, one of the walls is heated and maintained at a temperature T_h and the other cooled at a temperature T_c . All the remaining walls are considered to be adiabatic. It is also sought a high level of turbulence, with a Rayleigh number based on the cavity height of the order of $Ra_H \sim 10^{10}$.

In order to achieve the aforementioned objectives, the following activities were carried out:

- Design of a rectangular cavity with a stability apparatus to guarantee highly accurate experimental measurements;
- Measurement of velocity profiles within the cavity at different heights and depths by using the Laser Doppler Velocimetry (LDV);
- Determination of the associated measurement uncertainty;
- Analysis of the three-dimensional effects of the presence of the adiabatic walls on the flow;
- Analysis of the turbulence flow field within the cavity.

1.4 THESIS STRUCTURE

In this chapter, the main motivations and objectives for the present work were established. Chapter 2 presents important considerations related to this work through a literature review. The experimental apparatus and the procedure are described in Chapters 3 and 4, respectively. The experimental results are presented in Chapter 5. Finally, Chapter 6 discusses the main findings and possible directions for further work.

2 LITERATURE REVIEW

It is found that thermally driven flows in three-dimensional enclosures is a very active area of research. The number of physical aspects that have been considered in the literature is very large and alternatives for future investigations are almost unlimited. Even for classical flow configurations, such as differentially heated and Rayleigh-Bénard cavities, there have been some recent important contributions related to both numerical simulation and experimental analysis.

For situations where two opposite vertical walls of the cavity are maintained at different temperatures, the majority of the related literature uses two-dimensional flow geometries. Moreover, the range of Rayleigh numbers studied is generally low, such that the fluid flow is restricted to laminar or low-level turbulence regimes (Vahl Davis and Jones, 1983; Hortmann *et al.*, 1990; Le Quéré, 1991).

On the other hand, cubic geometries have been employed more recently (Fusegi *et al.*, 1990; Dabiri *et al.*, 1996; Ker and Lin., 1996; Tric *et al.*, 2000; Frederick and Quiroz, 2001; Peng *et al.*, 2003). Stationary multicellular flow has been studied for tall cavities (Le Quéré, 1990; Schweiger *et al.*, 1995; Lartigue *et al.*, 2000).

In most cases the working fluid is air, but other fluids have been employed, such as: glycerol (Lutjen *et al.*, 2001), water (Schöpf and Patterson, 1996), and silicon oil (Hsieh and Yang, 1996), and a low-Prandtl fluid ($Pr = 0.015$, Jing *et al.*, 2003). Different fluids are used primarily to maintain high values of the Rayleigh number, sufficiently small geometric cavity dimensions, and a practical temperature difference between the heated walls.

Other experimental works on natural convection within cavities focus on altering the geometric orientation of the cavity. Specific examples of different geometric orientations include the work by Leong *et al.* (1998) on the inclination of cavities and the effect of rotation (Ker and Lin, 1996; 1997).

In addition, a significant number of natural convection studies have investigated the effect of turbulence in the fluid flow and heat transfer, i.e., with high Rayleigh numbers ($Ra_H > 10^9$).

The aforementioned works give the reader an idea of the large number of studies, although almost all of them for low Rayleigh flows ($Ra_H < 10^8$). Considering the main objective of this work, the literature review presented in the coming sections will be limited to three-dimensional differentially heated cavities at $Ra_H > 10^8$. The only

exception is the work of Kizildag *et al.* (2010), which is two-dimensional.

2.1 EXPERIMENTAL INVESTIGATIONS

Hsieh and Yang (1996) built a cavity with the relative dimensions of height: width: depth of 3:1:1.2, using silicon oil ($Pr = 457$) as the working fluid. They analyzed the transient temperature distribution and flow pattern history, and also the hot wall Nusselt number. They concluded that there is a three-dimensional effect in the enclosure at $Ra_H = 4.12 \times 10^8$ and that the working medium, such as silicone oil, does affect the transient flow behavior, due to its viscosity variation across the enclosure.

Schöpf and Patterson (1996), using the shadowgraph technique, studied flow development until a steady state was reached in a water-filled square cavity that was suddenly heated and cooled on opposing sidewalls. The employed cavity had height, width, and depth dimensions of 0.24, 0.24, and 0.5 m, respectively, at $Ra_H = 4.9 \times 10^8$ and 7.2×10^8 . The authors obtained results of a time series of shadowgraph images that showed: a second group of waves traveling up the hot boundary layer; the impact of the second wave group on the top intrusion; the further evolution of the intrusion flow after the second wave group had gone by; the approach to the final steady state, and the final steady state; the locations of individual wave peaks up the hot boundary layer as functions of time for the steady-state waves; and velocities of individual wave peaks as functions of the distance up the hot boundary layer. The authors concluded that central to the flow development at this stage is the formation and the subsequent collapse of a region of several flow reversals near the upstream end of the horizontal intrusion flow. The flow-reversal structure has a sudden and relatively strong response to the waves arising from the vertical boundary layer. However, it appears that the contraction and upstream motion of the structure is not related to the presence of the waves.

The measurement techniques of the velocity field are usually non-intrusive Particle Image Velocimetry (PIV), or Laser Doppler Velocimetry (LDV). However, a significant number of studies have measured the temperature field with intrusive sensors, such as micro-thermocouples (Salat *et al.*, 2004; Ampofo, 2004; 2005; Saury *et al.*, 2011).

Mergui and Penot (1997) studied an air-filled cavity with height, width, and depth dimensions of 0.94, 1.04, and 0.7 m, respectively, at

$Ra_H = 1.69 \times 10^9$. They employed LDV and thermocouples to measure the velocity and temperature, respectively. Results were presented for temperature and velocity profiles, mean root square of temperature and velocity fluctuations, the magnitude and location of maximum velocity, shear stress and friction coefficients, and turbulent kinetic energy and turbulence production terms. Examination of the local temperatures in the core region and the two boundary layers located along the vertical walls highlights the conservation of the symmetry imposed by the boundary conditions. The phenomenon of relaminarization in regions of the boundary layer upstream, and the appearance of low thermal turbulence in regions further downstream, are also highlighted.

Tian and Karayiannis (2000) performed a study in an air-filled cavity with height, width, and depth dimensions of 0.75, 0.75, 1.5 m, respectively, resulting in a two-dimensional flow. They obtained the temperature and velocity, and their respective fluctuations in different regions of the cavity, and also the wall shear stress along the isothermal walls at $Ra_H = 1.58 \times 10^9$. They concluded that a low level of turbulence exists in the cavity at this Rayleigh number, that the flow is limited to a narrow strip along the walls where the velocity and temperature change sharply, and that the fluid in the cavity core is stationary and stratified.

Ampofo (2004) investigated turbulent natural convection in both a partitioned and non-partitioned cubic cavity ($Ra_H = 1.58 \times 10^9$) using air as the working fluid and obtained data for the fluctuating quantities of velocity, temperature, heat transfer and shear stress on the walls. One important aspect identified was the difficulty in obtaining experimentally adiabatic walls, even when the average cavity temperature $((T_h + T_c)/2)$ is maintained at the same temperature as the ambient temperature. In order to reduce the heat transfer on the vertical passive walls, the author built two guard cavities mounted on either side of the working temperature, so as to reduce the temperature gradient. Ampofo (2005) obtained the Reynolds stress and turbulent kinetic energy distribution at different heights for the cavity of his previous work. Figure 2.1 shows the test cavity of this author.

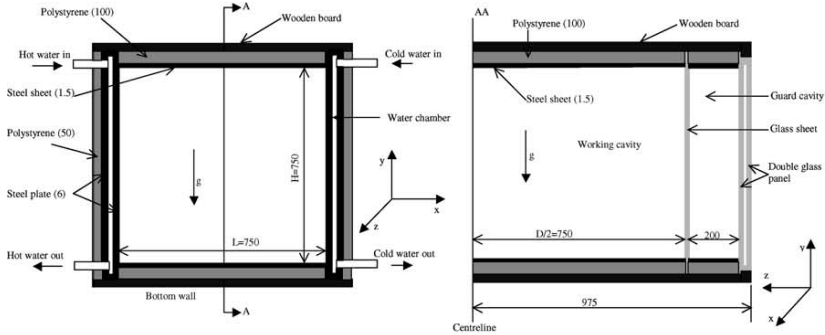


Figure 2.1- Schematic diagram of Ampofo's (2004) test cavity.

Salat *et al.* (2004) performed a numerical and experimental study in an air-filled cavity with height, width, and depth dimensions in 1, 1 and, 1 m, respectively, at $Ra_H = 1.5 \times 10^9$, in order to understand the discrepancy observed on the vertical thermal stratification in the core region of the cavity between the numerical and experimental data. The authors employed micro-thermocouples to measure the temperature distribution and LDV to measure the velocity. They concluded that using experimentally measured temperature distributions along the top and bottom walls as boundary conditions in the numerical simulations, the agreement between the experimental and numerical studies is improved.

Saury *et al.* (2011) performed an experimental study using air as the working fluid within a cavity with height, width, and depth dimensions of 3.84, 1, and 0.86 m, respectively. The influence of wall radiation on the stratification parameter was highlighted. The insulated walls were made of 8-cm-thick polyurethane foam panels and 3-cm-thick panels were added around the cavity on the outer side. On the inner side of the cavity, a low-emissivity film was added in order to reduce wall radiation. Measurement of velocity profiles through the LDV technique was performed in the upper region of cavity for three Rayleigh numbers (4.0×10^{10} , 8.1×10^{10} and 1.2×10^{11}). Temperature measurements were also carried out in the cavity by using micro-thermocouples. Airflow inside the cavity was analyzed and the Nusselt number along the hot and the cold wall was also presented. The authors concluded that the Rayleigh number has a small influence on the stratification parameter; whereas the aspect ratio (vertical AR_v and horizontal AR_h) and the wall emissivity both play an important role.

2.2 NUMERICAL ANALYSES

With the rapid advance in computer capacity and speed, the Computational Fluid Dynamics (CFD) technique has become a powerful alternative for predicting flows in enclosed spaces. It offers a high level of detail, higher degree of flexibility, and lower cost than experimental studies.

There are three different approaches to numerically solving turbulent flows via CFD: (i) Direct Numerical Simulation (DNS), (ii) Large Eddy Simulation (LES), and (iii) Simulation with turbulence models based on the Reynolds-Averaged Navier-Stokes equations (RANS).

DNS computes a turbulent flow by directly solving the Navier-Stokes equation without approximations. Therefore, the whole range of spatial and temporal scales of the turbulence is resolved, from the smallest dissipative scales (Kolmogorov scales) to the integral length scale, L . As a result, DNS requires a very fine grid resolution to capture the smallest eddies in the turbulent flow. In addition, this technique requires very small time steps, which makes the simulation time extremely lengthy.

In LES, the larger eddies, which are three-dimensional and unsteady, are directly solved as in the DNS formulation, whereas the effects of the smaller-scale motions are modeled. In terms of computational cost, LES lies between RANS models and DNS. Because the large-scale unsteady motions are directly computed, LES can be expected to be more accurate and reliable than the RANS models.

The RANS models evaluate the average quantities through modeling the effects of all scales of motion in the flow. This approach has become very popular in modeling flows in enclosed spaces due to its significantly small requirements on computer resources and user skills.

For many years, three-dimensional direct numeric simulations were restricted due to the absence of adequate computational resources. Recently, with increased computer processing power and parallelizations, simulations employing LES and even DNS have been carried out.

Janssen and Henkes (1996) analyzed through DNS the transitional instabilities of the flow inside a three-dimensional rectangular cavity with relative height, width, and depth dimensions of 1, 0.5, 2, respectively. $Pr = 0.71$ and 2, with Ra_H from 10^6 up to 4×10^8 . For an air-filled cubical cavity, it was found that there was a central region in the cavity near $z = D/2$, away from the lateral walls, where the

flow was mainly two-dimensional until the transition began. For larger Prandtl numbers ($Pr = 2$), there is no steady instability and the frequency of the resulting oscillation is very close to the two-dimensional value. The results also show that the instability is characterized by a wave-like modulation in the z -direction.

Dol and Hanjalic (2001) performed a computational study in a side-heated near-cubic cavity with relative height, width, and depth dimensions of 1, 1, and 1.5, respectively. They analyzed the flow pattern in the corner regions of the cavity at $Ra_H = 4.9 \times 10^9$, adopting air as the working fluid. Two kinds of lateral vertical walls were employed, corresponding to different experimental approximations of adiabatic conditions: the first by insulation, and the second by imposing a stratified wall heating. The authors used two RANS models represented by a second moment closure (SMC) and a k - ϵ model (KEM). The numerical computations showed that the SMC is more accurate at capturing thermal three-dimensionality effects and strong streamline curvature in the corners. However, the KEM provides reasonable predictions of the first-order turbulence moments away from corners.

Peng and Davidson (2001), through LES, analyzed an air-filled cavity with relative height, width, and depth dimensions of 1, 1, and 2, respectively, at $Ra_H = 1.58 \times 10^9$. The governing equations were discretized on a collocated grid using the second-order central differencing scheme. The solution was advanced in time using the second-order Crank-Nicolson scheme. The following results were obtained: velocity and temperature profiles, local Nusselt number and wall friction coefficient, streamlines and isotherms, second-order statistics for velocity and temperature, and contours of fluctuating velocity and vorticity. They concluded that the flow is characterized by a relatively low turbulence level and thermal stratification. In general, the simulation was able to reasonably reproduce experimental data for mean flow and thermal field. In comparison with the Smagorinsky sub-grid turbulence model, the dynamic model was to yield mean flow quantities that are in rather good agreement with the measured data, although not as good for some turbulence statistics. The discrepancies between the experimental data and the computed results in the outer part of the boundary layer suggest that special attention should be paid to the flow physics and numerical treatment in this region.

Gassowski *et al.* (2003), analyzed through DNS an air-filled cubical cavity at $Ra_H = 10^5$ up to 3×10^8 . The governing equations were integrated in time using a second-order Euler scheme with explicit treatment of the non-linear terms via a second-order Adams-Bashforth

scheme. Two spatial discretizations were compared: a finite difference technique using a staggered non-uniform grid and a Tchebychev spectral method. Results of vorticity and maximum velocity magnitudes were compared with results available in the literature. They concluded that when starting from the previous unsteady solutions and increasing the Rayleigh number, another transition was found to take place in the range $[6.5 \times 10^7, 7 \times 10^7]$, which leads to a steady regime that has not yet been reported in the literature. Moreover, multiple steady solutions were obtained for $Ra_H = 10^8$. All these solutions are characterized by non-oscillating longitudinal vortices.

In relation to the present thesis, the works of Soria *et al.* (2004) and Trias *et al.* (2007) stand out. Each one of such studies performed DNS within an air-filled rectangular cavity with relative height, width, and depth dimensions of 4, 1, and 1, respectively, and compared 2-D and 3-D solutions. Soria *et al.* (2004) solved the flow inside the same previously adopted cavity at $Ra_H = 6.4 \times 10^8$, obtaining results for: instantaneous temperature maps corresponding to the statistically steady state, averaged flow field (streamlines, isotherms, mean velocity and temperature profiles), averaged and instantaneous local Nusselt numbers and second order statistics. The authors concluded that with respect to the 2-D and 3-D results, their first-order statistics were very similar, in particular, the averaged local and overall Nusselt numbers; however, this was not the case for second-order statistics, which were substantially different (by two orders of magnitude in certain cases), far beyond the possible numerical inaccuracies. At the vertical boundary layers, the 2-D simulation incorrectly predicts very low values for all the second-order statistics. Hence, if direct numerical simulations of buoyancy-driven flows are to be used to develop or enhance RANS turbulence models, the assumption of two-dimensionality is not valid. Figure 2.2 shows the comparison between the 2-D and 3-D solutions for velocity and temperature profiles.

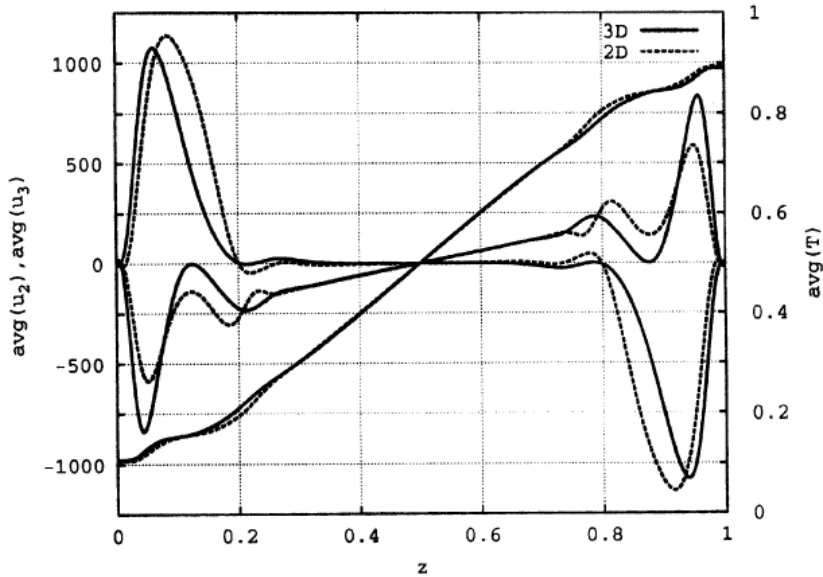


Figure 2.2- Averaged profiles at cavity mid-height, $Y = 0.5$ and $Z = 0.5$, of horizontal velocity (u_2), vertical velocity (u_3), and temperature (T). Source: Soria *et al.*, (2004).

Trias *et al.* (2007) analyzed the flow for three values of Ra_H (6.4×10^8 ; 2×10^9 and 10^{10}). The obtained results were the main features of the flow, including: the time-averaged flow structure, the power spectra, and the probability density distributions of a set of selected monitoring points, the turbulent statistics, and the global kinetic energy balances. In addition, the internal wave motion phenomena were described and discussed. They concluded that all simulations predict some basic flow features: a stratified cavity core, recirculating structures near the downstream corners, and thin vertical boundary layers that remain laminar at their upstream part, up to a point above the mid-height where transition occurs. With respect to centerline dimensionless thermal stratification, all the numerical simulations predicted values close to 1, whereas experimental studies yielded values of about 0.5. These results confirm the conclusions of Salat *et al.* (2004), which discard the three-dimensional effects as a possible reason for these discrepancies. Understanding the origins of these differences seems an interesting area for future work. With respect to the comparison between two- and three-dimensional results, the time-averaged flow structures are similar, in particular, regarding the averaged local and overall

Nusselt numbers. However, significant differences are observed in the flow dynamics. For the range of Rayleigh numbers investigated here, second-order statistics are significant only on the downstream corners of the cavity. Two-dimensional simulations may be enough, as a first and less computationally demanding approach, to capture the general features of buoyancy-driven flows in enclosed cavities at Rayleigh numbers up to 10^{10} . However, three-dimensional simulations are necessary for an accurate description of the flow, especially for turbulent statistics.

Trias *et al.* (2010), using the same cavity as in their previous works, obtained a set of DNS solutions ($Ra_H = 6.4 \times 10^8, 2 \times 10^9, 10^{10}, 3 \times 10^{10}$ and 10^{11} , $Pr = 0.71$) to cover a relatively wide range of Rayleigh numbers from weak to fully developed turbulence. Significant changes were observed for the highest Ra_H for which the transition point at the boundary layers clearly moves upstream. Such displacement increases the top and bottom regions of disorganization, shrinking the area in the cavity core where the flow is stratified. Consequently, thermal stratification values are significantly greater than unity (1.25 and 1.41, respectively for the two highest values of Ra_H). The heat transfer has been analyzed by obtaining a power-law scaling, $Nu = 0.182Ra_H^{0.275}$, which has an exponent far too small compared to the classical $1/3$ exponent. Regarding the flow dynamics, it was observed that the vertical boundary layers remain laminar or quasi-laminar on their upstream parts throughout the range of Ra_H investigated. Then, periodic oscillations in the form of Tollmien-Schlichting waves are amplified, triggering non-linear effects and provoking transition from laminar to turbulent flow regime. Those eddies ejected from the boundary layer are responsible for the large-scale mixing effect in the hot upper and cold lower regions. However, their energy is rapidly passed down to smaller scales and their influence is constrained to the vertical boundary layer when Ra_H is increased.

Kizildag *et al.* (2010) questioned the validity of the Boussinesq approximation with reference to 2-D LES and DNS simulations in a rectangular water filled-cavity with a vertical aspect ratio of $AR_v = 6.68$, $Ra_H = 2.2 \times 10^{11}$ and $Pr = 3.42$. Heat transfer and first and second order statistics were studied. The authors highlighted that simulations in water-filled cavities are much more complicated than in air-filled cavities, as the boundary layer becomes thinner for water under the same conditions. Consequently, very refined space and time discretizations are required for solving the three-dimensional and time-dependent flow, in order to capture the smallest scales of the turbulent flow. An

important conclusion for simulations at this Prandtl number is that the flow asymmetry disappears when the Boussinesq approximation is used.

2.3 CONCLUDING REMARKS

At this point it is worth comparing the objectives specified for this master's thesis and the results reported in the literature. Following that, the contributions sought in this work will become clear.

In experimental investigations, the majority of the aforementioned works employed air-filled cavities at $Ra_H > 10^9$ (Mergui and Penot, 1997; Tian and Karayiannis, 2000; Ampofo, 2004; 2005; Salat, 2004; Saury, 2011). These authors measured velocity and temperature mean profiles as well as their fluctuations. Some of them also measured the heat transfer and the wall shear stresses on the isothermal walls.

Different fluids were also employed, such as: silicone oil, $Pr = 457$ (Hsieh and Yang, 1996) and water (Schöpf and Patterson, 1996). Both works analyzed the unsteady flow in differentially heated cavities. The former work obtained the transient temperature distribution as well as the flow pattern history. The latter obtained a time series of images to describe flow development until the steady state is reached.

In the numerical analyses, most authors analyzed air-filled cavities ($Pr = 0.71$). In this group, DNS is the most widely applied approach (Janssen and Henkes, 1996; Gassowski *et al.*, 2003; Soria *et al.*, 2004; Salat, 2004; Trias *et al.*, 2007; 2009). Other approaches were also employed, such as LES (Peng and Davidson, 2001) and RANS (Dol and Hanjalic, 2001). Kizildag *et al.* (2010) used 2-D LES and DNS simulations to study a water-filled cavity and concluded that the flow symmetry disappears when employing the non-Boussinesq approximation in the momentum equations. The symmetry is a typical feature of air-filled cavities using the Boussinesq approximation.

To the author's knowledge, there are no experimental measurements of velocity distribution and turbulence analysis in a water-filled cavity at high Rayleigh numbers, such as 10^{10} . Therefore, the present work can contribute to the literature by providing experimental data about the flow behavior when employing a very challenging fluid, numerically speaking, as pointed out by Kizildag *et al.* (2010).

3. EXPERIMENTAL SETUP

This chapter describes the experimental setup and equipment used for measurements of temperature and flow velocity.

3.1 OVERVIEW OF THE EXPERIMENTAL APPARATUS

A test rig was carefully designed and constructed in order to perform the study of turbulent natural convection phenomena in cavities. Figure 3.1 presents a schematic diagram of the experimental apparatus.

As indicated in Figure 3.2, the experimental apparatus is formed by several components: Laser Doppler Velocimetry (LDV), cavity, vibration isolator, displacement device, radiation shield, temperature control system, and sensors to measure the temperature. A description of each one of such components will be presented in following sections.

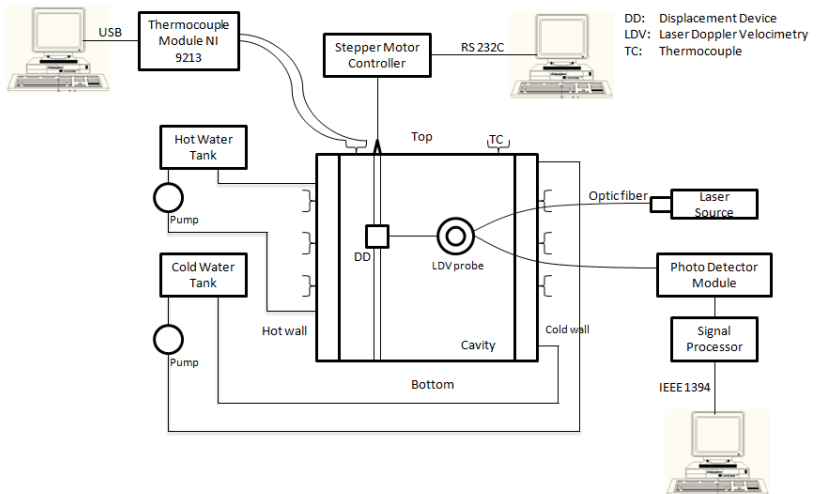


Figure 3.1- Schematic diagram of the LDV experimental apparatus.

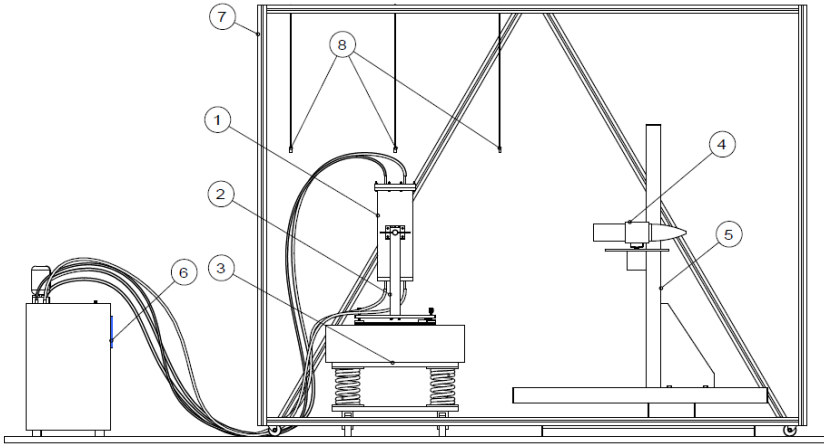


Figure 3.2- 1) Cavity; 2) Support; 3) Vibration Isolator; 4) LDV probe; 5) Displacement Device; 6) Thermal baths; 7) Radiation Shield; 8) Room thermocouples.

3.2 LASER DOPPLER VELOCIMETRY

Laser Doppler Velocimetry (LDV) is an optical technique employed for point measurements of velocity and turbulence distribution in both free and internal flows. Unlike other measurement techniques, LDV has specific benefits that allow it to be used for single- and multi-phase flows, including: non-intrusiveness, directional sensitivity, high spatial and temporal resolution, and high accuracy. For these reasons, the LDV technique enjoyed immediate acceptance after its introduction into academia for research applications, and this is well described by Albrecht *et al.* (2002).

LDV measures the velocity of small particles moving within the fluid of interest. Specifically, LDV is an indirect velocity measurement technique through the detection of inhomogeneities in the fluid flow by the use of seeding particles¹. The seeding particle motion represents the fluid flow velocity only if there is no appreciable discrepancy between the motion of the particles and the fluid. Therefore, the chosen particles should have a geometry that is as spherical as possible and a density similar to that of the surrounding fluid in order to avoid fluctuating forces (buoyancy or precipitation).

¹ The signal from natural particles is often poor and a high index of refraction seeding material may be necessary.

To measure the movement of the seeding particles, two laser beams are intersected within the fluid to create a measurement volume. The intersection of these two laser beams results in a fringe pattern; a series of light and dark laser light fringes (see Figure 3.3). When the particles move within the measurement volume, they directly alter the laser fringe pattern relative to their motion, e.g., the particle scatters light when it crosses a bright fringe, but does not scatter light when it crosses a dark fringe. This results in a fluctuating pattern of scattered light intensity with a frequency proportional to the particle velocity. Each individual pair of laser beams can measure a single direction of the velocity vector. Using two or more pairs of laser beams, one is able to make measurement volumes in different planes, and simultaneously collect multiple components of the velocity.

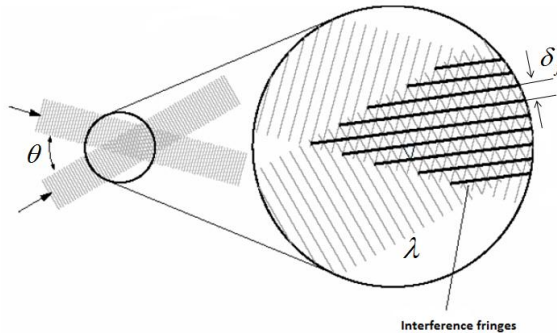


Figure 3.3- Formation of interference fringes.

The fringe displacement of the seeding particle is collected by a sensor that converts the light signal into an electrical frequency signal. Because the distance between fringes (δ_f) and the time for the particle to travel from one fringe to the next (inverse of signal frequency - $1/f_D$) are known, the measured signal frequency can be converted to velocity by using Equation 3.1:

$$U_p = \delta_f f_D \quad (3.1)$$

where f_D is known as the Doppler frequency and δ_f is the fringe spacing. (LDV Operational Manual -TSI, 2006) The fringe spacing is defined by the optics (Equation 3.2), where λ is the wavelength of the incident beams and θ is the angle between them.

$$\delta_f = \frac{\lambda}{2 \sin(\theta/2)} \quad (3.2)$$

When the measurement volume is made by two beams with identical frequency, the signal generated (frequency) by the particles moving in either forward or reverse direction will produce identical signals. This prevents the possibility of determining whether the velocity is positive or negative. To overcome this problem, a technique known as frequency shifting is used, where one of the beams has its frequency shifted by a Bragg cell of ~40 MHz. This results in interference fringes that are moving at a rate of 40 MHz in the measurement volume. With frequency shifting, it is possible to distinguish negative velocities. The particles crossing the measurement volume will have a frequency either above or below 40 MHz, depending on their direction. If a particle is moving against the fringes, it will have a frequency of 40 MHz plus the Doppler frequency (the frequency due to the particle velocity), and if a particle is moving in the same direction of the fringes, it will have a frequency of 40 MHz minus the Doppler frequency.

With this method, it is also possible to measure velocities near zero, because without the motion of the fringes there would be no light scattered from slow-moving particles. The LDV system can be divided into three components: the laser source, the optical system, and the acquisition/signal processing system. (see Figure 3.4)

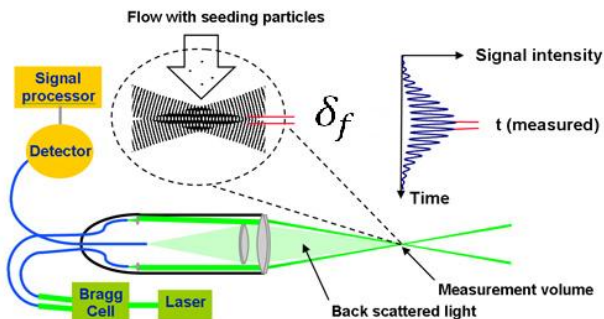


Figure 3.4- Flow measurement technique using an optically fixed measurement volume. (Cunha and Silva, 2000)

3.2.1 Laser Source

A laser source should produce coherent light with the following features: tightly focused, stable frequency and wavelength, and sufficient power for the application of interest. The laser source used in the LDV system adopted in the present study is the Argon Ion Continuous Wave (CW) Laser (Coherent Inc., model INNOVA 70C-3, 3 W power output). This laser source configuration uses water for cooling in order to maintain the equipment within an acceptable range of working temperature.

3.2.2 Optical System

The main purposes of the optical system are to divide the laser beam generated by the laser source into two or more beams, and to lead them to a known position defined as the measurement volume where the beams intersect each other, and then to capture the Doppler Effect generated by the interaction between the particles and the laser beams.

The separation of the each pair of beams is made by the Fiberlight multicolor Beam Separator (TSI Inc., model FBL-3), as depicted in Figure 3.5. The system output contains three pairs of beams: green (514.5 nm), blue (488 nm), and violet (476 nm). Each pair includes a frequency shifted beam and an unshifted beam. For the present work, only the first two pairs are used: the green and blue, in order to measure the horizontal and vertical components, respectively.

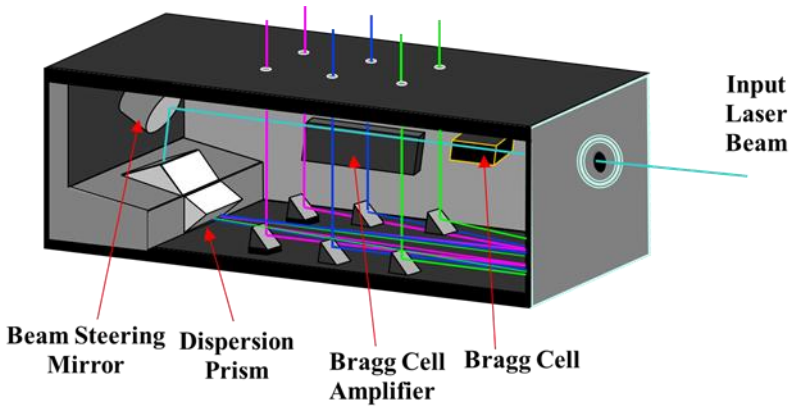


Figure 3.5- Beam separator with three output pairs of beams: green, blue and violet. (TSI, 2008)

The output laser from the beam separator is led to the probe through the fiber optics. The probe used is the TR 60 Series (TSI Inc., model TLN06-363) with specifications according to Table 3.1. The fiber optic probe is the sensor for the LDV system and for this configuration can make two-component velocity measurements. The probe used is designed not only to generate the measurement volume, but also to be responsible for collecting the scattered light signal from particles passing through this volume by using a photodetector. The photodetector is placed inside the probe (backscatter configuration).

Table 3.1- Specifications of the Fiber optic Probe model TLN06-363. (TSI, 2007)

	Horizontal component	Vertical component
Probe beam diameter (mm)	2.65	2.65
Probe beam spacing (mm)	50.0	50.0
Lens focal length (mm)	349.7	349.7
Numerical aperture	0.085	0.085
Beam-crossing half-angle ($^{\circ}$)	3.95	3.95
Measurement volume diameter (μm)	90	85
Measurement volume length (mm)	1.31	1.24
Fringe spacing (μm)	3.73	3.54
Number of fringes	24	24

3.2.3 Acquisition and Signal Processing Systems

The signal captured is directed towards a photomultiplier that converts the optical signal into an electrical signal. This process is performed by the Photo Detector Module (PDM) (TSI, Inc., model PDM-1000). After this, the output signal from the PDM is used in the signal processing system to obtain the frequencies from the electrical signals and then these results are sent to a computer. This process is performed by the Flow Size Analyzer (TSI, Inc., model FSA-4000). The computer processes the frequencies and then obtains quantities, such as velocities, turbulence intensity and so on, through use of the FlowSizer software (TSI, Inc., version 2.0.3.0).

3.3 PARTICLE IMAGE VELOCIMETRY

Particle Image Velocimetry (PIV) is a non-intrusive flow measurement technique that provides velocity information on a fluid in motion. The fluid is traced with seeding particles, which are assumed to faithfully follow the fluid motion. For such an assumption, a proper selection of the seeding particle type is dependent upon the nature of the flow of interest. Using the correctly selected particles, a fluid section (in 2D PIV) is illuminated by a laser sheet, such that the particles are visible in this plane of interest. The velocity vectors are obtained by taking two images shortly after each other and calculating the distance traveled by individual particles within this time. From the known time difference and the measured displacement, the velocity can be calculated. A CCD camera is used to store the first image (frame) quickly enough in order to be ready for the second exposure.

The four basic components required for a PIV measurement are:

- An optically transparent test section containing the flow seeded with particles;
- A light source (laser) to illuminate the region of interest;
- Recording hardware;
- A computer with software to process the recorded images and extract the velocity information from the particle positions.

Figure 3.6 shows a typical PIV system, and a detailed description of the PIV components can be found in Raffel *et al.* (2007).

The optically transparent test section comprises the cavity itself, which is illuminated by a laser sheet from the top. The images are captured normal to the laser sheet by a CCD camera and recorded into a computer through a frame grabber.

The laser source is a Q-switched Nd: YAG (Dantec, Inc., model Dual Power 200-15). This laser produces 200 mJ per pulse with a repetition rate of 15 Hz and a wavelength of 532 nm. The CCD camera is fully synchronized with the pulsating laser. The CCD camera employed is a FlowSense (Dantec, Inc., model 4M Mk2) with a frame grabber PCI-Express (CameraLink, Inc., single channel). The software employed to process the recorded images is Dynamic Studio (Dantec, Inc., version 3.31.22). Figure 3.7 shows a schematic diagram of the PIV experimental apparatus.

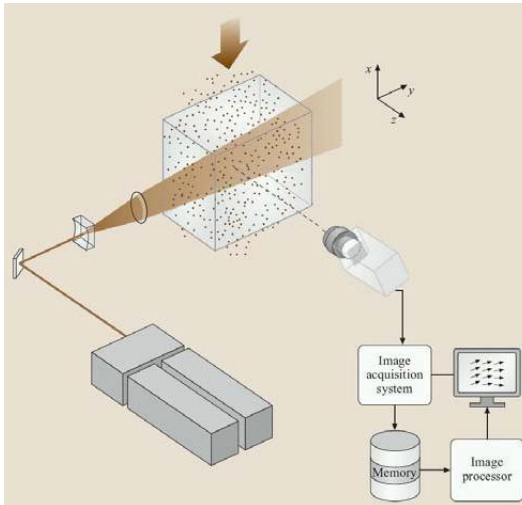


Figure 3.6- Schematic of a typical PIV measurement system (Blonski *et al.*, 2008).

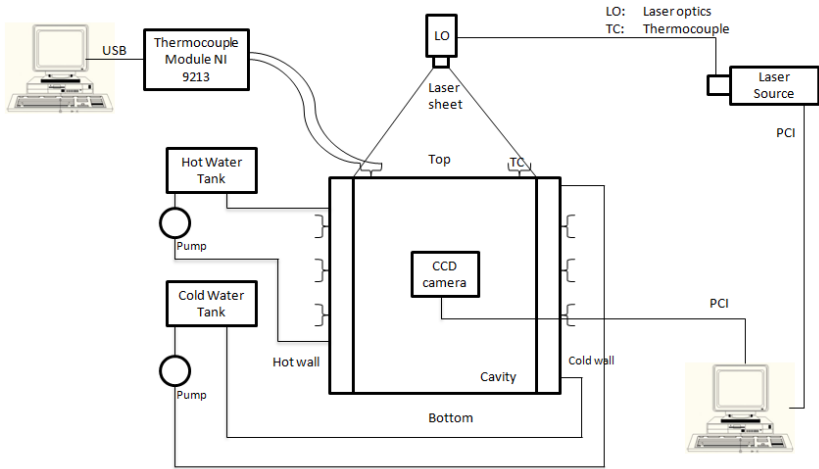


Figure 3.7- Schematic diagram of the PIV experimental apparatus.

3.4 SEEDING PARTICLES

One of the most important aspects of LDV and PIV is the appropriate choice of seeding particles. Many experimentalists rely on particles naturally present in the flow, e.g., solid particles within tap water. However, it is desirable to carefully select suitable particles with which to seed the flow in order to obtain adequate data rates.

As already mentioned, the LDV and PIV techniques determine fluid velocity indirectly from the particle's velocities. In order to avoid any discrepancy between the motion of the particles and that of the fluid, it is necessary to analyze the main sources of discrepancy between these motions, as discussed by Tarozzi (2007):

1. Difference of dynamic response between the particles and the fluid;
2. Influence of gravitational acceleration.

The first aspect can be analyzed with reference to the solution of a simple case represented by a rigid single particle inside a non-confined fluid, neglecting the weight of the particle. The governing equation of motion of the particle is given by Equation 3.3:

$$\vec{F}_D = m_p \frac{d\vec{U}_p}{dt} \quad (3.3)$$

where \vec{F}_D is the drag force of the fluid over the particle, m_p is the mass of the particle, and \vec{U}_p is the velocity of the particle. In the case of a spherical particle at a very small Reynolds number, $Re_p = \rho_p |\vec{U}_f - \vec{U}_p| d_p / \mu_f \ll 1$, the drag force is obtained by Stokes' Law through Equation 3.4:

$$\vec{F}_D = 3\pi\mu_f(\vec{U}_f - \vec{U}_p)d_p \quad (3.4)$$

In this equation, ρ_p is the fluid density, \vec{U}_f and \vec{U}_p are the velocity vectors of the fluid and particle, respectively, d_p is the diameter of the particle, and μ_f is the dynamic viscosity of the fluid. In the case of the particle moving in the same direction as the fluid, the motion is described by Equation 3.5:

$$\frac{\rho_p d_p^2}{18\mu_f} \frac{d\vec{U}_p}{dt} + \vec{U}_p = \vec{U}_f \quad (3.5)$$

The motion of a particle can be seen as a first order system dependent of a single parameter, the characteristic time τ_p , and it is given by Equation 3.6:

$$\tau_p = \frac{\rho_p d_p^2}{18\mu_f} \quad (3.6)$$

We can solve Equation 3.5 by using different initial conditions; for the particular case in which the particle is initially stationary, $\vec{U}_p(t=0) = 0$, and its velocity is given by Equation 3.7:

$$U_p = U_f(1 - e^{-t/\tau_p}) \quad (3.7)$$

Figure 3.8 shows the dynamic response of spherical Polyamide seeding particles (Dantec Dynamics Inc., PSP-5,20,50) with different nominal diameters ($\rho_p = 1030 \text{ kg/m}^3$, $d_p = 5, 20, 50 \text{ }\mu\text{m}$), which are initially stationary $\vec{U}_p(t=0) = 0$ and introduced into a water flow,

$\mu_f(T_o = 23^\circ\text{C}) = 9.326E - 04 \text{ kg}/(\text{m}\cdot\text{s})$, that has velocity equal to U_f .

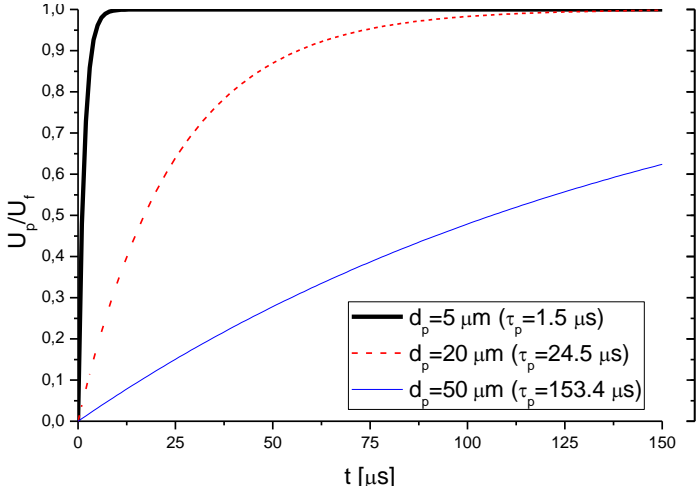


Figure 3.8- Dynamic response of spherical Polyamide seeding particles with different nominal diameters.

The previous considerations applied for non-spherical particles are only valid if the regime is $Re \ll 1$ (Stokes regime), and the size of the particles is uniform in all directions. Some discrepancies in the behavior of the particles are found when increasing the Reynolds number; for an accurate analysis, expressions for the coefficient of friction for different geometries and different flow regimes are available in the literature (Loth, 2010).

In a similar way, the motion of the particles under the effect of gravitational acceleration can be predicted. When the density of the particle is different to that of the fluid, fluctuating forces (buoyancy or precipitation) induce irregular motion, which must be avoided if the particles are to faithfully follow the fluid flow pattern. The governing equation of motion of a single particle, heavier ($\rho_p > \rho_f$) and rigid, in a vertical motion with constant velocity U_f , is described by Equation 3.8:

$$\vec{F}_D + \vec{W}_p - \vec{B}_p = m_p \frac{d\vec{U}_p}{dt} \quad (3.8)$$

where \vec{W}_p and \vec{B}_p are the weight and buoyancy force of the particle, respectively. Assuming that the particle is spherical and that it is possible to apply Stokes' Law (Equation 3.4), the governing equation of motion can be determined from the solution of Equation 3.8, when using an initial condition. The flow reaches steady conditions after a transient initial period (typically, $t > 6\tau_p$), the relative particle velocity will reach a velocity described by Equation 3.9:

$$(U_p - U_f)_\infty = (1 - 1/\gamma)g\tau_p \quad (3.9)$$

where γ is the ratio between the densities of particle and the fluid ($\gamma = \rho_p/\rho_f$). From Equation 3.9, it is easy to see that if one wants to reduce the relative velocity between the particle and the fluid, it is necessary to reduce the difference between the densities ($\gamma \approx 1$) and also to reduce the diameter of the particle.

However, the choice of seeding particle cannot be limited solely to fluid-mechanics considerations; it is also necessary to evaluate the properties of light reflection. The light scattered by the seeding particles is a function of the ratio of the refractive index of the particles to that of the surrounding medium, and of the particle's size, shape, and orientation. A greater relative refractive index and larger geometric particle size both help improve signal strength, where the relative index is $m = n_p/n_f$ ¹ (Seed Particles for LDV and PIV-TSI, 2006).

The light scattering depends on polarization and observation angle. For spherical particles with diameter d_p , larger than the wavelength of the incident light λ , Mie's scattering theory can be applied to describe the light reflection. Mie scattering can be characterized by the normalized diameter q , defined as $q = \pi d_p/\lambda$. Figure 3.9 shows the polar distribution of the scattered light intensity for monochromatic light ($\lambda = 0.488 \mu\text{m}$) for three different particle diameters. This figure shows that the scattered light intensity is strongly dependent on the direction, and that the maximum scattered light is always in the forward reflection (forward scattering, $\theta = 0^\circ$). However, a local maxima can also be observed in the back reflection (backscattering, $\theta = 180^\circ$). There is a tendency for the scattered light intensity to increase with increasing particle diameter. However, the number of local maxima and minima is proportional to q ; if q is larger

¹ n_p and n_f are the refractive indexes of the particle and the fluid respectively.

than unity, approximately q local maxima appear in the angular distribution over the range from 0 to 180°.

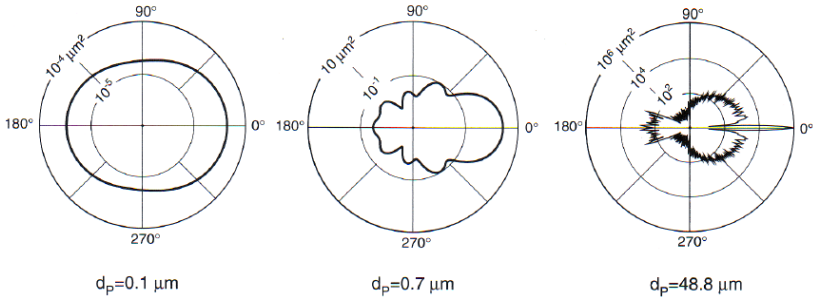


Figure 3.9- Light scattering of a hollow glass sphere in air for three different diameters according to Mie's theory ($\lambda = 0.488 \mu\text{m}$). The polar scale is logarithmic (Tarozzi, 2007).

Raffel *et al.* (2007) noted that small particles follow the fluid motion with greater efficiency; however, the particle diameter should not be too small, because the light scattered by the particle increases with its size. Hence, a compromise has to be found when selecting the seeding particles in order to obtain adequate quality images for PIV, and this can also be applied to LDV, as the velocity in this technique is obtained via light scattered by a tracer particle.

3.5 CAVITY

The main goal of this work is to obtain an internal flow with a high Rayleigh number of the order of magnitude of $Ra \sim 10^{10}$. The vertical wall temperatures were fixed at 28 °C and 18 °C (T_h and T_c , respectively), and the experiment was tested in a temperature-controlled room at 23 °C. By maintaining the working temperature¹, T_o , to be the same as the room temperature, heat losses through the ideally adiabatic walls can be reduced. Furthermore, the small temperature difference between the vertical walls (10 °C), combined with the low emissivity of the aluminum material selected for the manufacture of the heated walls, allows us to neglect radiation heat transfer.

¹ Working temperature is defined as $T_o = (T_h + T_c)/2$.

The adiabatic walls are made of acrylic because of its desired insulation properties, such as low absorption coefficient¹ (the laser energy losses are minimal), and low thermal conductivity.

After the definition of the preceding parameters, the dimensions of the cavity must be defined, and also an analysis of the possible fluids must be performed. Water was chosen as the working fluid for the experiments. In Figure 3.10, it is demonstrated through Equation 2.1 that the desired value of the Rayleigh number ($\sim 10^{10}$) is first reached at $H = 400$ mm when using water and helium as the working fluids. In general, other fluid options require greater treatment than water. Figure 3.11 shows that by fixing the cavity height at $H = 400$ mm, the cavity must be pressurized to 2 atm and 3.4 atm when employing R134a and xenon, respectively as the working fluid. This results in very high stresses in the cavity due to the high pressure when compared with water. Furthermore, water is cheap, non-flammable and non-toxic. For these reasons, deionized water was determined to be the ideal fluid for the experiments. The process of deionization consists of removing the salts, which are the major source of impurities in tap water.

After the definition of the cavity height, the width and depth are also defined. The aspect ratio (height:width) of the present work is already established as four; thus, obtaining a width of 100 mm. The thickness of the adiabatic walls is 32 mm. Figure 3.12 shows the manufactured cavity with a squared base attached to its support.

¹ The absorption coefficient determines how far into a material the light of a particular wavelength can penetrate before it is absorbed. In a material with a low absorption coefficient, light is only poorly absorbed, and if the material is thin enough, it will appear transparent to that wavelength.

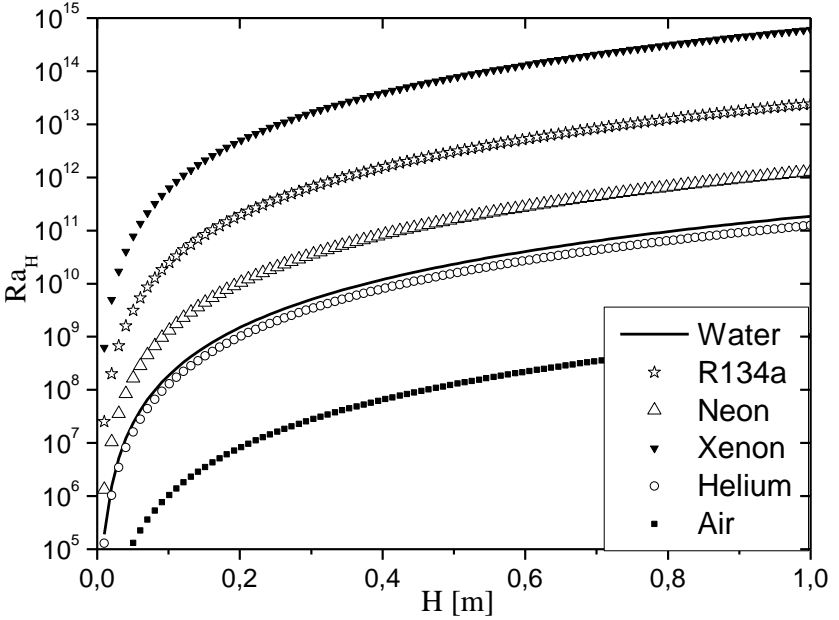


Figure 3.10- Rayleigh number \times Characteristic length (H), $T_H = 28^\circ\text{C}$, $T_C = 18^\circ\text{C}$, $\Delta T = 10^\circ\text{C}$, $P = 1\text{ atm}$.

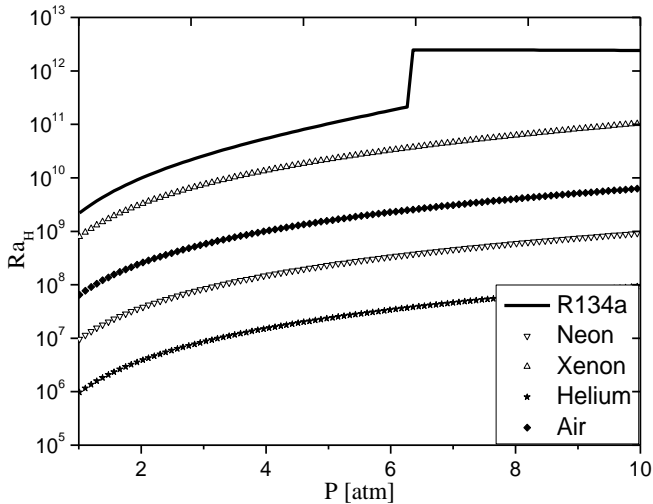


Figure 3.11- Rayleigh number \times Pressure, $T_H = 28^\circ\text{C}$, $T_C = 18^\circ\text{C}$, $\Delta T = 10^\circ\text{C}$, $H = 400\text{ mm}$.

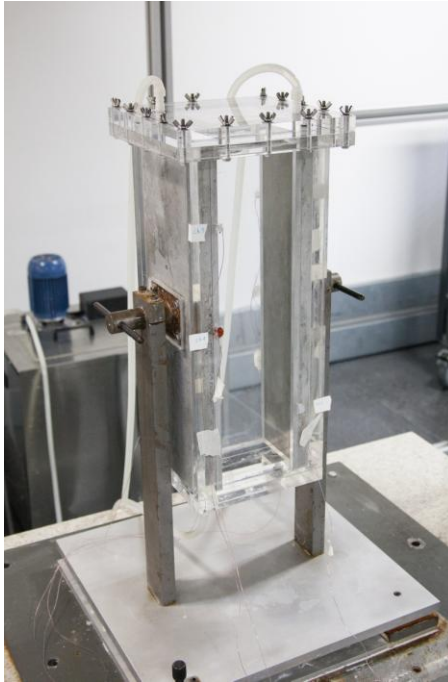


Figure 3.12- Cavity used in this work.

3.5.1 Temperature Control System

The temperature control system maintained a constant temperature flow to the opposite lateral walls ($x = 0$ and $x = W$) by using two thermoelectric baths (Quimis, Inc., model Q214M), whose specifications are listed in Table 3.2.

Table 3.2- Specifications of thermoelectric bath. (Quimis, 2010)

Temperature range	-20 to 120 °C
Tank capacity	8 L
Thermal sensor	PT100 encapsulated in stainless steel with 0.1 °C sensitivity
Volume flow rate	10 L/min
Cooling capacity	3000 btu/h

The hot and cold solutions were pumped through the opposite lateral walls at a rate of 10 L/min (nominal). Each wall was machined to have a serpentine-like channel, depicted in Figure 3.13, to deliver the

heated or cooled water to all extensions of these isothermal lateral walls. Silicon tubes were used to close a circuit flow between the isothermal walls and the baths because of two important characteristics: heat insulation, and the capacity of absorbing the vibration from the bath. The solution was a mixture of 7 L of water and 1 L of ethylene glycol, which decreased the freezing point and raised the boiling point of the liquid to -5 and 102 °C, respectively. Although the working temperatures are far from these points, when using pure water, the water temperature level needs constant monitoring, whereas using this solution, this concern can be neglected.

The serpentine channel, combined with the high thermal capacity and thermal conductivity of the aluminum walls, allowed us to maintain them at constant and uniform temperatures. Figure 3.14 shows an illustration of the two serpentine-like channels filled with hot and cold fluid from the thermal baths.

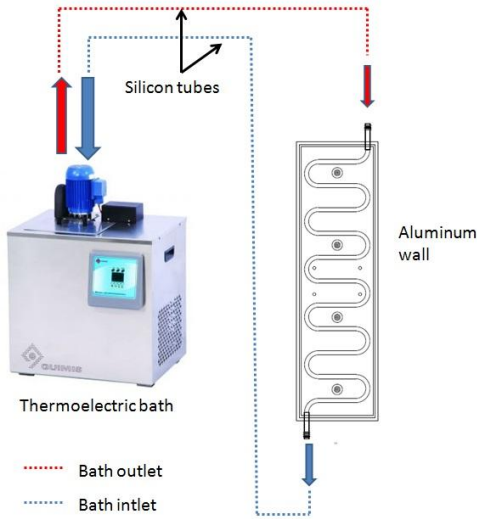
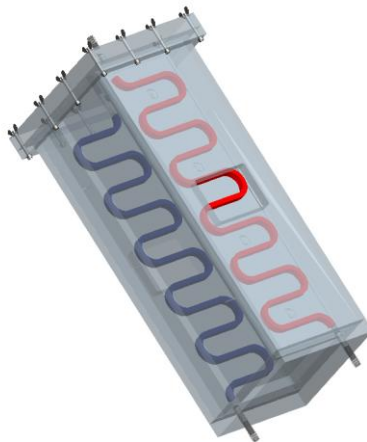


Figure 3.13- Closed circuit flow between bath and isothermal wall.



SCALE: 1:1 TYP: ASSEMBLY DRAWING SHEET NO. 002-AS-001 OF 3

Figure 3.14- Illustration of the serpentine-like channels of the cavity to allow the hot and cold water to maintain, as far as possible, isothermal conditions of the walls.

3.5.2 Temperature Measurement

The temperature measurement can be divided into two parts: the measurement of the cavity walls, and the measurement of room temperature. These temperatures were continuously measured by means of T-type thermocouples (Omega, Inc.) and recorded by a 16 channel, 24 bit, USB portable data acquisition recorder (National Instruments, Inc., model NI USB-9213), using an automatic acquisition frequency of 1.0 Hz to sample the data. The temperature readings from the thermocouples are sent via the data acquisition system to the computer by means of an interface developed in LabView 6i.

In each isothermal wall there were 3 pairs of thermocouples, equally spaced along the cavity height. These holes were parallel to the z -axis (see Figure 3.15), and the centers of the holes were placed 3 mm from the surface of the internal wall.

In order to measure the room temperature, three thermocouples with thermal masses were installed; all of them hung in the radiation shield (see Figure 3.2). Table 3.3 identifies the thermocouples according to their place of measurement.

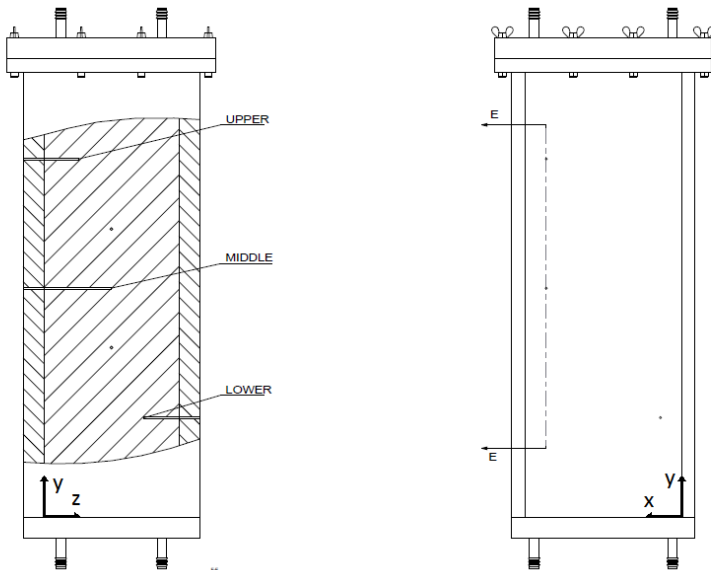


Figure 3.15- Detailed view of the thermocouple's channels.

Table 3.3- Corresponding thermocouple to the place of measurement.

	Position	Coordinates ¹ [mm]			Channels
		x	y	z	
Hot wall	Upper	0	320	20	TC1
	Middle	0	200	50	TC2
	Lower	0	80	80	TC3
Cold wall	Upper	100	320	80	TC4
	Middle	100	200	50	TC5
	Lower	100	80	20	TC6
Room	TC7, TC8, TC9				
Total number of thermocouple pairs	9				

3.6 AUXILIARY COMPONENTS

3.6.1 Vibration Isolator and Support

A vibration isolator system and support were designed for fixing the cavity and reducing vibration transmission from external sources by increasing the stiffness of the test rig. To reduce the natural frequency of the test rig, a 200 kg block made of concrete was attached over four isolators. A 100 kg steel plate with width, height, and depth dimensions of 650, 15, and 550 mm was attached to the top of the block.

The support, which is used to hold the cavity to give stability and repeatability, has two knobs to adjust the inclination of the two horizontal axes parallel to the x and z direction. Each knob has at its end a precision screw thread with a fine pitch resulting in a homogeneously smooth motion. Using a digital inclinometer with a resolution of 0.05° (Bosch, Inc., model DNM 120L) placed over the cavity and aligned parallel to the x and z -axis, it is possible to indirectly correct the inclination of the cavity. Natural convection problems in cavities are very sensitive to the inclination, because gravity is decomposed into different directions, which alters the dynamics of the flow. Figure 3.16 shows the setup of the cavity, support and vibration isolator.

¹ The thermocouple sensors are considered to be located on the heated walls surface ($x = 0$ and $x = W$). In reality, there is gap of the order of 3 mm between them and the walls.

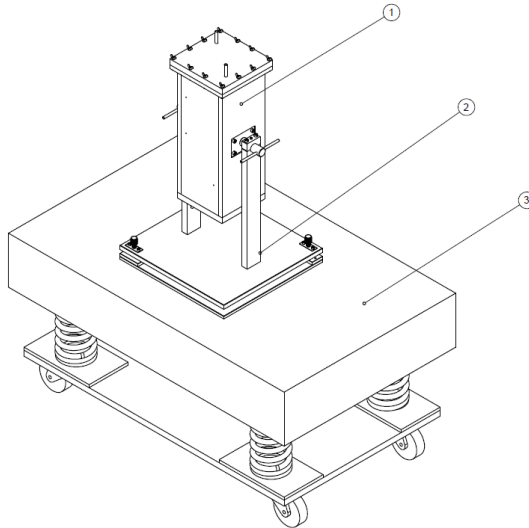


Figure 3.16- 1) Cavity; 2) Support; 3) Vibration Isolator.

3.6.2 Displacement Device

The LDV measurement was performed by positioning the probe in different positions in order to displace the measurement volume and capture the signal from the velocity in different profiles. To displace the probe, a 3D traverse (TSI, Inc., model T3DE) was employed, which consists of a three-axis ($600 \times 600 \times 600$ mm) displacement device controlled by a stepper motor. The traverse's specifications are shown in Table 3.4.

Table 3.4- Specifications of Traverse System. (TSI, 2006)

Unidirectional Repeatability (μm)	± 10
Accuracy (μm)	± 300 F.S.
Resolution (μm)	6.25

3.6.3 Radiation Shield

A radiation shield comprising an aluminum frame surrounded by a black plastic tarp was designed and manufactured to promote safety against the potential danger of the laser beams¹. In addition to the safety

¹ Exposure to the laser can cause severe skin burns and permanent eye damage.

concerns, it is also desirable to reduce the noise from other sources, such as the light signal from the background environment, as documented by Durrani (1972). In the beginning of the tests, the entire radiation shield was closed with the plastic tarp in order to perform some pretests. The valid measurements were performed with the radiation shield closed only at the top, and all the remaining faces open, in order to maintain the correct temperature of the testing room.

4. EXPERIMENTAL PROCEDURE

This chapter presents the experimental procedure adopted to acquire the experimental data of interest in the analysis of the flow. Special attention is given to procedures used to guarantee measurement accuracy.

4.1 MEASUREMENT PROCEDURE

The cavity was filled with water, and the seeding particles were introduced before starting the heating/cooling procedure of the vertical walls. Before the measurement procedures commenced, the system was left for 24 hours to reach steady state conditions, and the room illumination was turned off to avoid noise from the light signal of the background environment.

For the PIV measurements, the laser sheet was placed over the cavity, illuminating the mid-depth ($Z = 0.5$). The laser pulse separation between two frames was 0.33 s.

For the LDV measurements, for every measuring point, the LDV probe lasted for a period of approximately 8 min. The laser beams entered the cavity through the acrylic wall with an inclination to the isothermal wall; a more detailed description is presented in section 4.1.1. When laser beams pass through different mediums refraction occurs, and the influence of this in the coordinate system is analyzed in section 4.1.2.

The velocity and fluctuation distribution were measured at the cavity mid-plane ($z = 0.5D$) on a very fine non-uniform mesh. First, the velocity was measured at 9 different heights and for each height, at 118 points from the hot wall to the cold wall. The first three points were 0.25, 0.38, and 0.50 mm; from 0.50 to 2 mm from the wall, the velocity was measured at every 0.25 mm; from 2 to 15.5 mm, it was measured every 0.5 mm; and from 15.5 mm to the cavity center, the distance between consecutive measuring points was 1.5 mm. Finally, measurements were taken from the center to the cold wall, using the same coordinates but reversed. During all measurements, the experimental conditions were kept as steady as possible.

Experimental repeatability was verified by measuring a half profile on the hot wall side to the center of the cavity at $Y = 0.5$ and $Z = 0.5$. The three dimensionality of the flow was verified by comparing the velocity distribution at two different cavity depths, $Z = 0.5$ and 0.95. The results are presented in Chapter 5.

4.1.1 Measuring with a Tilted Probe

In order to take measurements near the heated walls, the probe had to be tilted by approximately 5 degrees (see Figure 4.1). The traverse-fixed coordinate system (x, y, z) with its corresponding velocity components u , v , and w is assumed to be aligned parallel to the wall. In the present work, a four-beam two-velocity system was employed, and a transformation had to be used to the horizontal component u . Accordingly, the transformation to the velocity components is given by Equations 4.1 and 4.2, as follows:

$$u = u_m \cdot \cos \theta_{tilt} \quad (4.1)$$

$$v = v_m \quad (4.2)$$

where u and v are the actual velocity components (corrected components), and u_m and v_m are the measured components, or the non-corrected quantities, and θ_{tilt} is the tilt angle of the probe.

The correction of the horizontal velocity fluctuations was not undertaken, because to perform this, it is necessary to obtain the velocity fluctuation in the z -direction (w'), and by using the present probe configuration this was not possible. One can find more detailed descriptions in Albrecht *et al.* (2003).

The tilting of the probe is done manually, and there is no accuracy in this procedure. For the configuration employed here, the correction for such a small tilt angle will result in a reduction in the order of 0.4% of the horizontal component of velocity. Albrecht *et al.* (2003) pointed out that the horizontal velocity fluctuation is only influenced over very small distances from the wall, beyond $y^+ \approx 5$ the effect can be neglected.

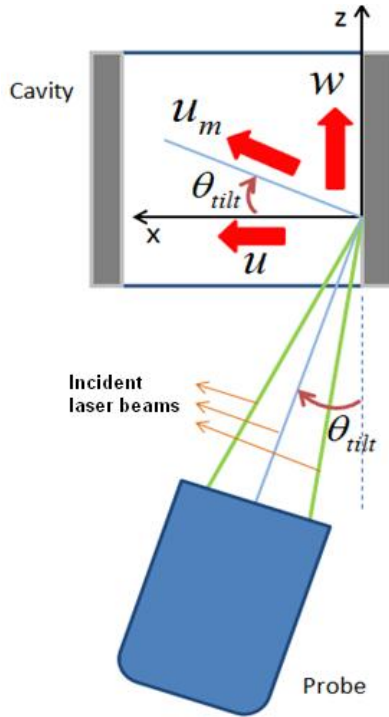


Figure 4.1- Incident laser beams from a probe tilted for measurement in the near-wall region.

4.1.2 Measuring Confined Fluids

When measuring confined flows, the laser beam has to pass through test sections with one or more windows. Generally, the refractive index of the window material is different from the air. This causes the beams to refract, which in turn changes the location of the measurement volume as depicted in Figure 4.2.

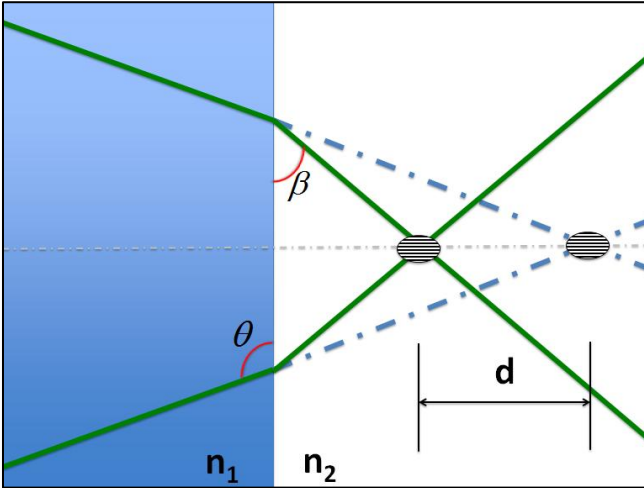


Figure 4.2- Refraction of two laser beams in two mediums.

Depending of the refractive index, the new position of the measurement volume will be closer or further from the inertial reference (window wall), this difference is due to an angular deviation of the crossing beam passing through the different mediums, which can be related by the refractive indexes of each medium. This phenomenon can be described the Snell's Law (Equation 4.3).

$$\frac{n_2}{n_1} = \frac{\sin\theta}{\sin\beta} \quad (4.3)$$

where:

n_1 = refractive index of medium 1;

n_2 = refractive index of medium 2;

θ = incidence angle;

β = refractive angle.

However, as the LDV probe is located in air, and the measurement volume is located inside the cavity, it is necessary to correct the effect of refraction through the interface air-acrylic-water, establishing the relationship between the distance traveled by the measuring volume and the LDV probe. The effect of refraction in the experiment is shown in Figure 4.3.

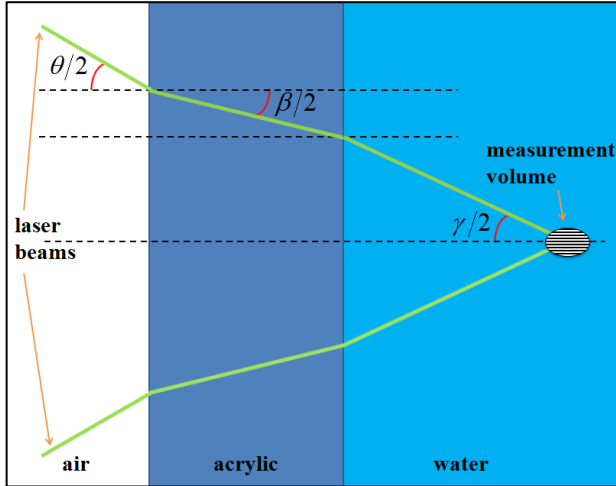


Figure 4.3- Refraction through the interfaces air-acrylic-water.

The refractive indexes of the materials are listed as follows:

- Refractive index of air, $n_a = 1.00$;
- Refractive index of acrylic, $n_w = 1.49$;
- Refractive index of water, $n_f = 1.33$.

Using the refractive indexes above for $\theta/2 = 3.95^\circ$, and applying Snell's Law from Equation (4.3):

$$n_a \sin\left(\frac{\theta}{2}\right) = n_w \sin\left(\frac{\beta}{2}\right) = n_f \sin\left(\frac{\gamma}{2}\right) \quad (4.4)$$

the values of $\beta/2$ and $\gamma/2$ are determined to be 2.65° and 2.97° , respectively.

Equation 4.5 gives the relation between the distance traveled by the LDV probe and the measurement volume, which is placed inside the cavity, as follows (Albrecht, 2003):

$$y_f - y_a = y_a \left(\frac{n_f}{n_a} - 1\right) + t \left(1 - \frac{n_f}{n_w}\right) \quad (4.5)$$

where:

y_f = disturbed position of the measurement volume, in mm;

y_a = undisturbed position of the measurement volume, in mm;

t = thickness of the window, in mm.

Figure 4.4 shows the behavior of the movement of one beam across the cavity interior. We are interested in the displacement of the measurement volume (y_f) with respect to the displacement of the probe (y_a). Therefore, we differentiate the expression (Equation 4.5) with respect to the distance to the window, obtaining Equation 4.6:

$$\frac{dy_f}{dy_a} = \frac{n_f}{n_a} = 1.33 \quad (4.6)$$

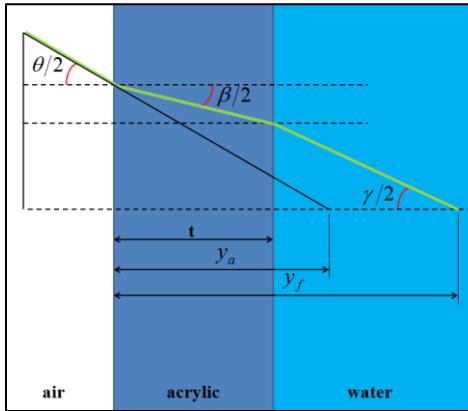


Figure 4.4- Behavior of the beam crossing the cavity wall.

This simply states that movement of the transmitting system normal to the plane window, translates into an amplified normal movement of the measurement volume within the cavity with an amplification of n_f/n_a . As an example, to traverse 100 mm of the measurement volume within the cavity (z direction) requires a traverse of the laser probe of only $100/1.33 = 75.2$ mm.

4.2 UNCERTAINTY ANALYSIS

For this work, there are two important quantities for which we must evaluate their uncertainties in order to express reliable data: temperature and velocity. The various input quantities for the calculation of Rayleigh number are analyzed separately in order to evaluate the standard uncertainty of this important parameter. A short review of the uncertainty evaluation procedure can be found in Appendix A.

4.2.1 Temperature

In order to determine the temperature uncertainty, it is necessary to consider all the calibration parameters and measurement repeatability (random error), and they are listed as follows:

- Bulb thermometer used as the standard reference;
- Calibration curve fitting;
- Repeatability of the measured temperatures.

The bulb thermometer (IncoTerm, Inc., model 5096) used as the reference had a scale from -10.7 to 50.7 °C and a resolution of 0.1 °C. The calibration report of the bulb thermometer is in Attachment A.

In order to achieve accurate readings from the thermocouples, a calibration procedure must be carried out. For this work, nine type-T thermocouples were calibrated by comparing their response with a standard bulb thermometer. For each thermocouple (or channel), the polynomial coefficients of Equation 4.7 must be determined:

$$T_{ref} = a_0 + a_1V + a_2V^2 + a_3V^3 + \dots \quad (4.7)$$

where T_{ref} is the temperature measured by the bulb thermometer (standard reference), and V is the voltage signal obtained by the thermocouple sensor. The calibration curve was obtained by means for the working range of temperatures from 17 to 29 °C.

The calibration procedure consisted of immersing all the thermocouple sensors and the bulb thermometer into a thermal bath. In order to avoid interference in the thermocouple readings all the sensors were introduced individually inside glass test tubes filled with machine oil. A polystyrene sheet was used to insulate the bath and to ensure that the temperature was as uniform as possible inside the bath, and also to keep the sensors and the bulb thermometer in a defined position allowing it to be partially immersed. This is a requirement for partial immersion thermometers. A schematic diagram of the calibration apparatus is presented in Figure 4.5. Figure 4.6 shows a picture of the bulb thermometer and the thermocouples immersed in the thermal bath during the calibration procedure.

The temperature from the standard thermometer was obtained directly from the thermal bath, after 30 minutes of stabilization, in each temperature within the chosen range. After stabilization, voltage signals were captured during a 15-second period with an acquisition frequency

of 1.0 Hz. This process was repeated from the lower to the higher temperature.

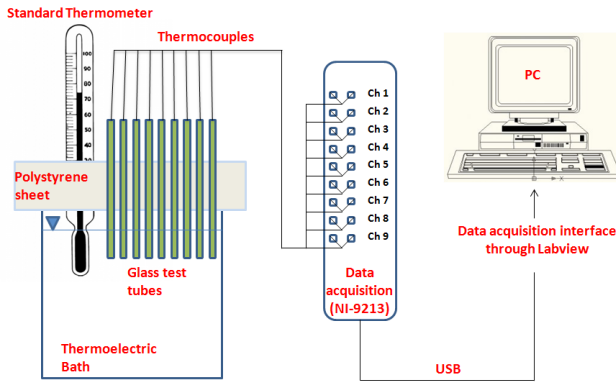


Figure 4.5- Schematic diagram of the thermocouple calibration apparatus.

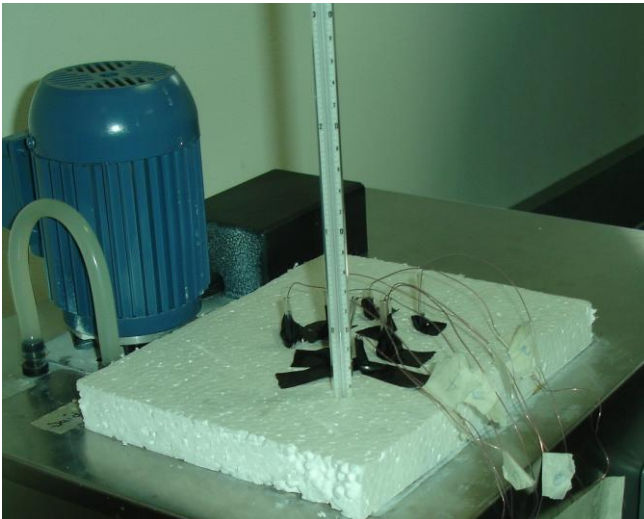


Figure 4.6- Experimental thermocouple calibration apparatus.

The tension signals obtained from the thermocouples during calibration as a function of the reference temperature measured by the bulb thermometer are shown in Figure 4.7. Using a linear curve fitting through the *Least Squares Method*, the obtained polynomial coefficients (from Equation 4.7) are shown in Table 4.1.

The result of the calibration process can be seen in Figure 4.8, which shows the temperature signals from all nine thermocouple channels. In the case of not using the calibration curve, or if one adopts the software fitting, the values will present a wider dispersion. On the other hand, the calibrated thermocouples will be more accurate (average temperatures are closer to the reference temperature) and the dispersion will be lower.

The final value assigned to the measured temperature depends on the quality of the curve fitting from the calibration data. Using Equation A.12, applied to a first degree polynomial, (see Figure 4.7) defines the uncertainty of the curve fitting, which for the various thermocouples is, on average, equal to 0.0449 °C.

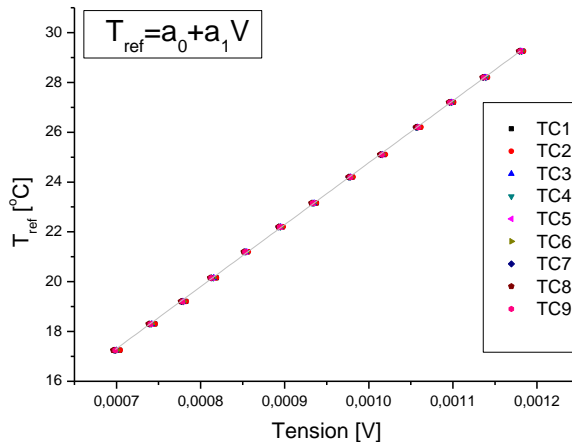


Figure 4.7- Thermocouple calibration curve.

Table 4.1- Polynomial coefficients for a linear curve fitting.

Thermocouple	a_0	a_1	R-square
1	-0.31502	25002.4962	0.99983
2	-0.29852	24967.9821	0.99984
3	-0.18169	24937.2617	0.99989
4	-0.10420	24855.4512	0.99989
5	-0.13549	24898.6823	0.99990
6	-0.18958	24947.3110	0.99987
7	-0.08068	24886.5904	0.99990
8	-0.04660	24865.6781	0.99989
9	-0.10362	24880.4440	0.99985

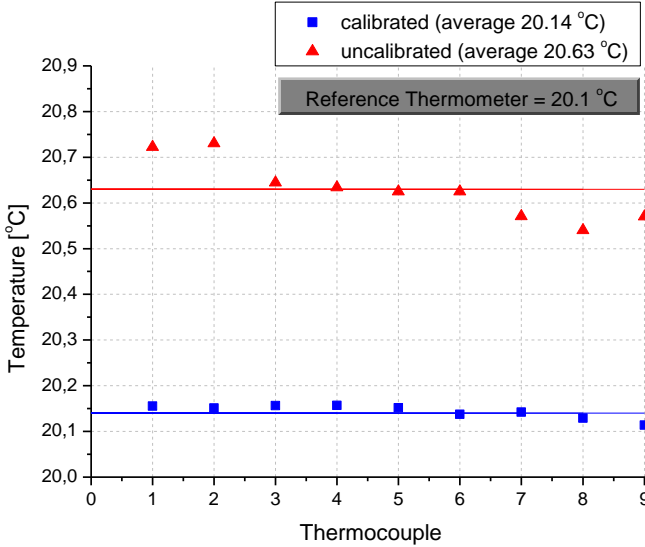


Figure 4.8- Results of the calibration procedures for all the thermocouples.

The repeatability of the temperature is given by the standard deviation of measurements in a typical test. In this work, the temperature measurement was performed before the measurement of each velocity profile, for a period of 1 min with an acquisition frequency of 1 Hz. Its uncertainty is defined by the rules of the Type A uncertainty (Equation A.4). The standard deviation of 60 measurements is, on average, $S = 0.02$ °C:

$$u(\bar{x}_i) = \frac{s(x_i)}{\sqrt{n}} = \frac{0.02^\circ\text{C}}{\sqrt{60}} = 0.0026^\circ\text{C} \quad (4.8)$$

Based on such data, the expanded uncertainty for measurements of temperature is given in Table 4.2:

Table 4.2- Combined standard uncertainty for temperature.

#	Description	Type	Value [°C]	Distribution	Divisor	u_i [°C]
1	Resolution	B	0.1	rectangular	$\sqrt{3}$	0.0577
2	Curve Fitting (calibration)	B	0.0449	-	1	0.0449
3	Repeatability	A	0.0026	normal	1	0.0026

4	Combined Uncertainty	$u_c(T) = \sqrt{\sum u_i^2}$	$\pm 0.073 \text{ }^\circ\text{C}$
5	Expanded Uncertainty confidence level of 95.45%)	$U(T) = k_p \cdot u_c(T)$	$\pm 0.2 \text{ }^\circ\text{C}$

4.2.2 Expanded Uncertainty

In most experimental investigations, several quantities are measured and the results of such measurements are used to calculate a sought quantity. For example, experimental values of density are usually determined by dividing the measured mass of a sample by the measured volume of that sample. Each measurement includes some uncertainty and those uncertainties will create an uncertainty in the calculated result, in this example, density (Beckwith *et al.*, 1993). In other words, each measured quantity propagates some error in the final result.

Here, we are interested in expressing the experimental uncertainties for the dimensionless parameter of the Rayleigh number. By using Equation 1.1, we can express the combined uncertainty of the Rayleigh number through Equation A.8:

$$u_{Ra}^2 = \left(\frac{\partial Ra}{\partial T_h} u_{T_h}\right)^2 + \left(\frac{\partial Ra}{\partial T_c} u_{T_c}\right)^2 + \left(\frac{\partial Ra}{\partial v} u_v\right)^2 + \left(\frac{\partial Ra}{\partial \alpha} u_\alpha\right)^2 + \left(\frac{\partial Ra}{\partial \beta} u_\beta\right)^2 + \left(\frac{\partial Ra}{\partial H} u_H\right)^2 + \left(\frac{\partial Ra}{\partial g} u_g\right)^2 \quad (4.9)$$

The uncertainties of the properties (α , β and v) can be estimated from tabulated data through the Engineering Equation Solver (Klein, 2012).

The uncertainty from the cavity height H , is expressed in Equation 4.10, where δH is the assembly tolerance. The gravity g , is a physical constant and its uncertainty can be neglected (Equation 4.11).

$$u_H = \pm \delta H = \pm 0.45 \text{ mm} = \pm 0.45 \times 10^{-3} \text{ m} \quad (4.10)$$

$$u_g \cong 0 \quad (4.11)$$

Rewriting Equation 4.9 with the derivatives for each source of uncertainty gives:

$$u_{Ra}^2 = \left(\frac{g\beta H^3}{\nu\alpha} u_{T_h}\right)^2 + \left(-\frac{g\beta H^3}{\nu\alpha} u_{T_c}\right)^2 + \left(-\frac{g\beta\Delta TH^3}{\nu^2\alpha} u_\nu\right)^2 + \left(-\frac{g\beta\Delta TH^3}{\nu\alpha^2} u_\alpha\right)^2 + \left(\frac{g\Delta TH^3}{\nu\alpha} u_\beta\right)^2 + \left(3\frac{g\beta\Delta TH^2}{\nu\alpha} u_H\right)^2 \quad (4.12)$$

Dividing Equation 4.12 by Ra_H^2 , we obtain Equation 4.13 as follows:

$$\left(\frac{u_{RaH}}{Ra_H}\right)^2 = \left(\frac{1}{\Delta T} u_{T_h}\right)^2 + \left(\frac{1}{\Delta T} u_{T_c}\right)^2 + \left(-\frac{1}{\nu} u_\nu\right)^2 + \left(-\frac{1}{\alpha} u_\alpha\right)^2 + \left(\frac{1}{\beta} u_\beta\right)^2 + \left(3\frac{u_H}{H}\right)^2 \quad (4.13)$$

The values of the stated uncertainties are shown in Table 4.3. The uncertainties of the measured temperatures of the hot and cold walls are the uncertainties obtained from the thermocouple calibration process.

Table 4.3- Standard uncertainties of the experimental quantities.

Uncertainty Source	Value [unity]
u_α	8.950E-11 [m ² /s]
u_β	1.993E-6 [1/K]
u_ν	4.336E-9 [m ² /s]
u_H	0.450E-3 [m]
u_g	0 [m/s ²]
$u_{T_h} = u_{T_c}$	0.073 [°C]

From Equation 4.13, the standard uncertainty of the Rayleigh number is $u_{Ra} = 1.48 \times 10^8$, where the expanded uncertainty from Equation A.10 in Appendix A, can be rewritten as:

$$U_{Ra} = k_p u_{Ra} \quad (4.14)$$

For a confidence level of 95.45%, $k_p = 2$ (see Table in Appendix A), and the expanded uncertainty of the Rayleigh number is $U_{Ra} = 2.96 \times 10^8$, which represents 2.6% of the experimental Rayleigh number.

The evaluation of uncertainty associated with measurements of velocity is not within the scope of the performed activities. Nevertheless, it is worth noting that typical velocity error is less than 0.5% of the measured value, as documented by TSI (2008). In Appendix B, one can find a description of the methodology required to evaluate the uncertainty of the measured velocity.

4.2.3 Experimental Repeatability

Experimental repeatability of two consecutive experiments was performed by repeating the setup procedure of the cavity, i.e., filling the cavity with water, seeding with particles, correcting the cavity inclination, and setting up the origin of the laser. The results can be seen in Attachment B. The maximum deviation between the acquisitions obtained during the experiments performed at different times was 0.2 mm/s. This test was performed at $Y = 0.5$ and $Z = 0.5$.

5. RESULTS

In this chapter, the experimental data is presented and analyzed. The initial part comprises the velocity distribution and the second part, the analysis of the influence of the walls on the flow. In the final part, an analysis of turbulence within the cavity is shown.

5.1 VELOCITY DISTRIBUTION

Measurements of the mean vertical and horizontal velocity components at different heights and $Z = 0.5$ are shown in Figure 5.1 (a and b), respectively. In order to avoid the overlap of the data, constants were added in such figures. The parameter V_o is the buoyancy velocity, defined as $V_o = \sqrt{g\beta W(T_h - T_c)}$, and is used as a normalization parameter for the velocity and turbulence intensity results. In the present flow situation, $V_o = 0.04851$ m/s, and W is the distance from the heated walls. The mean velocity components (\bar{u} , \bar{v}) were calculated using Equation 5.1:

$$\bar{m} = \frac{1}{N} \sum_{i=1}^N m_i \quad (5.1)$$

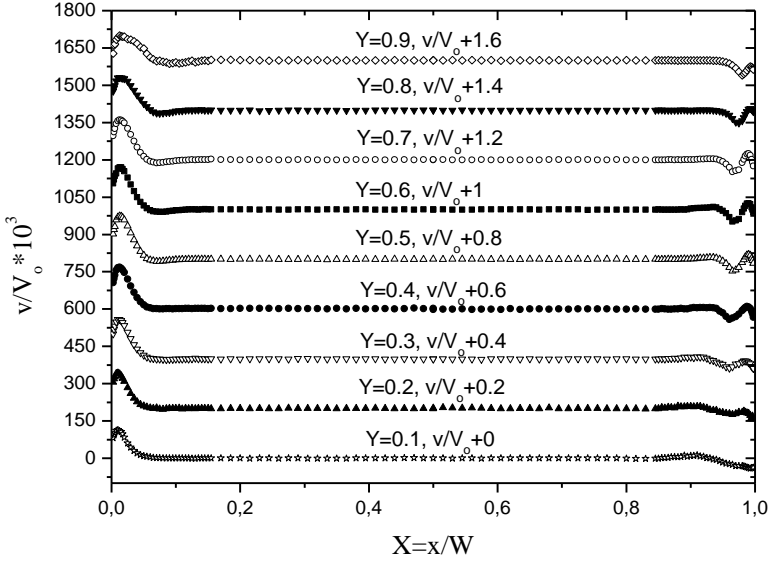
where m is any velocity component, N is the number of readings taken in the experiments and m_i is the i -th velocity measurement.

The flow boundary layer can be seen clearly in the vertical component of the velocity distribution (see Figure 5.1 (a)). The boundary layer of the hot wall starts at the bottom and its thickness increases as it reaches the upper region of the cavity. In contrast, the vertical boundary layer of the cold wall starts at the top with a thinner thickness, which increases as it reaches the bottom region. The components of the velocity are shown in Figures 5.2–5.10. The maximum vertical velocity reaches its value of 8.43 mm/s at cavity mid-height ($Y = 0.5$, where $Y = y/H$) at $X = 0.025$. The maximum horizontal velocity reaches its value of 0.36 mm/s at $X = 0.0125$ and $Y = 0.6$.

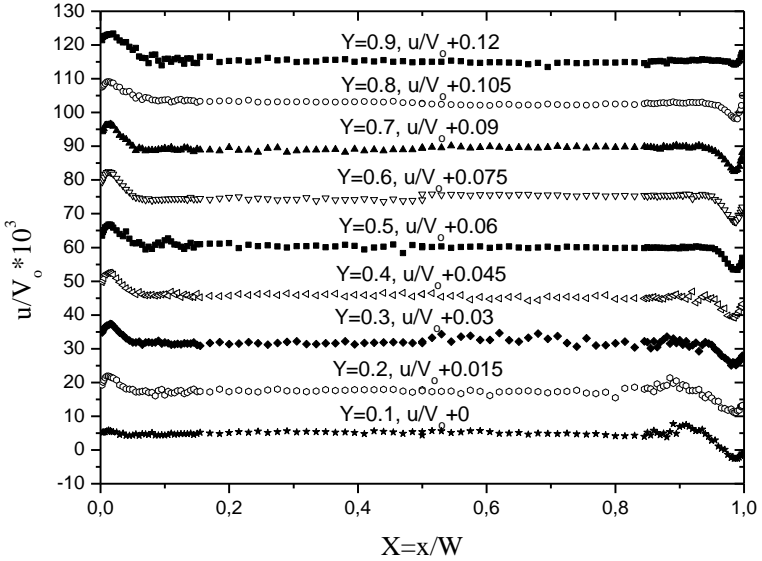
The flow can be divided into two distinct regions: (i) the near-wall region where the velocity gradients are high; (ii) the core region where the flow is approximately stationary. Higher velocities are obtained near the hot wall region, and the peak velocities of the hot side are three times greater than the velocities of the cold side. Analyzing the vertical velocity profiles of the hot wall side shows that outside the

boundary layers there are small negative velocities at $Y = 0.5\text{--}0.9$, suggesting a clockwise recirculating motion. An unexpected result is obtained in the region of the cold wall. Initially, there is a thin film of water of the order of 1–1.5 mm descending on the cold wall. The flow has a tendency to turn its direction upwards after this thin film, and within this region the flow reaches a positive vertical velocity in the top-cold region at $Y = 0.4\text{--}0.8$. Beyond the boundary layer on the cold wall, the fluid is moving upwards, reaching positive velocities throughout most of the cavity height, except at $Y = 0.9$. In this work, this phenomenon will be referenced as the intrusion traveling upwards, a nomenclature also adopted by Hsieh and Yang (1996). The horizontal components of velocity are approximately anti-symmetrical at $Y = 0.6$. The dispersion of the horizontal component of velocity is high at $Y = 0.1\text{--}0.4$ and $Y = 0.9$.

The entire fluid flow vector plot in the cavity is given in Figure 5.11 (a). This plot is based on all the experimental velocity data obtained through LDV, but the vectors magnitudes are amplified for clarity. The flow structure within the cavity can be analyzed and differences can be noticed in the vicinity of the two vertical walls. Analyzing the hot side of the vector plot (Figure 5.11 (a)), the circulatory clockwise motion is confirmed in the upper part of the cavity, $Y > 0.5$. In Figure 5.11 (b), a zoomed view of the flow structure is shown for the cold side region. It seems that an intrusion upwards induces the fluid to change its direction.



(a)



(b)

Figure 5.1- Mean velocity distribution at different heights: (a) vertical velocity; (b) horizontal velocity.

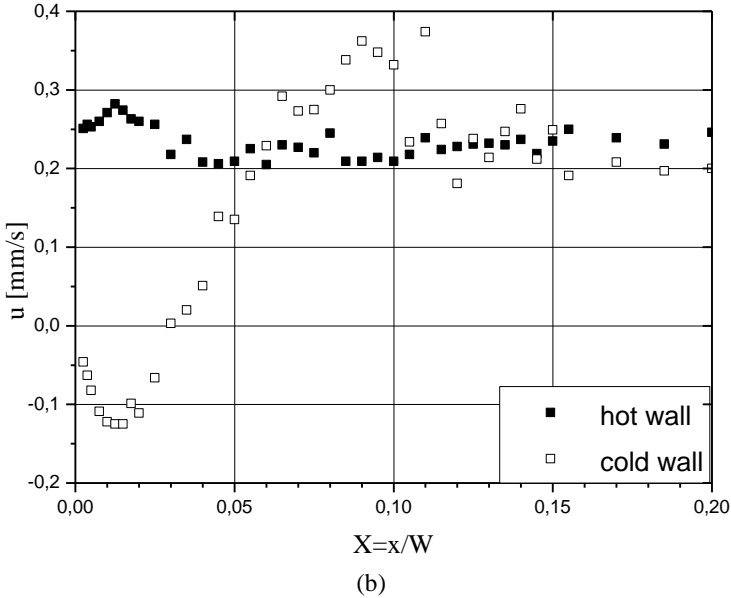
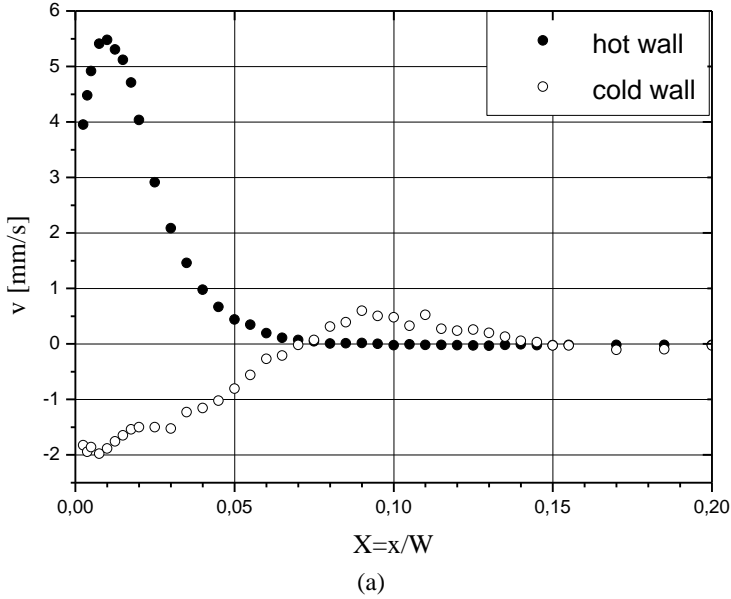


Figure 5.2- Mean velocity distribution at $Y = 0.1$: (a) vertical velocity; (b) horizontal velocity.

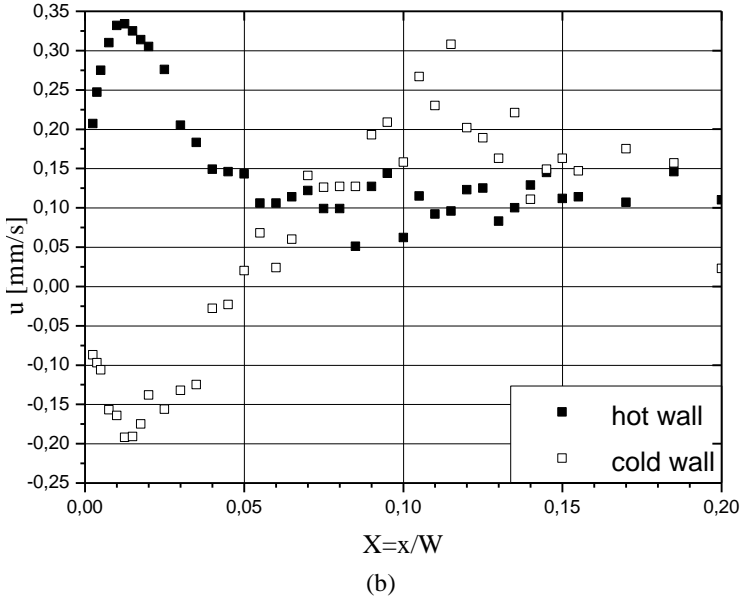
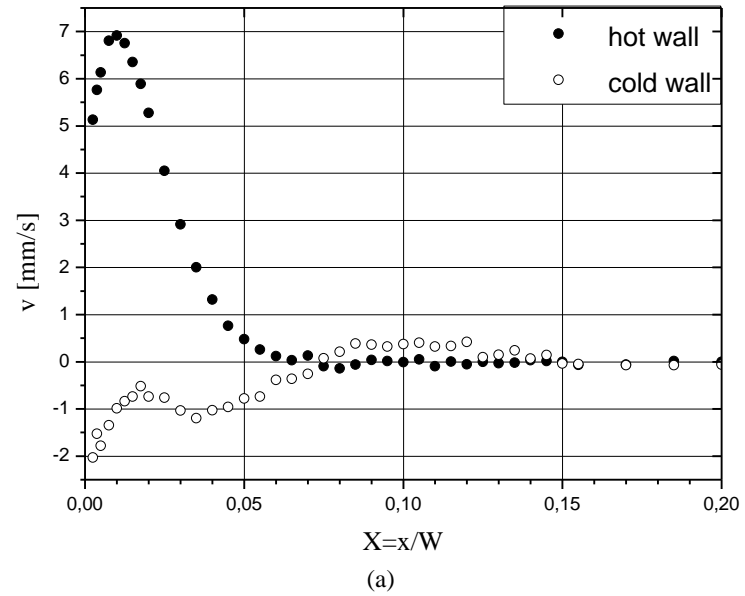


Figure 5.3- Mean velocity distribution at $Y = 0.2$: (a) vertical velocity; (b) horizontal velocity.

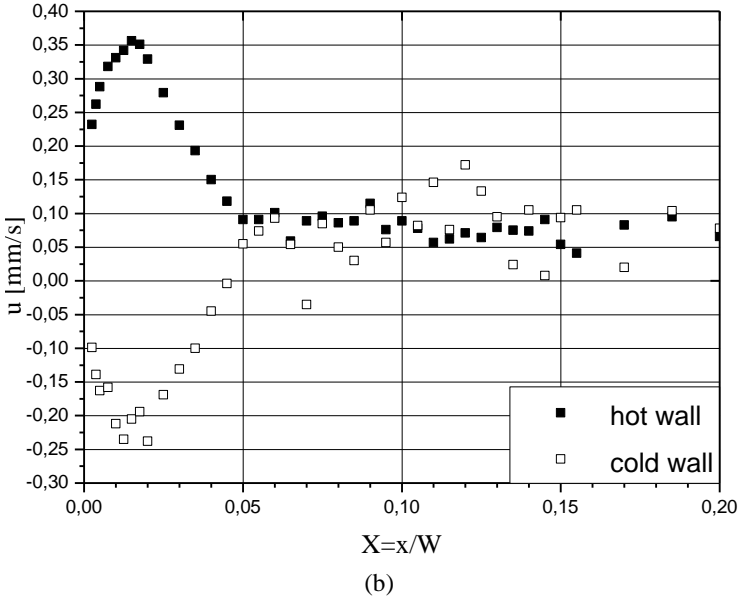
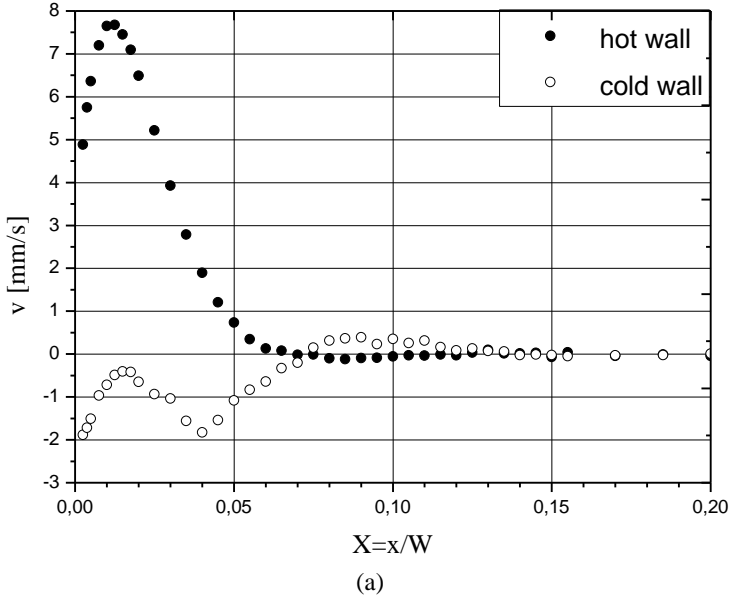


Figure 5.4- Mean velocity distribution at $Y = 0.3$: (a) vertical velocity; (b) horizontal velocity.

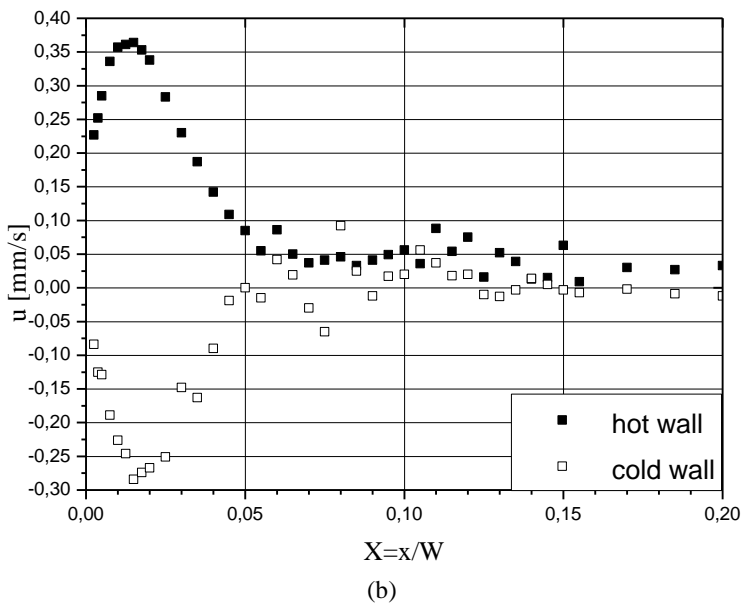
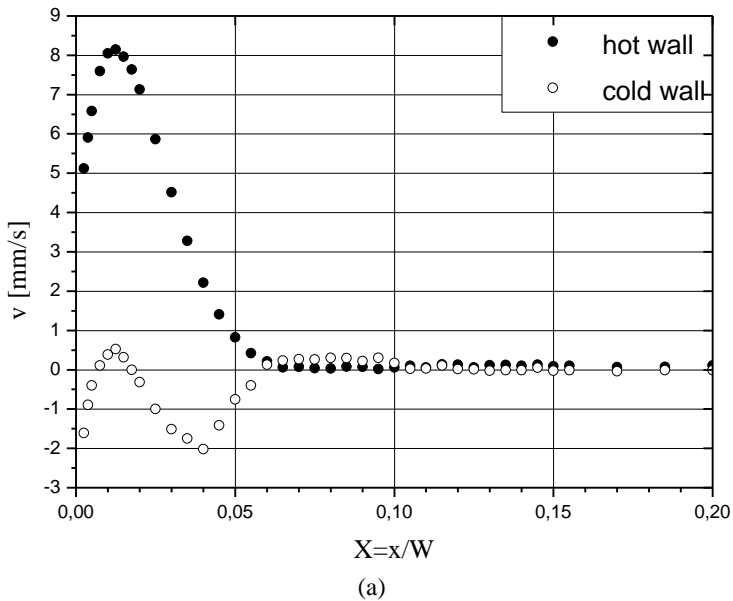


Figure 5.5- Mean velocity distribution at $Y = 0.4$: (a) vertical velocity; (b) horizontal velocity.

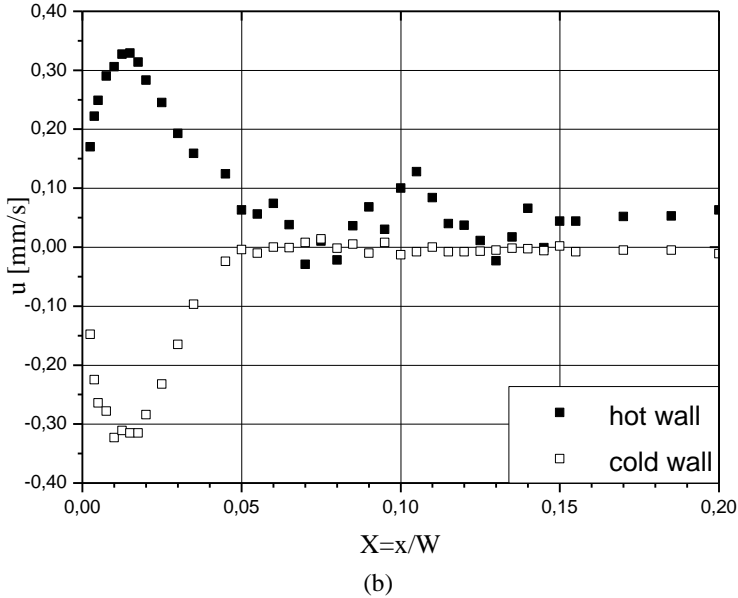
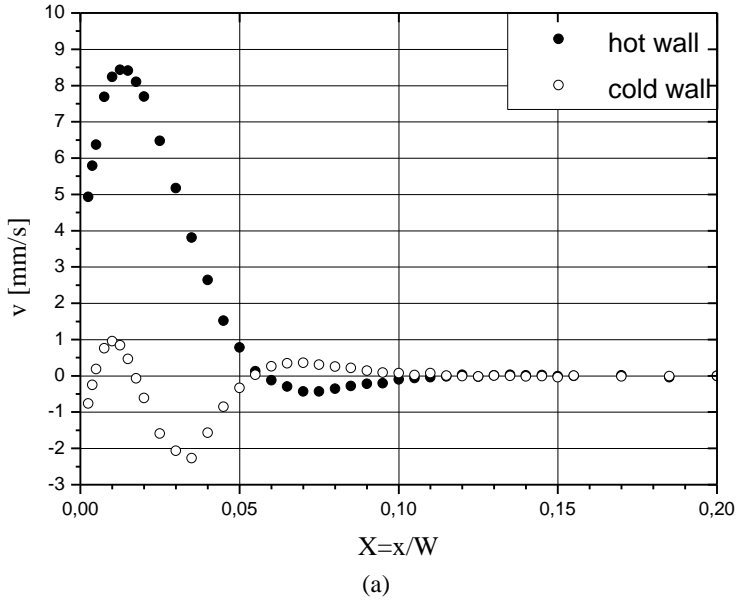


Figure 5.6- Mean velocity distribution at $Y = 0.5$: (a) vertical velocity; (b) horizontal velocity.

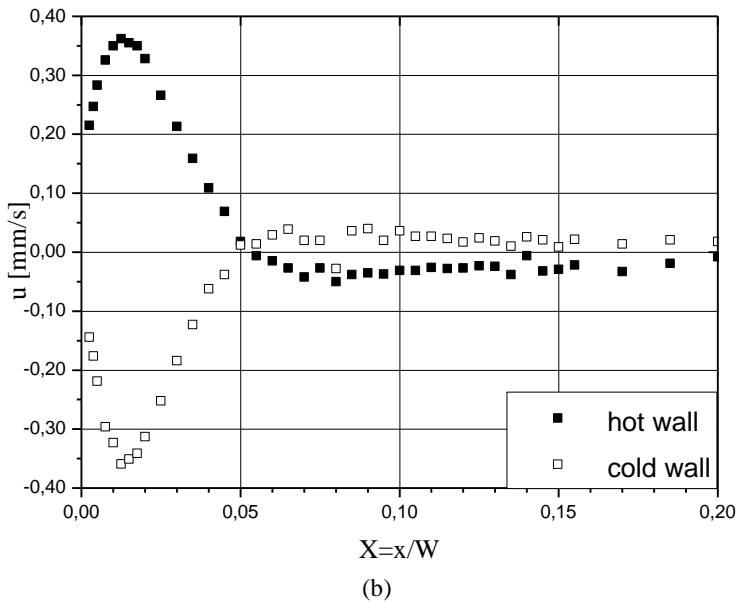
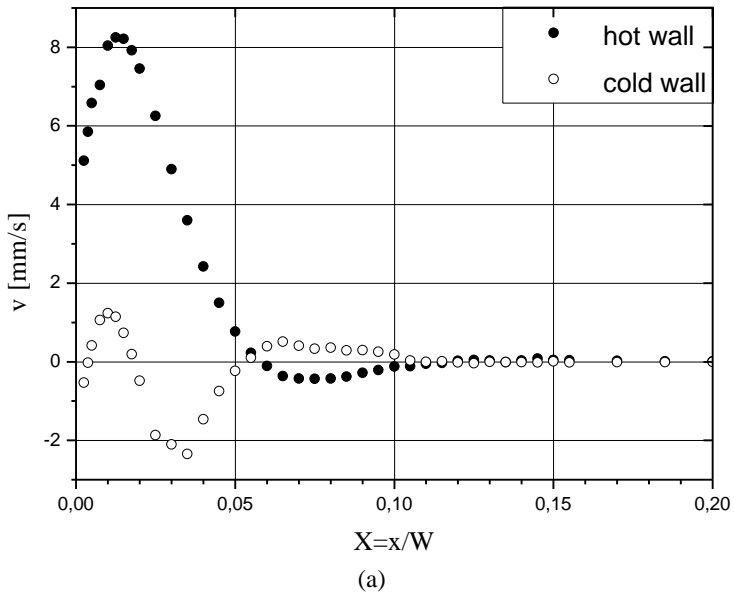


Figure 5.7- Mean velocity distribution at $Y = 0.6$: (a) vertical velocity; (b) horizontal velocity.

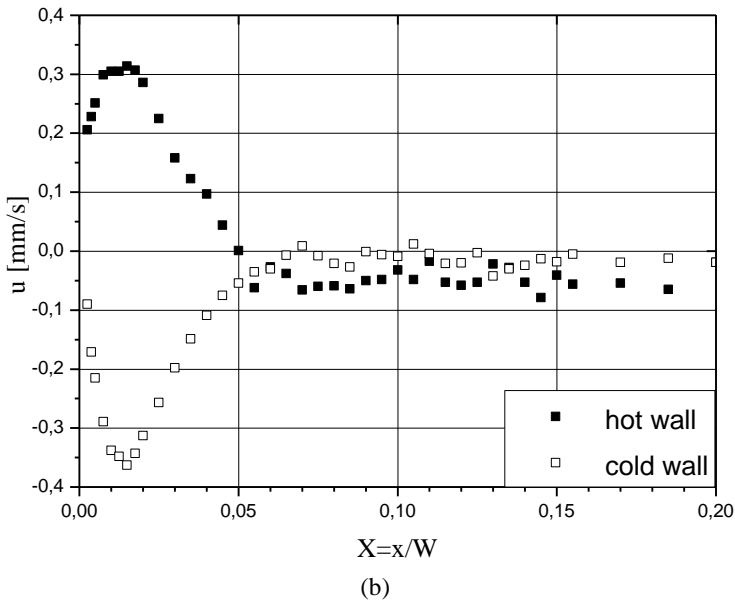
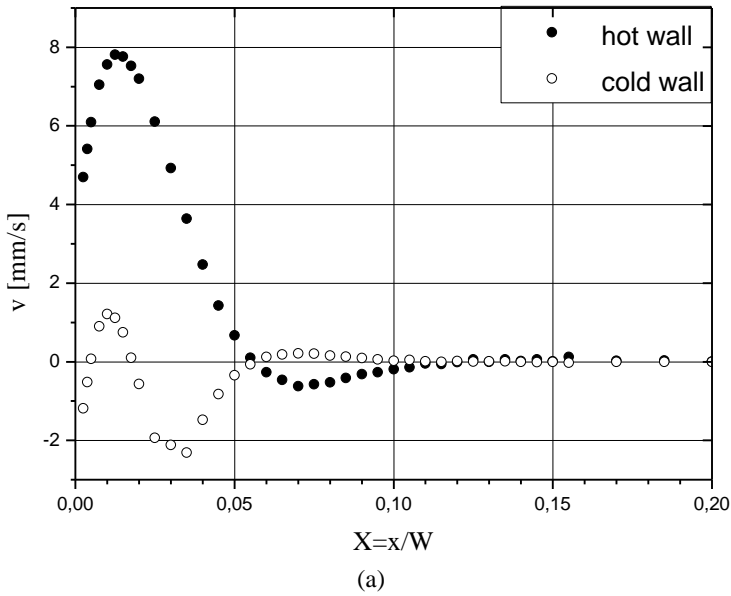


Figure 5.8- Mean velocity distribution at $Y = 0.7$: (a) vertical velocity; (b) horizontal velocity.

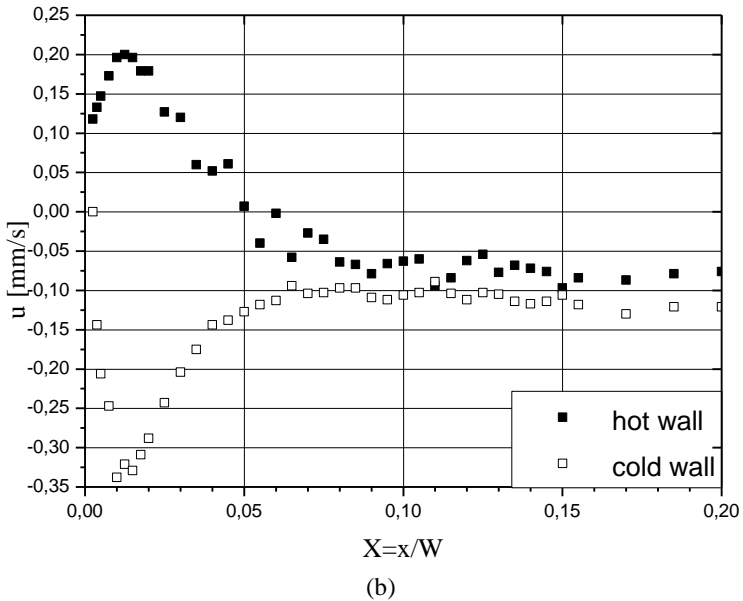
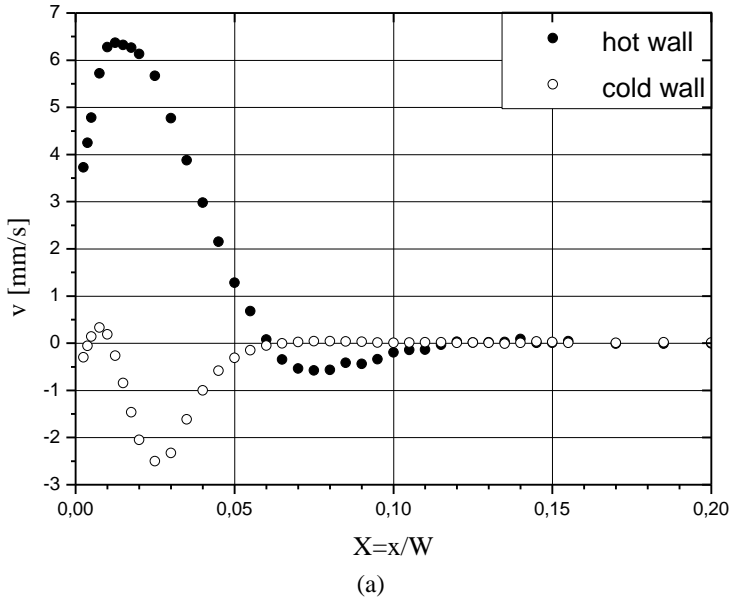


Figure 5.9- Mean velocity distribution at $Y = 0.8$: (a) vertical velocity; (b) horizontal velocity.

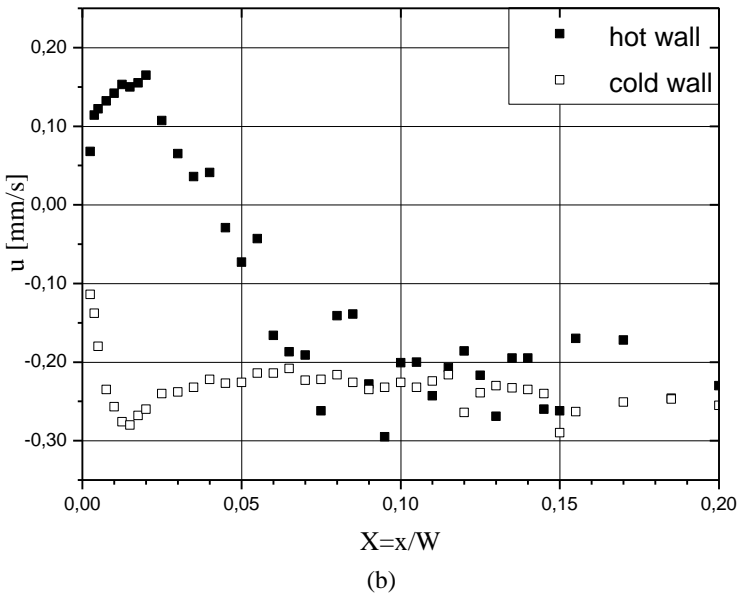
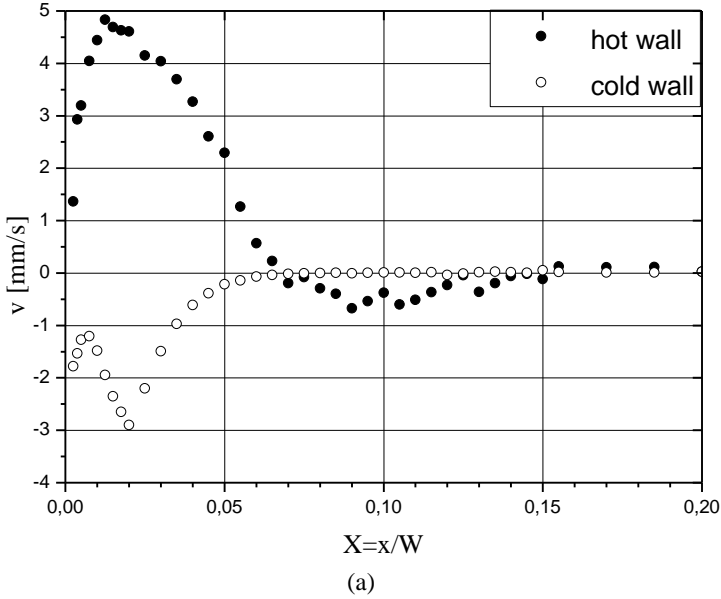


Figure 5.10- Mean velocity distribution at $Y = 0.9$: (a) vertical velocity; (b) horizontal velocity.

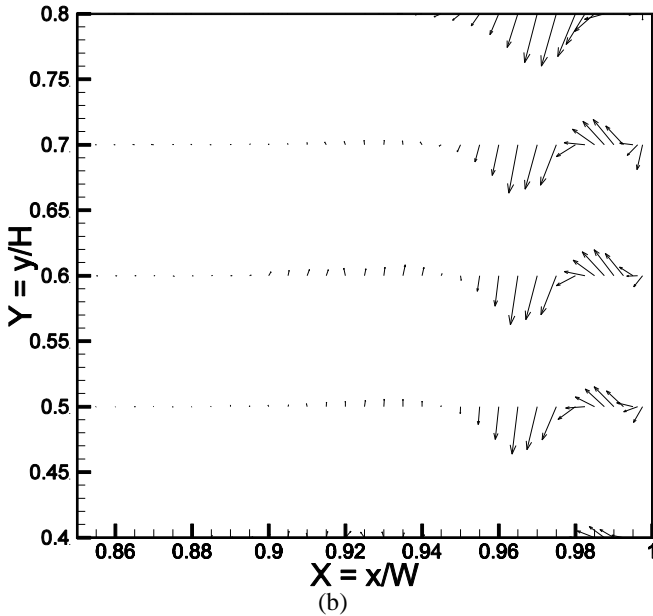
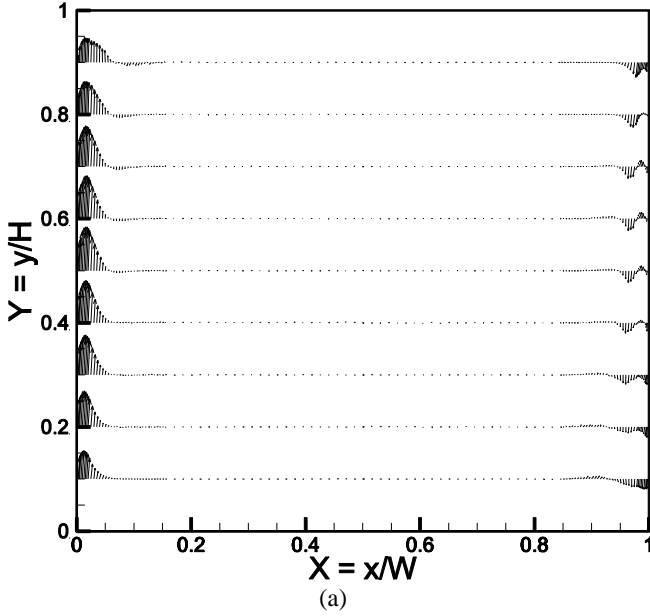


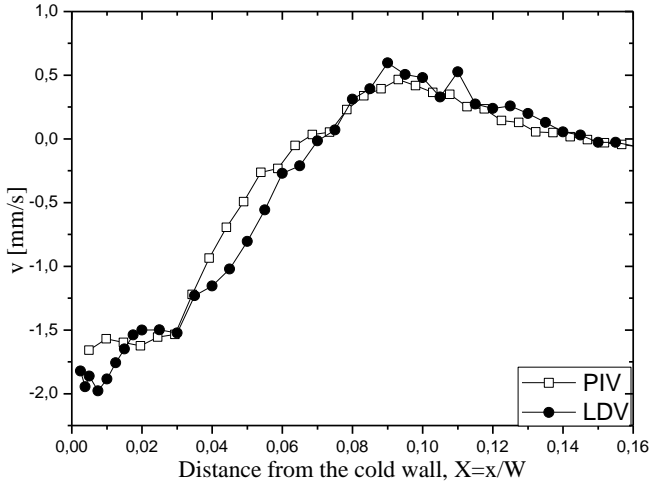
Figure 5.11- Velocity vectors: (a) entire cavity; (b) mid-height region on the cold wall side.

PIV measurements were adopted to further clarify the flow inside the cavity. In order to validate the PIV measurements, a comparison was performed with the LDV results, and the vertical velocity components for two different heights were plotted for the cold wall side at $Y = 0.1$ and $Y = 0.2$, see Figure 5.12 (a and b), respectively. The present results show that there is reasonable agreement for both techniques considering that these results were found in a very small region. On the other hand, near the wall where the velocities are higher, there is a pronounced difference. This can be explained by the chosen time pulses, which were not small enough to perform a good correlation in this region of the flow.

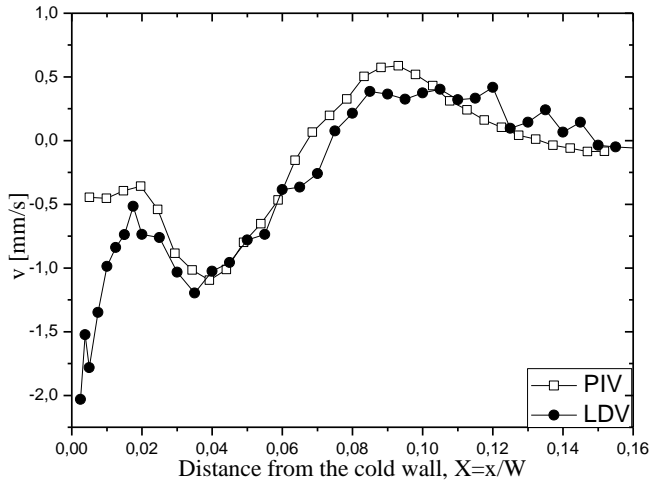
A comparison of the instantaneous and mean flow fields on the cold wall side is given in Figure 5.13. The mean flow field is the average of 151 instantaneous vector maps (see Figure 5.13 (a)). The instantaneous flow reveals the presence of a vortical structure rotating in the clockwise direction (see Figure 5.13 (b)). However, this structure disappears when the averaging is performed and thus, this is an issue of flow unsteadiness. Figure 5.13 (a), shows the fluid moving downwards in the vicinity of the cold wall and then turning its direction; this fluid motion represents the intrusion traveling upwards. The upwards intrusion is located approximately 6 mm from the wall and its influence can be seen clearly in the counter-flow on the cold wall side. It seems that the interaction between the fluid moving downwards and the intrusion moving upwards generates vortices, which can be seen in Figure 5.13 (b), where the vortex core is located approximately 6 mm from the cold wall.

Figure 5.14 shows the hot wall side in a region near the top. The average field shows that the fluid moving upwards has split at the upper corner of the hot wall into two distinct streams: one, the hottest moves along the top wall, and the other moves downwards, forcing the clockwise cell back towards the hot wall (see the instantaneous field, Figure 5.14 (b)).

In order to better analyze the unsteady behavior near the walls, streamlines for three different instants of time were plotted. Figure 5.15 shows the cold wall side, where a vortex is moving downwards. Figure 5.16 shows a vortex moving upwards on the hot wall side. It is believed that the vortex moves downwards on the cold wall side because the fluid layer in the vicinity of the wall has a higher velocity than the intrusion traveling upwards. On the other hand, the fluid layer in the vicinity of the hot wall moves faster than the counter flow, which induces the vortex to displace upwards and rotate in a clockwise direction.



(a)



(b)

Figure 5.12- Validation of the employed experimental techniques (PIV and LDV). Vertical velocity component in the cold wall side at $Z = 0.5$: (a) $Y = 0.1$; (b) $Y = 0.2$.

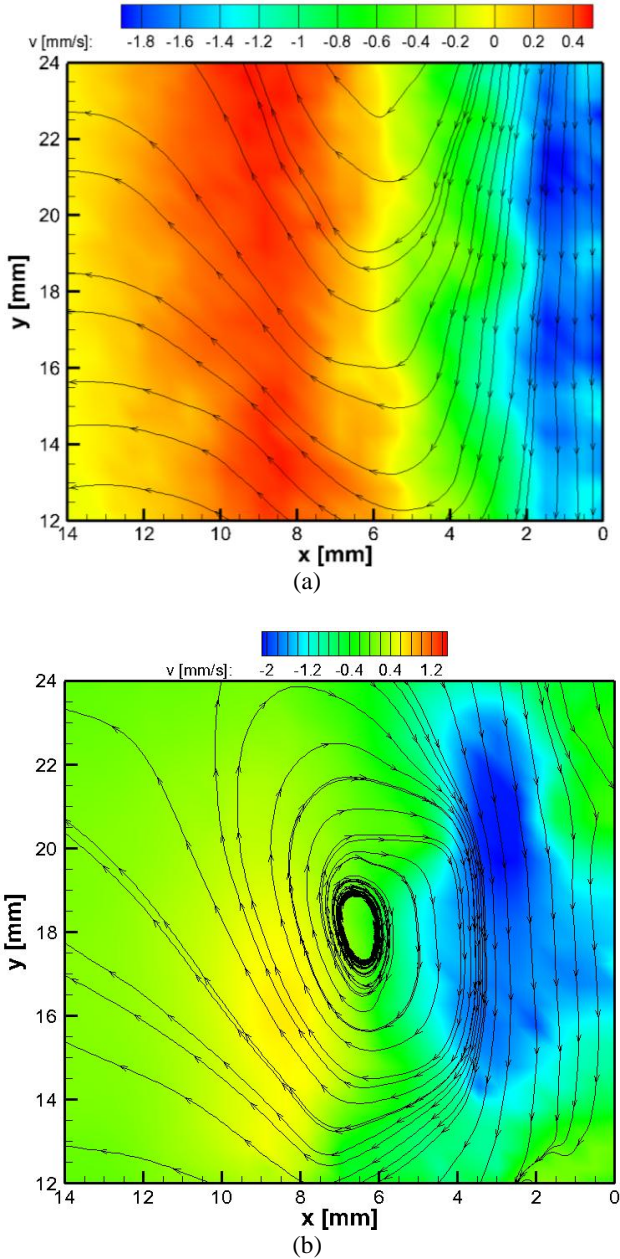


Figure 5.13- (a) Mean velocity and (b) Instantaneous fields for PIV on the cold wall side. x is the distance from the cold wall; y is the distance from the bottom.

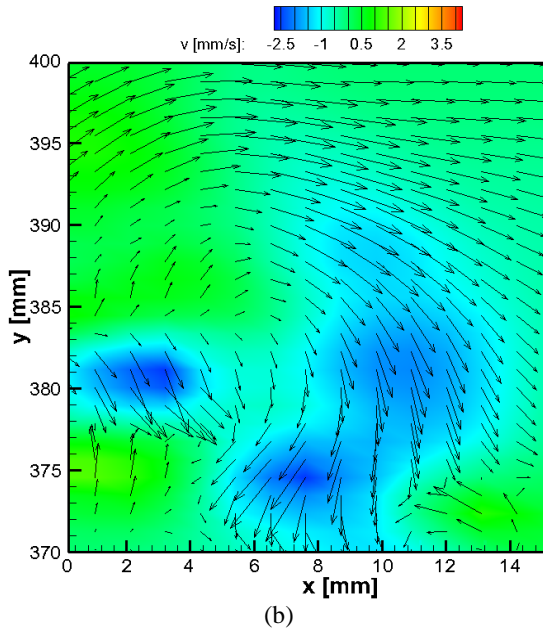
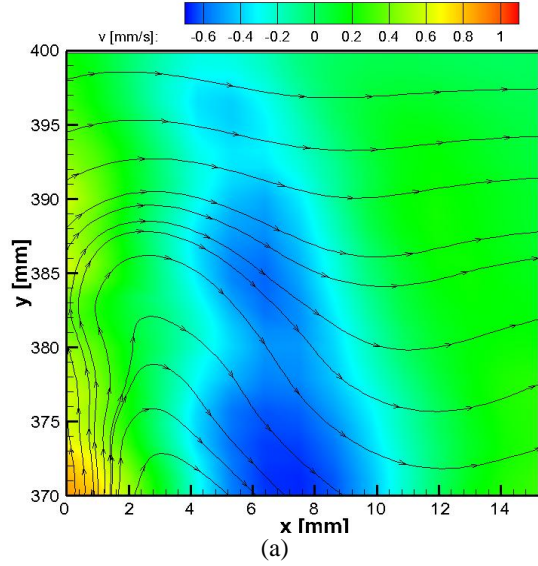


Figure 5.14- (a) Mean velocity and (b) Instantaneous fields for PIV on the hot wall side. x is the distance from the hot wall; y is the distance from the bottom.

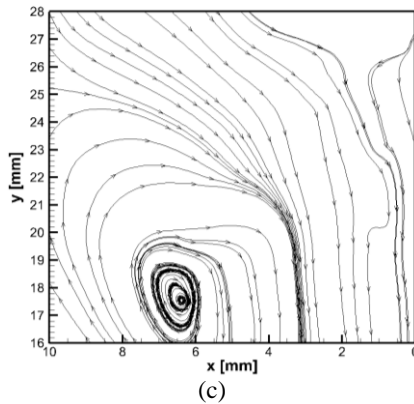
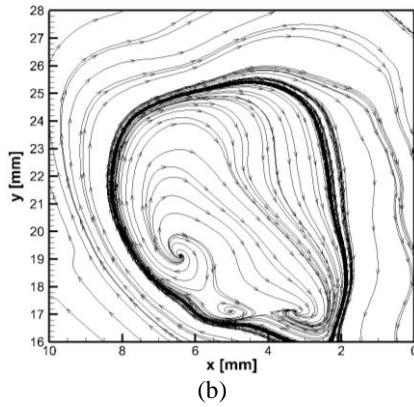
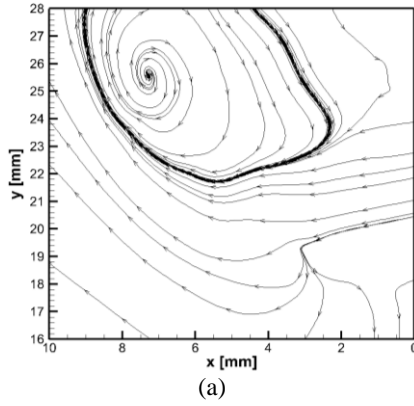
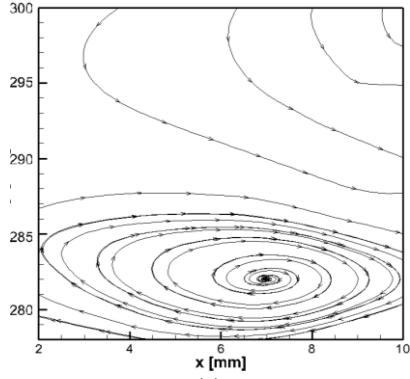
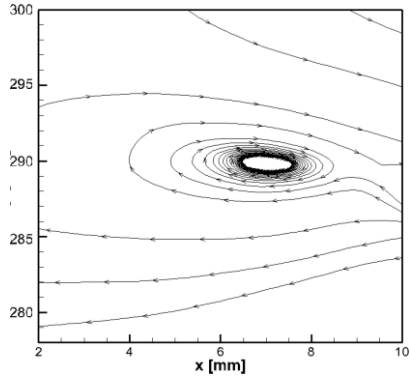


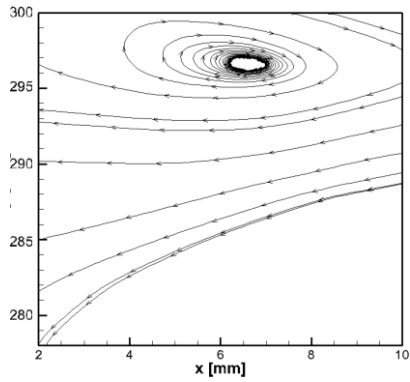
Figure 5.15- Instantaneous velocity field for different time frames on the cold wall side: (a) $t = 0$ s, (b) $t = 1.4$ s, (c) $t = 2.8$ s.



(a)



(b)



(c)

Figure 5.16- Instantaneous velocity field for different time frames on the hot wall side: (a) $t = 0$ s, (b) $t = 1$ s, (c) $t = 2$ s.

5.2 INFLUENCE OF THE WALLS

The three-dimensionality of the flow was observed by measuring the vertical velocity profiles at two different cavity depths, $Z = 0.5$ and $Z = 0.95$ ($Z = z/D$), the latter was located 5 mm from the front acrylic wall (experimentally insulated wall). The presence of the adiabatic walls does not seem to greatly affect the vertical component of velocity at this point in the hot wall region (see Figure 5.17); the cold wall region seems to be more influenced. However, at this point, in the mid-depth of the cavity, the flow can be considered as two-dimensional.

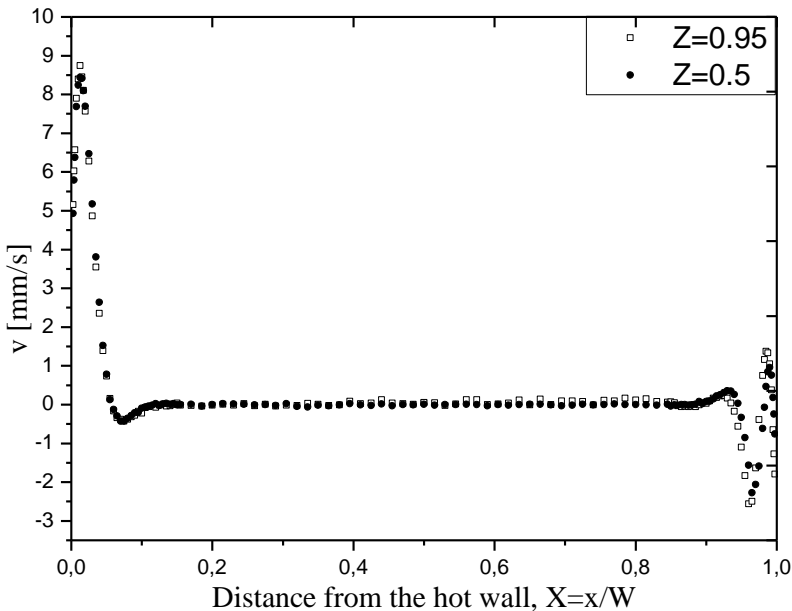
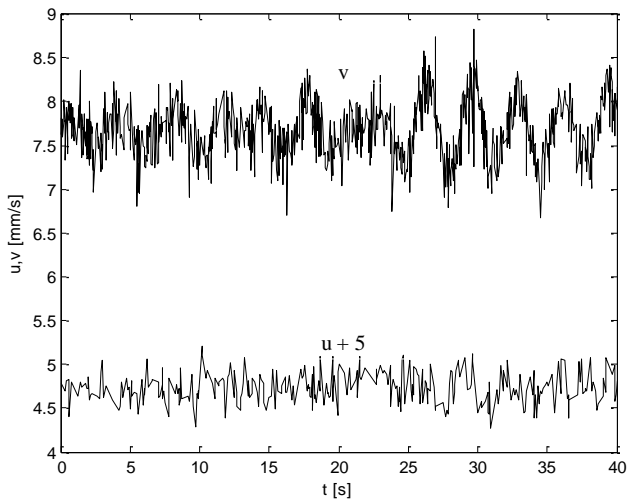


Figure 5.17- Comparison of the vertical velocity at cavity mid-height $Y = 0.5$ and $Z = 0.5$ and 0.95 .

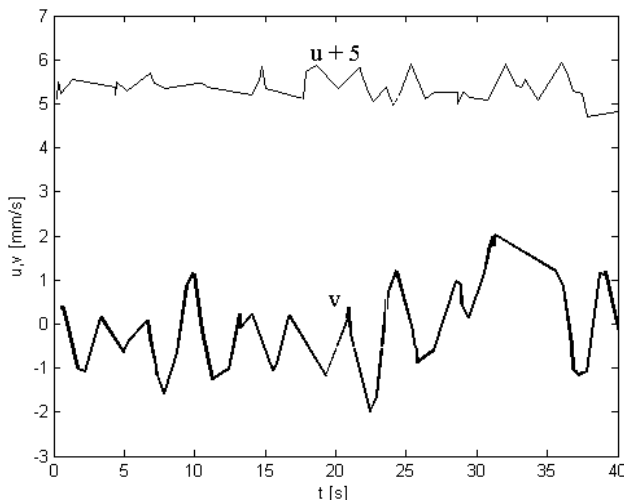
5.3 TURBULENCE ANALYSIS

Figure 5.18 (a and b) shows the time history of the velocity components, vertical (v) and horizontal (u), on the hot and cold wall sides, respectively. These recorded data were measured simultaneously at the cavity mid-height. The highest data rate was 23 Hz on the hot wall side, near the peak velocity region, and the lowest was 1 Hz in the core

region. The difference between the data rates is very clear in this figure, where the data rate on the cold wall side is approximately 1.3 Hz.



(a)



(b)

Figure 5.18- Velocity signals near the cavity walls at $Y = 0.5$: (a) hot wall; (b) cold wall.

The root-mean-square of the fluctuation quantities (u'_{rms} , v'_{rms}) were calculated through Equation 5.2 as follows:

$$m'_{rms} = \left[\frac{1}{N} \sum_{i=1}^N (m_i - \bar{m})^2 \right]^{1/2} \tag{5.2}$$

where \bar{m} is the mean quantity (\bar{u} , \bar{v}), obtained through Equation 5.1, and m_i is the i -th velocity measurement.

The vertical and horizontal components of the velocity fluctuations at different heights are shown in Figure 5.19 and Figure 5.20, respectively. The latter figure, shows that the velocity fluctuations are concentrated in the boundary layer region, i.e., the top-left and bottom-right regions. The overshoot of the profiles is obvious at $Y = 0.3-0.4$, 0.6 and $Y = 0.9$.

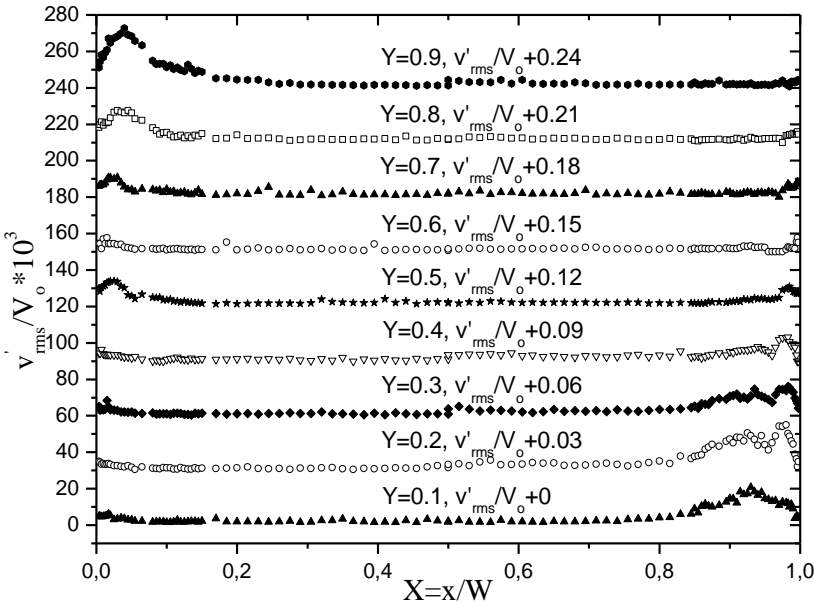


Figure 5.19- Vertical velocity fluctuation at different heights.

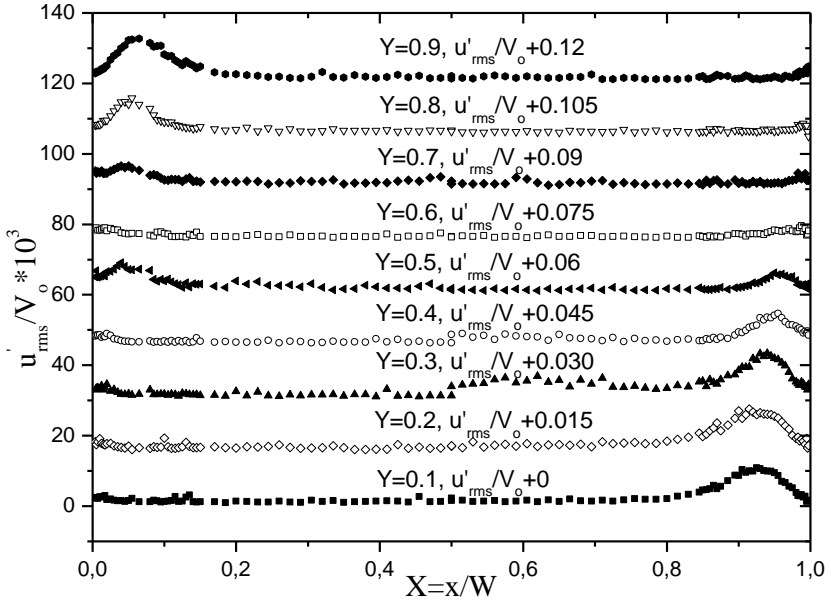


Figure 5.20- Horizontal velocity fluctuation at different heights.

By definition, isotropic turbulence means that the flow statistics are invariant under rotations and reflections in space. In turbulence modeling, the hypothesis of isotropy is very important and is largely employed, especially by the RANS models. For natural convection in cavities, the flow is theoretically anisotropic because solid walls bound the flow. In order to study this, the fluctuating components of the velocities near the hot and cold walls are shown in Figure 5.21. On the hot wall side, the anisotropic region starts from the wall and continues up to $X \approx 0.05$, the point of the strongest anisotropy is $X \approx 0.018$ ($v'_{rms}/u'_{rms} \approx 2.5$). On the cold wall side, the strongest point is approximately $X \approx 0.98$ ($v'_{rms}/u'_{rms} \approx 4$). Beyond these points, the anisotropy decreases towards the core region of the cavity where the fluid is approximately stationary.

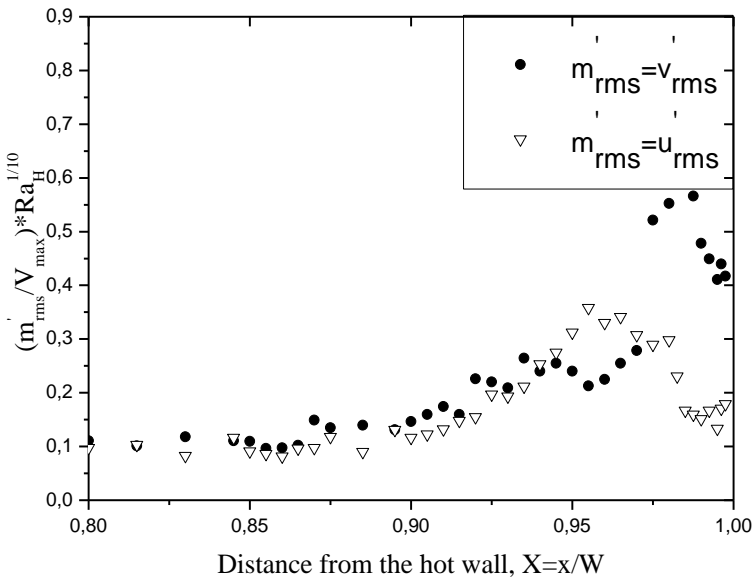
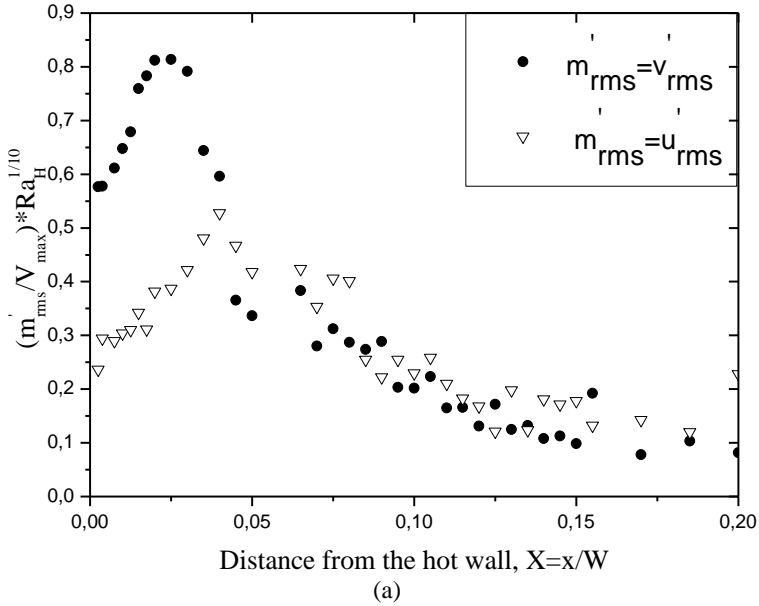


Figure 5.21- Relation between fluctuation quantities near the walls at $Y = 0.5$;
 (a) hot wall side; (b) cold wall side.

The cross correlation of the velocity fluctuations u' and v' gives the Reynolds shear stress $\overline{u'v'}$, which can be estimated by using Equation 5.3 (Albrecht *et al.*, 2003). This term physically represents the average of the momentum flux due to the effect of turbulence.

$$\overline{u'v'} = \frac{\sum_{i=1}^N (u_i - \bar{u})(v_i - \bar{v})g_i}{\sum_{i=1}^N g_i} \quad (5.3)$$

In this equation, g_i is the weight factor, which is inversely proportional to the vector velocity magnitude. Equation 4.3 assumes that the velocities (u and v) are measured at the same instant in time. When the data acquisition is performed in independent time series, Equation 5.3 must be modified in order to account for non-time-coincident data collection, and this modification gives Equation 5.4:

$$\overline{u'v'} = \frac{\sum_{i=1}^N \sum_{j=1}^M (u_i - \bar{u})(v_j - \bar{v})g_{ui}g_{vj}}{\sum_{i=1}^N g_{ui}g_{vi}} \quad (5.4)$$

In the literature, there are many studies to obtain an estimator of the weight factor, because not all the LDV systems provide the measurement quantities necessary to obtain the weight factor, and also because LDV data have two important peculiarities. The first is that the samples are irregularly spaced in time, and the second is that the short-term mean sampling rate is usually strongly correlated to the velocity. The latter property is the cause of biased estimators. The estimators most usually employed are:

- Free-running processor

$$g_i = 1 \quad (5.5)$$

When using this estimator, one obtains the exact arithmetic mean of all samples, although not recommended for use because it represents an upper bound value.

- Arrival time

$$g_i = t_i - t_{i-1} \quad (5.6)$$

This estimator is limited to high data densities, and the only one recommended for non-homogeneously seeded flows. For this work, the arrival time was employed (Equation 5.6), and the distribution of the Reynolds-stress at different heights can be seen in Figure 5.22. The Reynolds-stress is significant only in the downstream part of the vertical boundary layers, indicating that there is transition from laminar to a turbulent regime along the active walls, where the boundary layers develop.

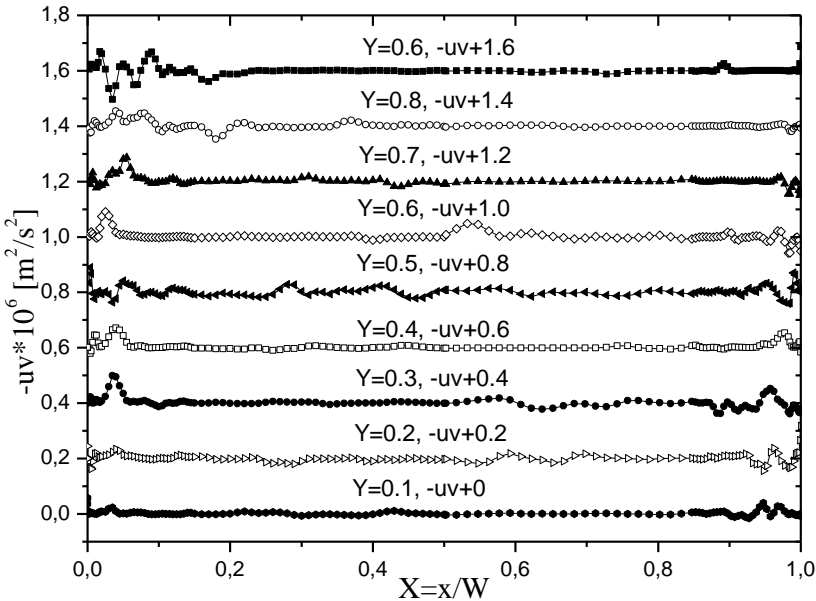


Figure 5.22- Distribution of Reynolds-stress at different heights.

In the past, most studies of natural convection in cavities have been performed through the 2D assumption, which implies that the length in the third direction (depth) is sufficiently large such that its influence can be neglected. This assumption is mainly adopted by numerical solutions; however, this is not easily achieved in practical experiments. Penot and N'Dame (1992) pointed out that the two-dimensional approximation of experimental natural convection in cavities should have an aspect ratio in the third direction (AR_h = depth/width) greater than 1.8.

Even though the cavity in the present work has an aspect ratio equal to 1 in the third direction, the presence of the adiabatic walls

seems not to affect the flow, as can be seen in Figure 5.17; therefore, the flow can be assumed to be two-dimensional. This assumption is valid only at the mid-depth of the cavity and for this class of flow.

It is very difficult to estimate the velocity fluctuation in the depth direction (w') without direct measurements. Experimental and numerical evidence by Kreplin *et al.* (1979) and Spalart (1988) suggest that along an isothermal vertical wall:

$$u'^2 \leq w'^2 \leq v'^2 \quad (5.7)$$

As a first estimation, Equation 5.8 can be used to calculate w' :

$$w'^2 = \frac{u'^2 + v'^2}{2} \quad (5.8)$$

The turbulent kinetic energy is defined through Equation 5.9:

$$k = \frac{1}{2}(u'^2 + v'^2 + w'^2) \quad (5.9)$$

Hence, by combining Equations 5.8 and 5.9, the turbulent kinetic energy k , can be estimated as:

$$k = \frac{1.5(u'^2 + v'^2)}{2} \quad (5.10)$$

By using Equation 5.10, an analysis of the turbulent kinetic energy has been performed along the cavity height of the hot and cold walls for the three distances from the wall: $x = 1.25, 5.0,$ and 15.0 mm, and for symmetrical points according to cavity center ($x = 0$). The results in Figure 5.23 (a and b) show higher turbulent kinetic energy in the top hot and the cold bottom regions of the cavity, this is in agreement with results of with Figure 5.19 and Figure 5.20, showing that in such regions the boundary layers are thicker. All the observed profiles on the hot wall side presented a local maximum at $Y = 0.5$.

The turbulence intensity I , is related with the turbulent kinetic energy through $I \sim \sqrt{k}$. According to Figure 5.23 (a), above $Y = 0.6$ the turbulence intensity increases, and at $Y = 0.8-0.9$, the turbulence intensity is higher at $x = 5.00$ mm, which is the intermediate position. At $x = 1.25$ mm, which is very close to the region where peak velocities

occur, there is less turbulent kinetic energy. Finally, at $x = 15$ mm, the energy is much lower, mainly because this point is already at the core region where the fluid is approximately stationary. In Figure 5.23 (b), which is the cold wall, the turbulent kinetic energy is lower at $x = 98.75$ mm, this point is located within the region where the velocity is upward, as discussed earlier.

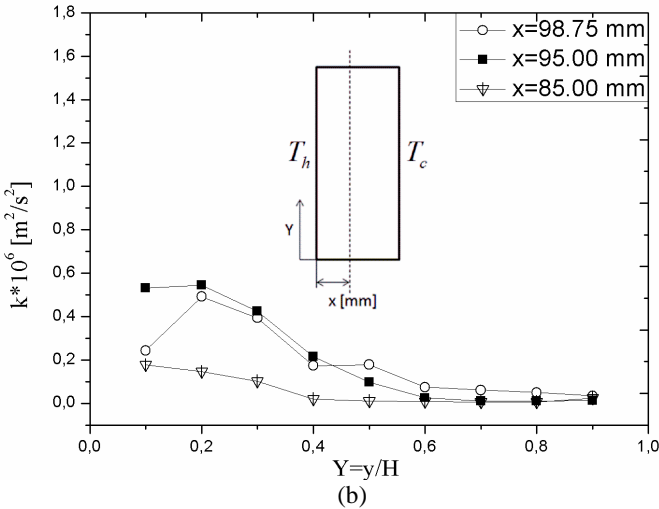
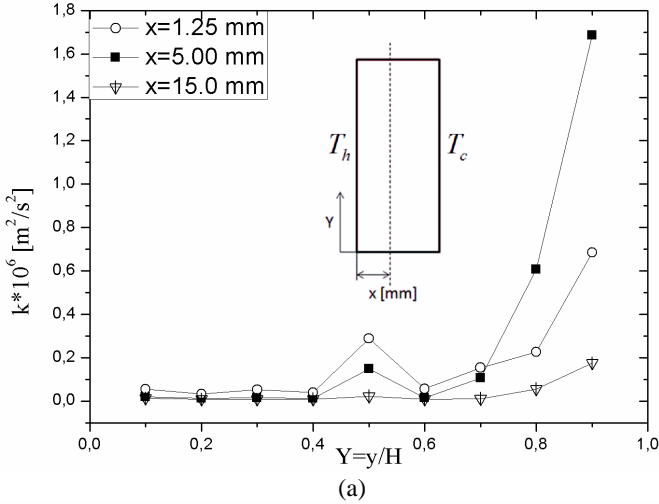


Figure 5.23- Turbulent kinetic energy along the walls: (a) hot wall; (b) cold wall.

Figure 5.24 shows the contours of turbulent intensity I , considering the buoyancy velocity (V_o) as the normalization parameter. Therefore, this is an estimation of the order of magnitude, where $I \equiv \sqrt{2k/3}/V_o$. The hot wall side exhibits the peak turbulence intensity, whereas the cold side seems to have a larger region affected by turbulence. The chosen range of the colors does not allow to clearly identify a small region at $Y = 0.9$ and $X = 0.015\text{--}0.065$ in which the highest turbulent intensity was observed ($I = 1.5\text{--}2.4\%$).

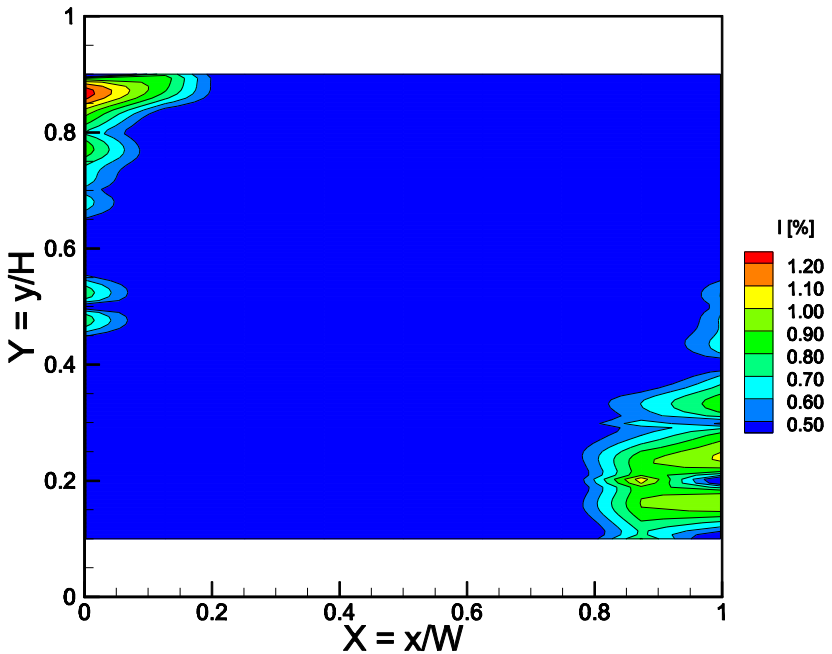


Figure 5.24- Contours of turbulent kinetic energy.

Viscous dissipation is one of the important characteristics of turbulence. In order to sustain turbulent flow, a continuous source of energy supply is required, because kinetic energy is rapidly converted into heat by viscous friction.

Turbulence causes the formation of eddies of different scales. Most of the kinetic energy of the turbulent motion is contained in the large-scale structures. The transfer of energy from these large-scale structures to the small-scale structures is essentially an inviscid mechanism. As this process continues, smaller and smaller structures are

created, which produces a hierarchy of eddies. Eventually, this process creates structures that are small enough for viscous dissipation of energy to take place. Such structures are referred to as Kolmogorov length scales.

The most important parameter influencing the small-scale motion is based on the dissipation rate per unit mass ε [m^2/s^3] and the kinematic viscosity ν [m^2/s]. Given these two parameters, there are unique length, velocity, and time scales that can be formed for the Kolmogorov scales, as shown in Equation 5.11 (Pope, 2000).

$$\eta \equiv \left(\frac{\nu^3}{\varepsilon}\right)^{1/4}, \tau \equiv \left(\frac{\nu}{\varepsilon}\right)^{1/2}, v \equiv (\nu\varepsilon)^{1/4} \quad (5.11)$$

The Kolmogorov length scale η is used to estimate the size of the smallest dissipative eddies, where ε is the dissipation rate of turbulent kinetic energy. The dissipation rate is balanced by energy supplied by the large scales. The amount of kinetic energy per unit mass of the large scales is proportional to u^2 and the rate of transfer of energy is proportional to L/u , where u and L are the velocity and length scales of the large eddies. Hence, the rate of energy supply to the small scales is of order u^3/L .

In the context of one-equation turbulence models based on the eddy viscosity hypothesis, the velocity scale u is usually replaced by $k^{1/2}$ and the dissipation rate is expressed through Equation 5.12:

$$\varepsilon = C_\mu^{3/4} k^{3/2} / L \quad (4.12)$$

where $C_\mu = 0.09$ (Wilcox, 2010). The measurement of the velocity distribution at the mid-height of the cavity was used to estimate the turbulent kinetic energy, which peaked near the hot wall at $4.2 \times 10^{-7} \text{ m}^2/\text{s}^2$. At about the cavity mid-height, the experimental results gave a boundary layer thickness of 6 mm and this value was used for L . Equation 4.12 gives $\varepsilon \approx 7.5 \times 10^{-9} \text{ W/kg}$ and the corresponding values of η , τ , and v are 3.2 mm, 11.2 s, and 0.29 mm/s, respectively.

5.4 DISCUSSION OF RESULTS

At this point, an attempt to explain the main findings in the present work will be developed by relating them with works in the

literature, and through discussion of the results obtained from the performed tests.

5.4.1 Asymmetry of the Flow

The asymmetry of the flow may be caused by the three-dimensional effect due to the variation of properties across the cavity. The smaller viscosity in the vicinity of the hot wall leads to a larger upward velocity than the velocity near the cold wall. The asymmetry was also observed by Hsieh *et al.* (1996) using silicon oil as the working fluid ($Pr = 457$), and $Ra_H = 6.9 \times 10^7 - 4.12 \times 10^8$ in a rectangular cavity.

The velocity in the vicinity of the cold wall is three times lower than the velocity on the hot wall side, and it seems that the fluid that moves downwards with much less momentum has a more intense interaction with the stationary fluid in the core region of the cavity; the larger region affected by the turbulence was observed in Figure 5.11.

The major part of the performed work in this field corresponds to air-filled cavities. For example, works with air as the working fluid have been performed by Soria *et al.* (2004) through DNS, in a cavity with the same geometry as the present work, with $Ra_H = 6.4 \times 10^8$, and the experimental work done by Tian and Karayiannis (2000) using a square cavity (aspect ratio equal 1), for a Rayleigh number $Ra_H = 1.58 \times 10^9$. For these works, the anti-symmetrical feature was observed.

According to Gifford (1991), the anti-symmetrical feature disappears in non-Boussinesq solutions. Gray and Giorgini (1976) pointed out that the use of the Boussinesq approximation in the momentum equations can be considered valid for variations of thermophysical properties up to 10% with respect to the mean value. The working conditions of this master's thesis presented a variation of about 12% in the dynamic viscosity and 22% of the thermal expansion coefficient.

5.4.2 Upward Velocity Near the Cold Wall

The unexpected results obtained for the vertical component of velocity in the region of the cold wall were verified by performing tests for the following aspects:

(a) Measurement repeatability - The measurement of the vertical component of velocity in the region of the cold wall was repeated 3 times;

(b) Geometric imperfection - Changing the side of the cold wall, which was initially at $x = W$, to $x = 0$. This procedure allows the verification of whether there was a specific feature only observed in the wall, which was originally the cold wall.

(c) Velocity measurement bias - A common problem related to LDV measurements is the velocity bias. When applying arithmetic averaging to the velocity signal, the resultant velocity will be biased towards a higher value than the actual flow velocity. One of the most employed techniques used to overcome this, is to reconstruct the velocity signal in such a way that unbiased statistics are obtained (Edwards, 1987). A common way to perform this, is the sample and hold processor (S/H), which averages all the velocity realizations, weighting each one by the time to the next realization. The mean of a sample and hold processor is given by Equation 4.13:

$$\bar{v}_{SH} = \frac{\sum v_i g_i}{\sum g_i} \quad (5.13)$$

where v_i is the measured velocity of the i -th realization and g_i is the weight factor, and it represents the time between the arrival of the i -th and the $i-1$ -th realization, and can be obtained through Equation 4.6.

Winter *et al.* (1991), pointed out that at a sufficiently high ratio of flow time scale/measurement time scale, this will result in bias-free sampling statistics when using Equation 5.13. Therefore, it is very important to guarantee a minimum necessary data rate in order to obtain bias-free results when using a sample and hold processor.

In the retest of the first item (a), the results showed a good repeatability, as already seen earlier. In other words, the flow exhibited the same characteristics, i.e., the tendency of the water going upwards close to the wall. The same behavior was also observed in the second item (b).

In the analysis of item (c), Figure 5.25 shows that there is approximately no difference between the arithmetic mean and the sample and hold processor, which seems to indicate that the velocities are bias-free due to an adequate data rate.

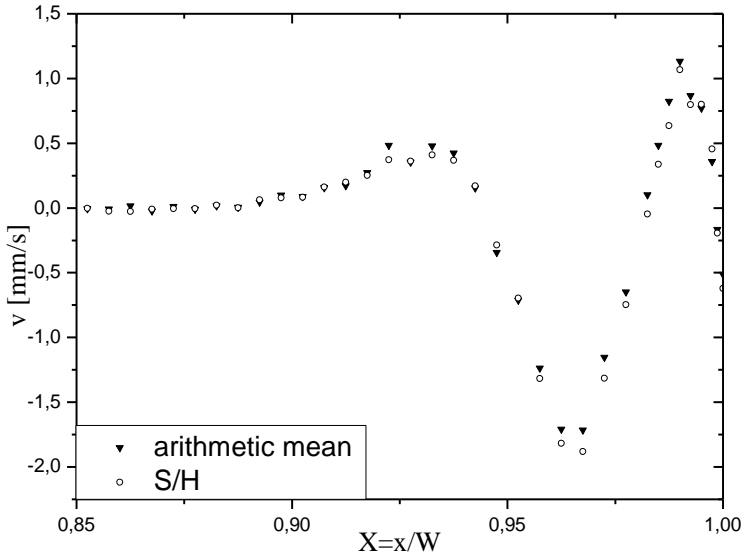


Figure 5.25- Comparison between the arithmetic mean and the sample and hold processor (S/H) in the reconstruction of the vertical velocity signal at $Y = 0.5$ on the cold wall side.

6. CONCLUSIONS

6.1 PRELIMINARY CONSIDERATIONS

An experimental investigation of turbulent natural convection in a water-filled cavity was conducted at $Ra_H = 1.14 \times 10^{10}$. The cavity had a square base and aspect ratio 4 in the height direction with two vertical walls maintained at different temperatures, inducing convective flow within the cavity.

Great effort was spent in designing the cavity, and special attention was devoted to the surface quality of the internal walls, and also to guaranteeing the ideally adiabatic and isothermal walls of the cavity. The temperature fluctuations in the heated walls were less than $0.9\text{ }^\circ\text{C}$ in the hot wall and $0.4\text{ }^\circ\text{C}$ in the cold wall.

In order to ensure that the cavity was not inclined during the measurement process, a support was designed and manufactured allowing control of the inclination in the two horizontal axes. The cavity was attached to this support to guarantee repeatability of the measurement.

The resulting uncertainty of the Ra_H was 2.6% for a confidence level of 95.45%. The repeatability of the experiment seemed to be reasonable, but maintaining the steady state conditions over long periods proved to be very challenging.

6.2 MAIN FINDINGS

To the author's knowledge, this is the first work where the velocity distribution was obtained using a water-filled cavity at a high Rayleigh number.

The flow is limited to a small portion in the near-wall region, and this region represents only 10% of the domain within the heated walls direction. The core region of the cavity is approximately stationary. If compared with an air-filled cavity, the boundary layer is thinner in the same conditions. The peak velocities occur approximately at $Y = 0.5\text{--}0.6$. The turbulence is more intense where the vertical boundary layer is thicker, i.e., in top hot and bottom cold regions.

The three-dimensionality of the flow was analyzed by measuring the velocity profiles at two different cavity depths ($Z = 0.5$ and 0.95), and for the analyzed profiles, the flow seemed not to be greatly affected by the presence of the adiabatic walls. The flow was

approximately two-dimensional for a large proportion of the fluid domain.

The flow presented an asymmetrical feature, where higher velocities were observed on the hot wall side. An unexpected result was measured in the cold wall region, where immediately after a very thin film of descending water on the cold wall, the flow direction turns upwards, reaching positive vertical velocities very near the wall. This is probably caused by an intrusion traveling upwards, which was detected through the vertical velocity profiles, the vector plots, and from the PIV measurements.

The instantaneous fields obtained by the PIV indicate flow unsteadiness is present in the cavity by the existence of moving vortices, which can be formed by the fluid layers moving in opposite directions. Different tests have been performed and all the results showed the same flow characteristics. These vortical structures appeared on both sides, but because the velocities on the cold wall side are lower, that region of the flow field was more strongly affected.

6.3 SUGGESTIONS FOR FUTURE WORK

A set of activities can be proposed to further improve the understanding of the physics involved in the phenomenon of turbulent natural convection in cavities:

- Design and build a new cavity with more efficient isothermal walls; in other words, with lower temperature fluctuations.
- Employ different working fluids, especially high Prandtl fluids, e.g., lubricant oils.
- Employ non-intrusive techniques to obtain the temperature field of the cavity, e.g., Liquid Crystal Thermography (LCT) or Laser Induced Fluorescence (LIF).
- Solve numerically the flow through Large Eddy Simulations without the Boussinesq approximation.

REFERENCES

- ALAMIRI, A.; KHANAFER, K.; POP, I., **Buoyancy-Induced Flow And Heat Transfer In A Partially Divided Square Enclosure.** International Journal of Heat and Mass Transfer 52 3818–3828, 2009.
- ALBRECHT, H.; BORYS, M.; DAMASCHKE, N.; TROPEA, C., **Laser Doppler And Phase Doppler Measurement Techniques.** Germany, Springer, 2003.
- AMPOFO, F., **Turbulent natural convection in an air filled partitioned square cavity.** Int. J Heat and Fluid Flow 25 103 – 114. , 2004.
- AMPOFO, F., **Turbulent natural convection of air in a non-partitioned or partitioned cavity with differentially heated vertical and conducting horizontal walls.** Exp. Thermal and Fluid Science 29 137 – 157, 2005.
- BEAN, V.; HALL, M., **New primary standards for air speed measurements at NIST.** United States, NCSL Workshop & Symposium, 1999.
- BECKWITH. T. G. (THOMAS G.), **Mechanical measurements.** Addison-wesley Publishing Company, 1993.
- BEJAN, A., **Convection heat transfer.** 3rd ed. New York: J. Wiley & Sons, 2004.
- BLONSKI, S.; KOWALEWSKI, T.; MIKIELEWICZ, D.; STASIEK, A.; STASIEK, J., **Heat Transfer Enhancement Through the use of Transverse Vortex Generators.** Italy, XXVI Congresso Nazionale UIT sulla Trasmissione del Calore, 2008.
- CUNHA, J.; SILVA, L., **L.D.V (Laser Doppler Velocimetry), P.D.A. (Phase Doppler Anemometry) - Princípios e Aplicações.** Instituto Superior Técnico, Portugal, 2000.
- DABIRI, D.; GHARIB, M., **The Effects of Forced Boundary Conditions on Flow Within a Cubic Cavity Using Digital Particle**

Image Thermometry and Velocimetry (DPITV). Experimental Thermal and Fluid Science; 13:349-363, 1996.

DOL, H.; HANJALIC, K., **Computational study of turbulent natural convection in a side-heated near-cubic enclosure at a high Rayleigh number.** International Journal of Heat and Mass Transfer 44 2323-2344, 2001.

DURRANI, T., **Noise Analysis for Laser Doppler Velocimeter Systems,** Communications, IEEE Transactions on, vol.20, no.3, pp. 296-307, 1972.

EDWARDS, R. V., **Report of the special panel on statistical particle bias problems in laser anemometry.** J. Fluids Eng. Trans ASME, 109, 89-93, 1987.

FREDERICK, R.L.; QUIROZ, F., **On the transition from conduction to convection regime in a cubical enclosure with a partially heated wall.** International Journal of Heat and Mass Transfer 44 1699-1709, 2001.

FROGATT, A., **Nuclear Reactor Hazards,** Heinrich Böll Foundation, 2005.

FUSEGI, F.; FAROUK, B.; HYUN, J. M.; KUWAHARA, K., **A Direct Numerical Simulation of periodic natural convection in differentially heated cubical enclosure.** In Proc. of Int. Symp. on Engineering Turbulence Modeling and Measurements, 261–268, 1990.

GASSOWSKI, G.; XIN, S.; DAUBE, O., **Bifurcations et solutions multiples en cavité 3D différentiellement chauffée.** C. R. Mécanique 331 705–711, 2003.

GIFFORD, A.W., **Natural Convection in a square cavity without the Boussinesq Approximation.** 49th Annual Technical Conference - ANTEC '91, pp. 2448-2454, 1991.

GRAY, D.D.; GIORGINI, A., **The validity of the Boussinesq approximation for liquids and gases,** Int. J. Heat Mass Transfer 19 545±551, 1976.

HORTMANN, M.; PERIC, M.; SCHEUERER, G., **Finite volume multigrid prediction of laminar natural convection: bench-mark solutions.** Int. J. Numer. Meth. Fluids 11, 189–207, 1990.

HORVAT, A.; KLJENAK, I.; MARN, J., **Two-dimensional large-eddy simulation of turbulent natural convection due to internal heat generation.** Int. J. Heat Mass Transfer 44 3985–3995, 2001.

HSIEH, S. S.; YANG S. S., **Transient three-dimensional natural convection in a rectangular enclosure.** Int. J Heat Mass Transfer 39 (1) 13-26, 1996.

IITC - RECOMMENDED PROCEDURES AND GUIDELINES, **Uncertainty Analysis Laser Doppler Velocimetry Calibration.** Japan, International Towing Tank Conference, 2008.

ISO, *et al.* **Guia para a Expressão da Incerteza de Medição.** Terceira Edição Brasileira "*Guide to the Expression of Uncertainty in Measurement*". Rio de Janeiro, ABNT, 2003.

JANSSEN, R. J. A.; HENKES, R. A. W. M., **Instabilities in three-dimensional differentially-heated cavities with adiabatic horizontal walls.** Phys. Fluids, Vol. 8, No. 1, January 1996.

JING, G. J.; HENRY, D., HADID, H. B. IMAISHI, N., **Low-order dynamical model for low-Prandtl number fluid flow in a laterally heated cavity.** Phys. Fluids, Vol. 15, No. 8, August 2003.

KAKAÇ, S.; AUNG, W.; VISKANTA, R., **Natural convection: fundamentals and applications.** Washington, DC.: Hemisphere; Berlin: Springer, 1985.

KER, Y. T.; LIN, T. F., **A combined numerical and experimental study of air convection in a differentially heated rotating cubic cavity.** Int. J Heat Mass Transfer 39 (15) 3193 – 3210, 1996.

KER, Y. T.; LIN, T. F., **Time-averaged and reverse transition in oscillatory air convection in a differentially heated rotating cubic cavity.** Int. J Heat Mass Transfer 49 (14) 3335 – 3349, 1997.

KIZILDAG, D.; VENTOSA, J.; RODRÍGUEZ, I.; OLIVA, A., **Non-Oberbeck-Boussinesq Natural Convection in a Tall Differentially Heated Cavity**. V European Conference on Computational Fluid Dynamics, Portugal, 2010.

KLEIN, S. B., **Engineering Equation Solver-Professional Version**, 2012.

KREPLIN, H. P; ECKELMANN, H., **Behavior of the three fluctuating velocity components in the wall region of a turbulent channel flow**. Phys. Fluids 22 1233-1239, 1979.

KUYPER, R. B.; VAN DER MEER, TH. H.; HOOGENDOORN, C. J.; HENKES, R. B. W. M., **Numerical study of laminar and turbulent natural convection in an inclined square cavity**. Int. J Heat Mass Transfer 36 (11) 2899 – 2911, 1993.

LARTIGUE, B.; LORENTE, S.; BOURRET, B., **Multicellular natural convection in a high aspect ratio cavity: experimental and numerical results**. International Journal of Heat and Mass Transfer 43 3157-3170, 2000.

LE QUÉRÉ, P., **A note on multiple and unsteady solutions in two-dimensional convection in a tall cavity**. J. Heat Transfer 112, 965–974, 1990.

LE QUÉRÉ, P., **Accurate solutions to the square thermally driven cavity at high Rayleigh number**. Computers Fluids 20, 29–41, 1991.

LEE, S.; LEE, J.; SUH, K., **Natural convection thermo fluid dynamics in a volumetrically heated rectangular pool**, Nucl. Eng. Des. 237 473–483, 2007.

LEONG, W. H.; HOLLANDS, K. G. T.; BRUNGER, B. P., **On a physically realizable benchmark problem in internal natural convection**. Int. J Heat Mass Transfer 41 (23) 3817 – 3828, 1998.

LIU, H.; ZOU, C.; SHI, B., **Thermal lattice-BGK model based on large-eddy simulation of turbulent natural convection due to internal heat generation**, Int. J. Heat Mass Transfer 49 4672–4680, 2006.

LOTH, E., **Particles, Drops and Bubbles: Fluid Dynamics and Numerical Methods**. Cambridge University Press, University of Illinois at Urbana-Champaign, 2010.

LUTJEN, P. M.; MISHRA, D.; PRASAD, D., **Three-Dimensional visualization and measurement of temperature field using Liquid Crystal Scanning Thermography**. ASME Journal of Heat Transfer 123 1006 – 1014, 2001.

MERGUI, S.; PENOT, F., **Analyse des vitesse et temperature de l'air en convection naturelle dans une cavité carrée différentiellement chauffée à $Ra = 1.69 \times 10^9$** . Int. J. Heat Mass Transfer. Vol. 40, No. 14, pp. 3427-3441, 1997

OZTOP, H.; BILGEN, E., **Natural convection in differentially heated and partially divided square cavities with internal heat generation**, International Journal of Heat and Fluid Flow 27 466–475, 2006.

PAVEL URBAN - CRYGENICS GROUP (Czech Republic). **HELIUM CRYOSTAT FOR EXPERIMENTAL STUDY OF NATURAL TURBULENT CONVECTION**. Disponível em: <<http://www.isibrno.cz/cryogenics/convection.html>>. Acesso em: 30 out. 2012.

PENOT, F.; N'DAME, A., **Successive bifurcations of natural convection in a vertical enclosure heated from the side**. Third UK National Conference and First European Conference on Thermal Sciences, vol. I, Birmingham, UK, 1992.

PENG, S. H.; DAVIDSON, L., **Large eddy simulation for turbulent buoyant flow in a confined cavity**. International Journal of Heat and Fluid Flow 22 323±331, 2001.

PENG, Y.; SHU, C.; CHEW, Y. T., **A 3D incompressible thermal lattice Boltzmann model and its application to simulate natural convection in a cubic cavity**. Journal of Computational Physics 193 260–274, 2003.

POPE, S., **Turbulent Flows**, Cambridge University Press, 2000.

QUIMIS, Inc., **Manual de Instruções**, 2010.

RAFFEL, M.; WILLERT, C.; WERELEY, S.; KOMPENHANS, J., **Particle Image Velocimetry**. Second Edition, Germany, Springer, 2007.

SALAT, J.; XIN, S.; JOUBERT, P.; SERGENT, B.; PENOT, F.; LE QUÉRÉ, P., **Experimental and numerical investigation of turbulent natural convection in large air-filled cavity**. *Int. J. Heat Fluid Flow* 25, 824–832, 2004.

SAURY, D.; ROUGER, N.; DJANNA, F.; PENOT, F.; **Natural convection in an air-filled cavity: Experimental results at large Rayleigh numbers**. *International Communications in Heat and Mass Transfer* 38, 679–687, 2011.

SCHÖPF W.; PATTERSON J. C., **Visualization of natural convection in a side-heated cavity: transition to the final steady state**. *Int. J Heat Mass Transfer* 39 (16) 3497 – 3509, 1996.

SCHWEIGER, H.; OLIVA, B.; COSTA, M.; PÉREZ-SEGARRA, C. D., **Numerical experiments on laminar natural convection in rectangular cavities with and without honeycomb structures**. *Int. J. Numer. Meth. Heat Fluid Flow* 5, 243–443, 1995.

SORIA, M.; TRIAS, F.; PÉREZ-SEGARRA, C.; OLIVA, B., **Direct numerical simulation of a three-dimensional natural-convection flow in a differentially heated cavity of aspect ratio 4**. *Numerical Heat Transfer, Part A*, 45: 649–673, 2004.

SPALART, P. R., **Direct simulation of a turbulent boundary layer up $R_\theta=1410$** , *Fluid Mech* 187 61-98, 1988.

TAROZZI, L., **Analisi Sperimentale della Convezione Naturale Mediante Tecniche Velocimetriche PIV e UPDV in Cavità Confinata**. Dottorato di Ricerca in Ingegneria Meccanica XIX Ciclo, Università Degli Studi di Modena e Reggio Emilia, 2007.

TIAN, Y.; KARAYIANNIS, T., **Low turbulence natural convection in an air filled square cavity Part I: the thermal and fluid flow fields**. *International Journal of Heat and Mass Transfer* 43 849-866, 2000.

TREECK, C. **Natural convection in a 2D cavity**. Disponível em: <<http://www.inf.bv.tum.de/~treeck/convection/convection.htm>>. Acesso em: 30 out. 2012.

TRIAS, F. X.; SORIA, M.; OLIVA, A.; PÉREZ-SEGARRA, C. D., **Direct Numerical Simulation of two- and three-dimensional turbulent natural convection flows in a differentially heated cavity of aspect ratio 4**. Journal of Fluid Mechanics 586 259 – 293, 2007.

TRIAS, F.X.; VERSTAPPEN, R. W. C. P.; GOROBETS, B., SORIA, M., OLIVA, B., **Direct numerical simulation of a differentially heated cavity of aspect ratio 4 with Rayleigh numbers up to 1011 – Part I: Numerical methods and time-averaged flow**. International Journal of Heat and Mass Transfer 53 665–673, 2010.

TRIC, E.; LABROSSE, G.; BETROUNI, M., **A first incursion into the 3D structure of natural convection of air in a differentially heated cubic cavity, from accurate numerical solutions**. International Journal of Heat and Mass Transfer 43 4043-4056, 2000.

TSI, Inc., **LDV Operational Manual**, 2006.

TSI, Inc., **Seed Particles for LDV and PIV**, 2006.

TSI, Inc., **Standard Traverse Systems for LDV, PDPA and PIV**, 2006.

TSI, Inc., **TR/TM Series Fiberoptic Probes**, 2007.

TSI, Inc., **Optical Systems - LDV/PDPA Workshop & Training**, 2008.

TSI, Inc., **Accuracy, Resolution, and Repeatability of PDPA and LDV, 2008**.

VAHL DAVIS, G.; JONES I. P., **Natural convection in a square cavity: a comparison exercise**. Int. J. Numer. Meth. Fluids 3, 227–248, 1983.

WILCOX, D., **Turbulence Modeling for CFD**, 3rd Edition, DCW Industries, Inc., La Canada, California, 2010.

WINTER, A. R.; GRAHAM, L. J. W.; BREMHORST, K., **Effects of time scales on velocity bias in the LDA measurements using sample and hold processing.** Experiments in Fluids 11, 147-152, 1991.

APPENDIX A - UNCERTAINTY EVALUATION

Every experimental measurement carries a certain amount of uncertainty. In order to evaluate the measurement uncertainty, it is recommended to follow a methodology described by the "Guide to Expression of Uncertainty in Measurement" ISO (2003), which comprises the following steps:

1. Identification of the measurand
2. Identification of uncertainty sources
3. Quantification of uncertainty sources
4. Determination of combined uncertainty
5. Evaluation of expanded uncertainty

The first step focuses on the correct specification of the measurand, symbolized by the generic Y . It is necessary to know clearly and without ambiguity what is required to be measured, and always if possible, to establish an algebraic expression relating the value of the measurand to the parameters in which the measurand is a function. These parameters can be other measurands, quantities not directly measured, constants, or even coefficients.

In the second step, all the possible uncertainty sources should be listed (X_i). In this stage, it is not necessary to worry about the individual quantification of each source. The objective is to have very clearly in mind all the important parameters to be regarded in the measurement proceedings.

To start a list of uncertainty sources, it is convenient to initially write a basic expression in order to obtain the value of the measurand as a function of intermediate values that define the output value of the measurand. Each parameter in this expression should have an uncertainty value associated with it, and must be a potential source of uncertainty. Furthermore, it might have other parameters that do not appear explicitly in the expression but do affect the measuring process and contribute to the measurand uncertainty.

In the implicit form, the expression of the measurand identified in the first step can be expressed in a generic form as:

$$Y = f(X_1, X_2, \dots, X_N) \quad (\text{A.1})$$

In the third step, the quantification of the uncertainty sources must be done. The uncertainty of the measurand is evaluated by

combining the uncertainty from each source (each variable from the measuring process).

Each component of uncertainty (x_i) can be classified into two types: Type A and Type B.

A.1 TYPE A EVALUATION OF UNCERTAINTY

A Type A evaluation of uncertainty may be based on any valid statistical method for treating data. It consists of evaluating the dispersion of the values over an average (variance) due to its random behavior.

As an example of a Type A evaluation, consider an input quantity x_i whose value is estimated from n independent observations $x_{i,k}$ of x_i obtained under the same conditions of measurement. In this case, the input estimate \bar{x}_i is usually the sample mean:

$$\bar{x}_i = \frac{1}{n} \sum_{k=1}^n x_{i,k} \quad (\text{A.2})$$

and its standard deviation is obtained by the following expression:

$$s(x_i) = \sqrt{\frac{1}{(n-1)} \sum_{k=1}^n (x_{i,k} - \bar{x}_i)^2} \quad (\text{A.3})$$

and finally, its standard uncertainty:

$$u(\bar{x}_i) = \frac{s(x_i)}{\sqrt{n}} \quad (\text{A.4})$$

A.2 TYPE B EVALUATION OF UNCERTAINTY

This is a method of evaluation of uncertainty by means other than the statistical analysis of a series of observations. A Type B evaluation of standard uncertainty is usually based on scientific judgment using all of the relevant information available, which may include: previous measurement data, the behavior and property of relevant materials and instruments, manufacturer's specifications, data provided in calibration and other reports, and uncertainties assigned to reference data taken from handbooks, etc.

In order to evaluate the Type B uncertainty, it is necessary to know the probability distribution associated with the value of the uncertainty source in question. The most common uncertainty sources are:

A.2.1 Rectangular Probability Distribution

In rectangular distribution, it is necessary to estimate lower and upper limits a_- and a_+ for the value of the input quantity in question, such that the probability that the value lies in the interval $[a_-, a_+]$ is for all practical purposes, 100%. The best estimate of the value of the quantity is then the half-width of the interval:

$$x_i = (a_+ + a_-)/2 \quad (\text{A.5})$$

Therefore, in this case, the standard uncertainty is calculated by the expression:

$$u(x_i) = \frac{a_i}{\sqrt{3}} \quad (\text{A.6})$$

A.2.2 Normal Probability Distribution

Many events in nature occur in this way; the "bell" shape of the normal distribution makes it a convenient choice for modeling a large variety of random variables encountered in practice. The standard uncertainty (type B) is obtained by:

$$u(x_i) = \frac{a_i}{k_p} \quad (\text{A.7})$$

where k_p is the coverage factor of a certain level of a specified confidence p . For a t-Student distribution, Table A.0.1 gives this factor; this table is for large numbers of samples ($n > 100$).

Table A.0.1- Level of confidence x coverage factor.

Level of confidence p (%)	Coverage factor k_p
50	0.6756
68.27	1

90	0.6756
95	1.960
95.45	2
99	2.576
99.73	3

After the identification of each source of uncertainty, and the determination of each value of its standard uncertainties $u(x_i)$, the next step is to combine them to obtain the combined standard uncertainty.

Employing the Theory of Error Propagation described by Herschy, the combined standard uncertainty is given by the following equation:

$$u_c = \sqrt{\sum_{i=1}^N c_i^2 u^2(x_i) + 2 \sum_{i=1}^{N-1} \sum_{j=i+1}^N c_i c_j u(x_i) u(x_j) r(x_i, x_j)} \quad (\text{A.8})$$

Where c_i are the sensitivity coefficients $\left(\frac{\partial f}{\partial x_i}\right)$ from each source of uncertainty, $u(x_i)$ are the standard uncertainties and $r(x_i, x_j)$ the correlation coefficients.

If the uncertainty sources are uncorrelated, $r(x_i, x_j) = 0$, and Equation A.8 becomes:

$$u_c = \sqrt{\sum_{i=1}^N c_i^2 u^2(x_i)} \quad (\text{A.9})$$

The combined standard uncertainty $u_c(Y)$ expresses the result within a range of one standard deviation (68.27% for a normal curve, see Table A.0.1). Although the value $u_c(Y)$ can be used to express the uncertainty of a measurement result, there are cases in which it is necessary to express the uncertainty within an expected interval that covers a large fraction of the distribution of values assigned to the measurand. This requirement defines the expanded uncertainty $U(Y)$:

$$U(Y) = k_p \cdot u_c(Y) \quad (\text{A.10})$$

where $u_c(Y)$ is the combined standard uncertainty of the measurement Y . The result of a measurement can be expressed by its average (y) and the expanded uncertainty $U(Y)$:

$$Y = y \pm U \quad (\text{A.11})$$

The coverage factor (k_p) depends of the effective degrees of freedom of the combined uncertainty and the required level of confidence, as described by ISO-GEUM (2003). In order to obtain the effective degrees of freedom, the Welch-Satterthwaite equation can be used as follows:

$$\nu_{eff} = \frac{u_c^4(Y)}{\sum_{i=1}^N \frac{u^4(x_i)}{\nu_i}} \quad (\text{A.12})$$

After defining the values of degrees of freedom, the t-Student coefficient used with the level of confidence $k_p = t(\nu_{eff})$. ISO-GEUM shows the values to be used according to the effective degrees of freedom.

A.2.3 Polynomial Uncertainty

It is a common practice to adopt calibration curve fitting obtained from the Least Squares Method. This curve is obtained from known values of measurand (V_k) and the output values of the measuring instrument. Thus, it is necessary to evaluate the uncertainty from the value obtained by this calibration curve fitting.

The uncertainty from the calibration curve fitting is obtained by the following equation:

$$u(x_i) = \sqrt{\frac{\sum_{k=1}^N (V_k - V_{LS,k})^2}{N - (1 + PD)}} \quad (\text{A.12})$$

Here, this uncertainty is going to be named as the polynomial uncertainty.

Where:

V_k = k -th value of the measured temperature, usually obtained by a standard instrument;

$V_{LS,k}$ = is the value obtained by the polynomial curve fitting from calibration, which corresponds to the measured value of V_k ;

PD = polynomial degree;

N = number of points employed in the curve fitting.

APPENDIX B - ANALYSIS OF VELOCITY UNCERTAINTY

According to Equations (3.1) and (3.2), the measured velocity has three uncertainty sources, and they are listed as follows:

1. Wavelength, λ ;
2. Half-angle between the crossing beams, $\theta/2$;
3. Doppler frequency, f_D .

Using the cause and effect diagram to express the uncertainty from the velocity measured by the LDV, we obtain Figure B.0.1:

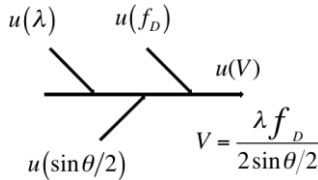


Figure B.0.1- Cause and effect diagram for a velocity component.

In Figure B.0.1, $u(\lambda)$ represents the wavelength uncertainty of λ , $u(\sin(\theta/2))$ is the sine uncertainty of the semi-angle between the two laser beams, and $u(f_D)$ is the uncertainty from the value of the Doppler frequency captured from the photo detector.

If the uncertainties sources are uncorrelated, then Equation A.8 becomes Equation B.1:

$$u_c = \sqrt{\sum_{i=1}^N c_i^2 u^2(x_i)} \quad (\text{B.1})$$

Rewriting Equation B.1 through the components shown in Figure B.0.1, we obtain Equation B.2, as follows:

$$u_c(V) = \sqrt{c_\lambda^2 u^2(x_\lambda) + c_\theta^2 u^2(x_\theta) + c_{f_D}^2 u^2(x_{f_D})} \quad (\text{B.2})$$

Where the sensitivity coefficients are given by the following expressions:

$$c_\lambda = \frac{f_D}{2 \sin(\theta/2)} \quad (\text{B.3})$$

$$c_{\theta} = -\frac{\cos(\theta/2)}{4\sin^2(\theta/2)} \lambda f_D \quad (\text{B.4})$$

$$c_{f_D} = \frac{\lambda}{2\sin(\theta/2)} \quad (\text{B.5})$$

For commercial LDV systems, the uncertainty in the wavelength is negligible, of the order of 0.01%. Bean and Hall (1999) have described a method for the measurement of the intersection half-angle of the laser beams $\theta/2$. The position of a transmitted laser beam was detected by a photo-diode mounted behind a 0.25 mm vertical slit. The photo-diode was mounted on a translation stage that traversed normal to the axis of the fiber-optic probe. The fiber-optic probe was mounted on a translation stage that traversed in a direction along the axis of the probe. For a fixed position, the distance between the axis of the laser and the location of the laser beam was measured as the distance CE. The laser was then translated towards the laser-diode translation stage by the distance AB, and the distance to the new position of the laser beam was measured as the distance CD. The half-angle was then obtained through Equation B.6:

$$\theta/2 = \tan^{-1} \left(\frac{CE-CD}{AB} \right) \quad (\text{B.6})$$

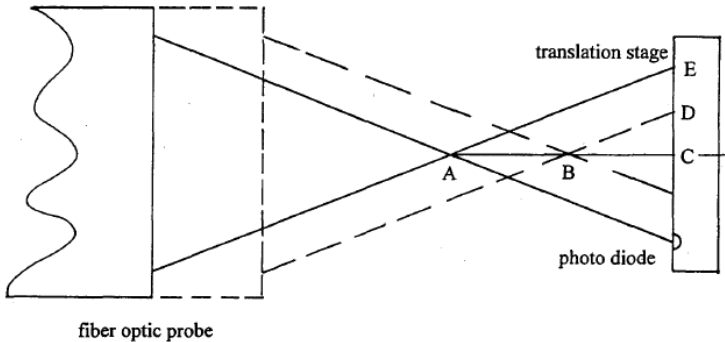


Figure B.0.2- Schematic diagram showing the experimental arrangement for direct measurement of the intersection angle of the laser beams (Bean and Hall, 1999).

The Doppler frequency has basically two sources of noise: electronic circuit and optical systems. In general, these uncertainties are less than 1% and are independent of the velocity values, as mentioned by ITTC - Recommended Procedures and Guidelines (2008).

ATTACHMENT A- Part 1: Calibration Report of the bulb thermometer

	Laboratório de TEMPERATURA E UMIDADE Pertencente à Rede Brasileira de Calibração	
	<h2>Certificado de Calibração</h2>	
Data da Calibração: 14/05/12	n. 2299/12	
Data da Emissão: 16/05/12		
Página: 1 de 2		
1. CONTRATANTE:	ALVARO TOUBES PRATA / CNPQ573581/2008-8 Campus Universitário, - Florianópolis - SC	
2. SOLICITANTE:	O mesmo	
3. TERMÔMETRO DE LÍQUIDO EM VIDRO CALIBRADO (SMC):		
n. Série (fabricante): 31739	Fabricante: Incoterm	
n. Identif. (solicitante): TC 19	Tipo de Imersão: Parcial	
Intervalo de Medição: [-10,7 a 52,7]°C	Tipo de Escala: Interna	
Valor de Uma Divisão de Escala: 0,1°C	Líquido Termométrico: Mercúrio	
Resolução Adotada: 0,05°C		
4. PADRÃO UTILIZADO (SMP):	5. PROCEDIMENTO DE CALIBRAÇÃO	
4.1 TERMÔMETRO DE RESISTÊNCIA TIPO PT100	PC-268	
n. Registro (CERTI): 002409	O termômetro a calibrar (SMC) foi montado junto ao termômetro padrão (SMP), em um meio termicamente controlado. Após o sistema atingir a temperatura desejada foram aguardados 10 minutos para garantir a estabilidade térmica do sistema e então iniciada a calibração. Foram realizados, pelo menos, 6 ciclos de medição com intervalos de 1 minuto entre cada ciclo.	
U: [0,07]°C		
Rastreabilidade Metrológica: Certificado de Calibração CONSISTEC CR-5663/11, de 13/06/11, válido até 30/06/12.		
4.2 INDIC. DIGITAL HART SCIENTIFIC - BLACK STACK		
n. Registro (CERTI): 000662		
U: [0,006]ohms		
Rastreabilidade Metrológica: Certificado de Calibração YOKOGAWA 02873/11, de 10/06/11, válido até 14/06/12.		
<small>Este certificado atende aos requisitos de acreditação pela Cgcre, que avalia a competência do laboratório e compreve sua rastreabilidade a padrões nacionais de medida. A Cgcre é signatária do Acordo de Reconhecimento Mútuo da ILAC - International Laboratory Accreditation Cooperation, e do Acordo Bilateral de Reconhecimento Mútuo com a EA - European Cooperation for Accreditation. Os resultados deste certificado referem-se exclusivamente ao instrumento submetido à calibração, nas condições específicas, não sendo extensivos a quaisquer lotes. Esta calibração não isenta o instrumento do controle metrológico estabelecido na regulamentação metrológica. A CERTI autoriza a reprodução deste certificado, desde que qualquer cópia sempre apresente seu conteúdo integral. O ajuste de instrumentos, quando realizado, não faz parte do escopo de acreditação do laboratório.</small>		
Fundação Centro de Referência em Tecnologias Inovadoras - CERTI		
Campus da Universidade Federal de Santa Catarina - UFSC	Setor C CEP: 88040-970 Florianópolis - SC Caixa Postal 5053	Tel.: +48 3239 2121 Fax: +48 3239 2119 metrologia@certi.org.br www.certi.org.br
		Fundação CERTI CNPJ 78.626.363/0001-24 Insc. Est. 251.378.241 Insc. Mun. 50.111-5

ATTACHMENT A- Part 2: Calibration Report of the bulb thermometer



Laboratório de
TEMPERATURA E UMIDADE
Pertencente à Rede Brasileira de Calibração



Certificado de Calibração

Data da Calibração: 14/05/12

n. 2299/12

Data da Emissão: 16/05/12

Página: 2 de 2

6. OBSERVAÇÕES:

6.1 A incerteza expandida de medição (U) relatada é declarada como a incerteza padrão de medição multiplicada pelo fator de abrangência k , o qual para uma distribuição t com graus de liberdade efetivos (ν_{eff}) corresponde a uma probabilidade de abrangência de aproximadamente 95%. A incerteza de medição foi determinada de acordo com a publicação EA-4/02 (1999). Os valores de k e ν_{eff} são apresentados na tabela de resultados.

6.2 Condições ambientais durante a calibração: Temperatura Ambiente: $[23 \pm 5]^\circ\text{C}$; Umidade Relativa do Ar: $[60 \pm 20]\%$ ur

6.3 Correção = - [Média das Indicações no Termômetro a Calibrar (SMC) - Média das Indicações no Termômetro a Padrão (SMP)]. O valor da correção deverá sempre ser somado algebricamente à indicação do SMC.

6.4 Os valores de temperatura apresentados estão em conformidade com a Escala Internacional de Temperatura de 1990 - ITS 90.

7. RESULTADOS

TABELA DE RESULTADOS					
Média das Indic. no SMP [$^\circ\text{C}$]	Média das Indic. no SMC [$^\circ\text{C}$]	Correção [$^\circ\text{C}$]	Incerteza U [$^\circ\text{C}$]	Fator de Abrangência k	Graus de Liberdade ν_{eff}
-10,04	-10,10	0,06	0,12	2,00	Infinito
0,00	0,00	0,00	0,09	2,00	Infinito
20,05	20,10	-0,05	0,09	2,00	Infinito
50,00	50,10	-0,10	0,09	2,00	Infinito



Reginaldo Origuela Filho
Signatário Autorizado



Reginaldo Origuela Filho
Responsável pela Calibração

Este certificado atende aos requisitos de acreditação pela Cgcre, que avaliou a competência do laboratório e compromissos sua rastreabilidade a padrões nacionais de medida. A Cgcre é signatária do Acordo de Reconhecimento Mútuo da ILAC - International Laboratory Accreditation Cooperation, e do Acordo Bilateral de Reconhecimento Mútuo com a EA - European Cooperation for Accreditation. Os resultados deste certificado referem-se exclusivamente ao instrumento submetido à calibração, nas condições especificadas, não sendo extensível a quaisquer fôtos. Esta calibração não isenta o instrumento do controle metrológico estabelecido na regulamentação metrológica. A CERTI autoriza a reprodução deste certificado, desde que qualquer cópia sempre apresente seu conteúdo integral. O ajuste de instrumentos, quando realizado, não faz parte do escopo de acreditação do laboratório.

Fundação Centro de Referência em Tecnologias Inovadoras - CERTI

Campus da Universidade Federal de Santa Catarina - UFSC	Setor C CEP: 88040-970 Florianópolis - SC Caixa Postal 5053	Tel.: +48 3239 2121 Fax: +48 3239 2119 metrologia@certi.org.br www.certi.org.br
		Fundação CERTI CNPJ 78.626.363/0001-24 Insc. Est. 251.378.241 Insc. Mun. 50.111-5

ATTACHMENT B - REPEATABILITY OF EXPERIMENT